A Platform for Nanomaterial-Enhanced Gas Sensing using Magnetomotive MEMS

by

Henry A. Brausen

A thesis submitted in partial fulfillment of the requirements for the degree of

Master of Science

in

Microsystems and Nanodevices

Department of Electrical and Computer Engineering

University of Alberta

Abstract

We present a platform for research into nanomaterial-enhanced gas sensing using magnetomotive MEMS resonators. A microfabrication process flow is developed and carried out to create metallized silicon MEMS resonators. In tandem, a test system based around a balanced electronic bridge is constructed to perform full electrical characterization of our devices, both in atmosphere, and at vacuum. An innovative fine-tuning circuit allows this apparatus to be built at low-cost. Initial results, compared with predictions from modelling, reveal that our system works as intended, but further optimization of our devices is required to achieve the best possible performance.

Acknowledgments

First of all, I owe a tremendous amount of thanks to my supervisor, Dr. Jeremy Sit. Thank you for giving me so much freedom to experiment and play with new ideas in the lab. Thank you for providing such a rich environment for learning new things. And thank you for being so supportive, encouraging, and positive. Working with you has been a pleasure.

A huge thank you to the NanoFab staff that made this project possible. Thank you to Keith Franklin for all your help, especially while constructing the vacuum system. You were always there when I needed to borrow a tool, some bolts, or a second opinion on what might or might not work. Thank you to Dr. Aaron Hyrciw for training me on electron beam lithography, and for providing valuable insight into the fabrication challenges we faced. Thank you to Stephanie Bozic for training me on so many tools, your patience with me, and for sharing a wealth of practical advice. Thank you to Scott Munro for your training and advice as well. And thank you to all the other staff members that helped me in some way with my work. I could not have asked for a better environment or friendlier people.

Thanks also to the staff of the ECE machine shop for guidance towards designing the mechanical test fixture and magnet retaining bracket, and for fabricating these parts. Thank you especially to Herbert Dexel for your valuable one-on-one advice.

Thank you Dr. Michael Brett and the Glancing Angle Deposition group for introducing me to microfabrication and thin-film engineering early on. The ins and outs of handling small chips with tweezers, performing thin-film depositions, preparing SEM samples, along with quite a few more day-to-day

skills I probably take for granted, I learned from you.

Contents

List of Tables

List of Figures

Chapter 1

Introduction

This thesis is concerned with the design and fabrication of nanomaterial-functionalizable gas sensors based on resonating MEMS structures, as well as the instrumentation for their characterization.

Gravimetric sensors based on MEMS and NEMS resonators have garnered interest as a possible next-step in the evolution of gas sensing technology. [6] These minuscule sensors – built using well-understood techniques and processes from the microfabrication industry – are particularly suited for mass production, as well as subsequent integration with semiconductor technology. Such devices hold promise for application as sensitive detectors in mass spectrometers [7], gas chromatography [8], as well as in safety applications, sensing dangerous gases that present a hazard even in vanishingly small concentrations [9].

The operational principle of resonant gravimetric sensors is simple: when material is adsorbed on the surface of a mechanical resonator, the subsequent mass-loading creates a change in the frequency of resonance (Figure. 1.1). This frequency change may then be read out electronically, resulting in a measurement of the mass of the adsorbed material. Furthermore, by chemically modifying the surface of the resonator, one can tailor the device to preferentially adsorb certain classes of molecules, yielding a *specific* sensor. Arrays of such specific sensors may be used for chemical identification.

The major advantage of sensing using resonant MEMS and NEMS struc-
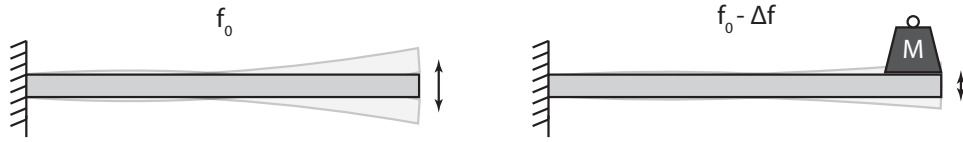
Figure 1.1: Operational principle of a resonant MEMS gravimetric sensor. Mass added to a resonator causes a shift in resonant frequency, which can be detected electronically.

tures is mass sensitivity. This sensitivity, simply speaking, derives from the fact that the resonant structures themselves are physically small – any adsorbed material produces a *relatively* large change in the resonating mass, thus producing a significant change in the behaviour of the device. This relative change in resonant behavior is then measured and converted into an electrical readout, i.e. we have a sensor.

Intuitively, scaling down the size of a resonator reduces its mass, hence further increasing the effect of some small amount of adsorbed material on the resonant properties of the device. Generally speaking, the smallest devices exhibit the highest mass sensitivity. (For an extreme example, a sensor based on a single carbon nanotube achieved a mass resolution of 1.7×10^{-24} g, or on the order of a single proton.) [10] This mass sensitivity, however, comes at the expense of surface area – a smaller device presents a smaller surface to which gas molecules may adsorb, reducing the coupling between the resonator and the surrounding gas.

One potential avenue to addressing the problem of low surface area in the domain of NEMS gravimetric sensors is to functionalize the resonator surface with a high-surface area nanomaterial. [11, 12] This nanomaterial should be low-density, so as to prevent significant loading of the resonator and to preserve its inherently high mass sensitivity. Furthermore, the nanomaterial should not introduce significant damping of mechanical resonance, as damping negatively impacts the final sensitivity of the device as well. Finally, the material should be amenable to chemical functionalization to enable analyte-specific sensors to be developed.

Working from these requirements, we have found SiO_2 Glancing-Angle

Deposition (GLAD) films to be an excellent candidate material for this gas sensing application. These films exhibit extremely high surface area [13], porosity [14], low mass density, and may be chemically functionalized using established techniques. [15, 16] Furthermore, these films are believed to be discontinuous where they interface with the substrate, which leads us to believe that damping effects due to mechanical flexure of interfacing materials should be minimal. A MEMS gravimetric sensor functionalized using GLAD films has the potential to bring together the best of both worlds – high surface area, and high mass sensitivity.

Earlier work by Westwood et al. explored the preliminary application of this idea by performing optical measurements on GLAD-functionalized Si resonators, establishing the feasibility of enhancing the surface-area of NEMS resonators by means of a porous nanostructured film. [11] For further research into this area, we require a platform to allow measurement of functionalized MEMS resonators in a controlled environment, and at a low cost.

This work brings together a number of ideas, techniques and technologies reaching from materials science and engineering, to electrical engineering and beyond. Before we delve deeply into the material, it will help to review a few of the methods used to measure the mechanical response of small resonant devices. This discussion of actuation and detection techniques is followed by a brief discussion on GLAD film growth, followed by an overview of the devices considered in this thesis.

1.1 Actuation and Detection

Necessary to achieving the goal of bringing together GLAD and MEMS / NEMS technologies is a scheme for the actuation and detection of motion of these devices. In particular, detection of NEMS resonators presents a unique challenge as the devices are so vanishingly small – as device dimensions shrink, so too do the physical effects we use to measure their behaviour. A number of schemes have been used to actuate and detect small resonators. Herein we outline a selection of techniques and their salient advantages and

disadvantages.

1.1.1 Optical Detection

Interferometric optical readout is a potential approach to measuring the small deflections characteristic of NEMS sensors. The basic scheme is as follows: a laser is used to illuminate the resonator. The cavity formed between the suspended NEMS structure and the substrate forms an optical resonator whose precise frequency of resonance is a function of the deflection of the NEMS. As the NEMS resonates, it modulates the properties of the cavity, hence modulating the interference of reflected laser light. The reflected light is detected using a photodiode and converted into an electronic signal for detection. This sort of detection scheme has been used many times in the literature. [17]. A theoretical analysis of this technique is found in [18], while some applied examples of optical detection are found in [19–22]. Notably, optical detection is compatible with Si micromachined resonators that have been coated in a GLAD nanostructured film. [11,12].

The main challenge associated with this technique is that the apparatus is complex and difficult to work with. One must be careful to align all optical components properly, and the laser spot must be carefully directed to illuminate the vanishingly small resonator. Apart from the difficulty associated with working in the optical domain, this approach comes at the expense of potential integration, as optical components are bulky and cannot (at this time) be integrated with the resonator on the chip. Furthermore, low-power illumination must be used to avoid heating the resonator and affecting the results of measurement [17], which limits achievable signal to noise (SNR). Finally, depending on the architecture of the resonator, the presence of some materials may absorb or scatter light, preventing optical coupling to the cavity between the resonator and substrate, and thereby yielding a weaker signal. All of these issues are compounded by the fact that optical instrumentation is expensive. For these reasons, we chose to avoid using optical techniques in measuring resonator motion.

1.1.2 Piezoelectric Actuation

Perhaps the simplest method for actuation of small resonators is to mechanically "shake" them into motion. This may be accomplished by bonding the chip containing the resonators to a piezoelectric disk. [11, 12] Though simple, this method has a number of distinct disadvantages. First of all, the amount of coupling between the piezoelectric disk and the resonators is not clear, and is difficult to relate to the strength of the driving signal. Second, the actuation itself is relatively narrowband with this technique, as piezoelectric disks tend to mechanically resonate only over a relatively narrow bandwidth. This limited bandwidth of actuation would seriously limit the variety of devices we could measure. For these reasons, we chose to forgo the use of a piezoelectric disk for the purposes of actuation.

There remains the possibility of integrating a piezoelectric element in the resonant structure for the purposes of actuation. We chose to disregard this approach primarily due to the added fabrication complexity such a scheme would create. In a production environment with strict quality and process control, piezoelectric actuation is certainly viable; however, in a research environment, it is necessary to keep device complexity to a minimum.

1.1.3 Piezoresistive Detection

The piezoresistive effect represents another potential avenue for detection of resonator motion. Under this scheme, a piezoresistor is integrated into the resonating structure in a location with a large time-varying strain. This mechanical strain then couples into the electrical resistance of the piezoresistor. The time-varying electrical resistance of the piezoresistor may then be measured to yield a measurement of resonator motion. Some examples of piezoresistive detection applied to the measurement of resonator motion are given in [5, 9, 23, 24].

The major advantage of this scheme is that readout is purely electrical, making it especially well-suited to integration with electronic readout circuitry. Furthermore, piezoresistors are relatively easy to fabricate – doped silicon, one of the key building blocks of modern microfabrication processes,

readily exhibits the piezoresistive effect.

The downsides of this technique are two-fold. First of all, the piezoresistive effect may only be used to detect resonator motion – it does not lend itself to driving the resonator into oscillation in the first place. Therefore, this scheme requires the application of a separate technique for actuation, increasing the complexity of the final system.

Perhaps more limiting is the fact that small piezoresistors (on the size-scale of the resonating element) have a large associated resistance on the order of 10 kΩ or more. [5] This resistance, coupled with the presence of unavoidable parasitic capacitances in the measurement apparatus, creates a low-pass filter that severely limits performance beyond a couple of megahertz. These capacitances may be minimized through the use of on-chip readout circuitry, but this is hardly feasible for a platform for research into resonant sensors due to the complexity involved.

The piezoresistive technique may be salvaged, however, though the use of an RF downmixing technique that exploits the properties of the piezoresistor to translate the high-frequency readout signal to a lower intermediate frequency for the sake of measurement. [5] On-chip downmixing bypasses the restrictions imposed by the low-pass filter formed by the high-source-impedance of the piezoresistive element and the measurement apparatus without requiring complex measurement circuitry to be built up on-chip. [5] The price to pay is a marked increase in the complexity of the measurement apparatus.

1.1.4   Magnetomotive Actuation and Detection

Magnetomotive actuation and detection schemes exploit the physical interaction between electric currents and static magnetic fields in order to both set into motion and detect the vibration of small resonators. The basic scheme is as follows: a time-varying (AC) electric current is passed through a resonator which is immersed in a uniform magnetic field. The time-varying current in the presence of the magnetic field generates a Lorentz force, driving the resonator into mechanical motion. As the resonator moves through

the magnetic field, the motion produces a back-emf which exhibits the same frequency dependence as the mechanical resonance. This back-emf gives rise to a frequency dependent change in the electrical (vector) impedance of the resonator. Measuring the frequency dependence of impedance allows the resonator to be characterized. Some examples of magnetomotive actuation and detection in the literature are found in [4, 22, 25–29].

This method has a number of distinct advantages. First of all, fabrication is extremely simple: one need only render the resonator electrically conductive, which may be carried out by means of doping or metallization. Furthermore, there is a clear physical relationship between the magnitude of the driving signal and the amount of force imparted on the resonator, making modeling more precise and allowing the researcher to work directly with easy to interpret physical quantities. A broadband technique, magnetomotive actuation and detection has been demonstrated far into the UHF spectrum, allowing a single apparatus to measure a wide variety of sensors. Finally, because magnetomotive schemes transduce resonator motion directly into the electrical domain, they are particularly suited to eventual integration with readout circuitry.

This technique, however, is not without downsides. Perhaps most problematic is the fact that the change in impedance due to resonance is extremely small, threatening to make electronic readout extraordinarily difficult. Furthermore, as devices are shrunk down in size, the coupling between the magnetic field and the (now spatially-small) electric current decreases, reducing mechanical drive and the relative change in electrical impedance. These issues may be circumvented somewhat by increasing the magnetic field strength, which increases the back-EMF and hence the change in impedance; however, this is only at considerable cost to the researcher. Magnetic fields with flux density above about 1 Tesla are near-impossible to generate over a physically-useful volume without the use of superconducting coils. Such equipment represents a significant investment and is therefore out of reach for many researchers.

A partial solution comes in the form of balanced-bridge measurement techniques. [17, 26, 27] These techniques, as will be discussed in detail later

in this thesis, transform a measurement of *absolute* impedance to one of *relative* change in impedance. Combined with delicate electronic fine-tuning, balanced systems can be made extraordinarily sensitive to minuscule relative changes in impedance – precisely the sort of sensitivity required for electronic readout of magnetomotive resonators. Careful application of this technique can overcome the need for extremely strong magnetic fields in the measurement apparatus, allowing the use of low-cost permanent magnet assemblies, making this technique attractive for low-cost research into resonant sensing. For this reason, we have chosen to use the magnetomotive technique for simultaneous actuation and detection of our resonators.

1.2   Glancing Angle Deposition

Glancing angle deposition (GLAD) is an extension of traditional physical-vapour-deposition (PVD) techniques that enables growth of columnar nanostructured thin films with significant control over film morphology.

GLAD works by exploiting the ballistic nature of film growth in (near) vacuum. In a typical system, a flux of material (generated using electron-beam evaporation, traditional evaporation, or sputtering) is incident at a highly oblique angle α to a substrate, as illustrated in Figure. 1.2. At high values of α, ballistic shadowing occurs; *i.e.* previously deposited material blocks certain areas of the substrate from receiving material flux. Over time, this shadowing gives rise to the growth of an anisotropic, columnar thin film. (Figure. 1.2). By varying α, column spacing and tilt can be carefully controlled. Where isotropy is desired, the substrate may be continuously rotated about its normal axis (angle ϕ) over the course of deposition, yielding a film composed of very uniformly spaced "vertical post" structures. By actively varying α and ϕ over the course of the deposition, a stunning variety of thin film nanostructures can be grown, including helices, zig-zags, square spirals and more. An excellent introduction to the GLAD technique can be found in [30], while details about film growth dynamics are presented in [31, 32].

GLAD films have a number of properties that make them especially
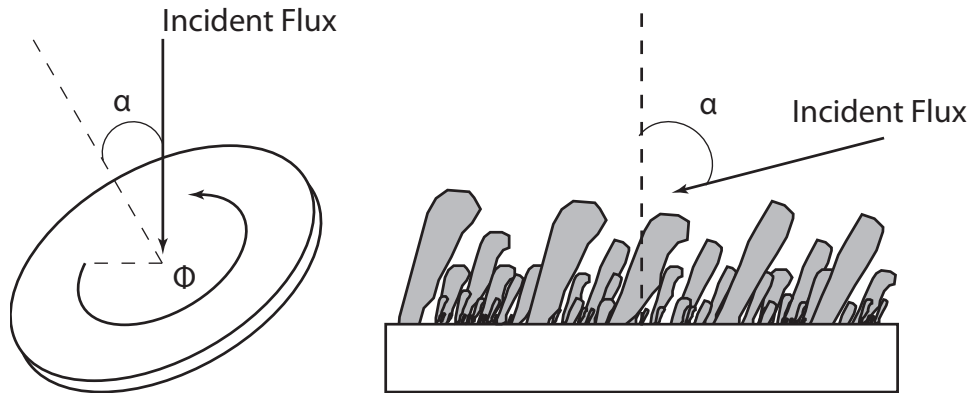
Figure 1.2: Left: Illustration of material flux incident at an oblique angle α to a substrate. The ϕ direction is labeled. Right: Illustration of GLAD film growth due to material incident at the oblique angle α.

interesting for application to NEMS resonant sensors. First of all, these films are highly porous, exhibiting a massive enhancement of surface area over that of the substrate. [13, 14] For application in gas sensing, a higher effective surface area should yield a more sensitive device. Second, the films are discontinuous at the interface with the substrate. This discontinuity is expected to reduce both residual film stress as well as the any mechanical damping effects that arise due to interfacing of dissimilar materials. Finally, GLAD SiO_2 films in particular are amenable to chemical functionalization [15, 16], providing a path for manufacture of specific sensors in the future. Taken together, these features make GLAD an attractive candidate material for enhancement of gravimetric sensors.

Essential to achieving workable GLAD performance is that the material flux be collimated. A lack of collimation in the flux undermines the effect of shadowing, inhibiting GLAD growth. [30] For this reason, typical GLAD systems place the source physically far away from the substrate. The requirement of collimation presents an obstacle to GLAD sputtering, as the presence of the working gas along with the physical size of the large yield a less collimated flux of material when compared with evaporation systems. [30, 33] This issue of collimation can be partially overcome by the use

of low-pressure long-throw sputtering [33], or by using a physical screen to block the uncollimated part of the vapour flux. [30, 34]

A schematic of a typical (electron-beam evaporation) GLAD system is illustrated in Figure 1.3. Here, two motors provide complete dynamic control of the substrate orientation during deposition. A quartz crystal monitor (QCM) in the deposition system measures film growth over time. The QCM readout is related to the GLAD film thickness by an α-dependent factor, and allows film growth parameters to be varied as a function of film thickness. This active feedback control allows repeatable growth of films with thickness-dependent properties.

1.3 Overview of Our Devices

In this thesis, we consider two types of magnetomotive MEMS resonators. The first of these is the doubly-clamped beam (DCB), which is somewhat analogous to a guitar string. A thin beam is mechanically supported on both ends, as illustrated in Figure. 1.4. The device is immersed in a magnetic field that is oriented perpendicular to the beam. A time-varying current driven through the beam creates a Lorentz force which drives the structure into mechanical resonance. For a detailed analysis, see chapter 2.

The second device we consider in this work is the U-cantilever resonator, illustrated in Figure. 1.4. Two cantilevers, clamped on one end, are joined by means of a cross-bar. The device is immersed in a magnetic field that is oriented perpendicular to the cross-bar, and a time-varying current is driven through the "U". The resulting Lorentz force drives the structure into mechanical resonance. See chapter 2 for a detailed analysis.

These devices are amenable to functionalization with GLAD films, as they have planar surfaces. Furthermore, careful engineering of the surrounding topography should allow edge effects – in which film growth dynamics differ at the edges of the resonator as compared to the middle – to be mitigated. [12]
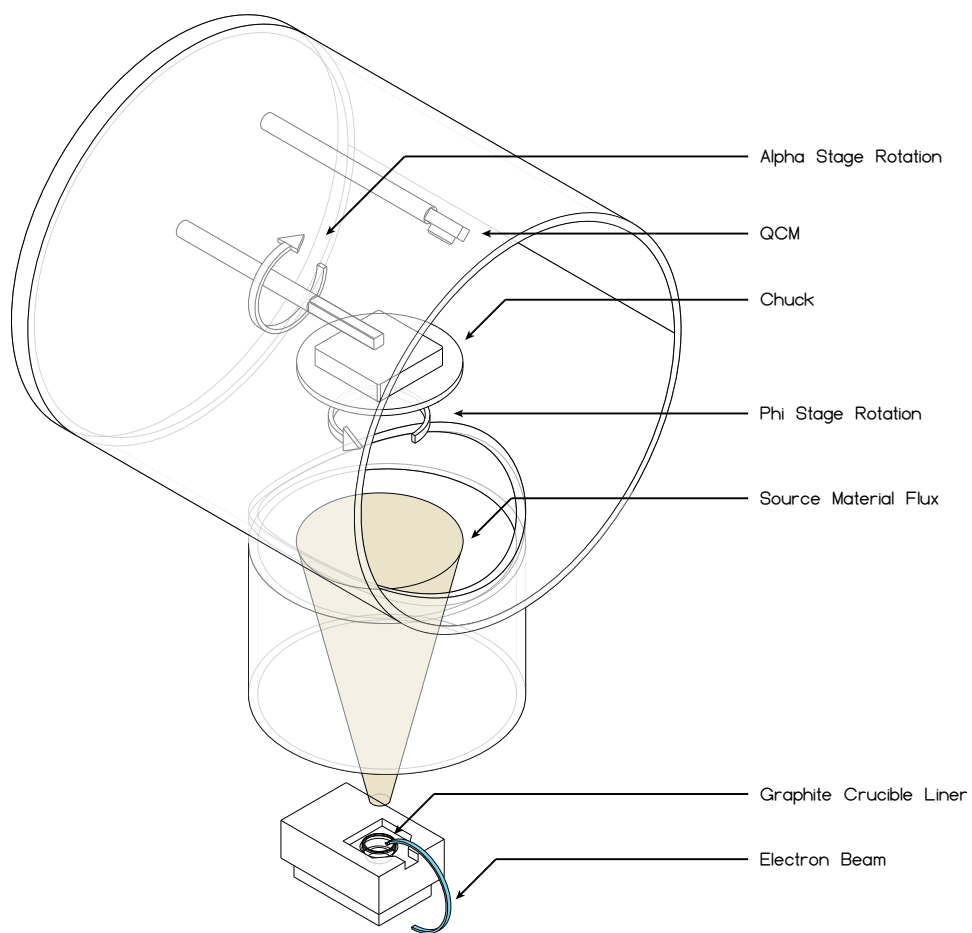
Figure 1.3: Simplified diagram of an electron-beam evaporation GLAD system.
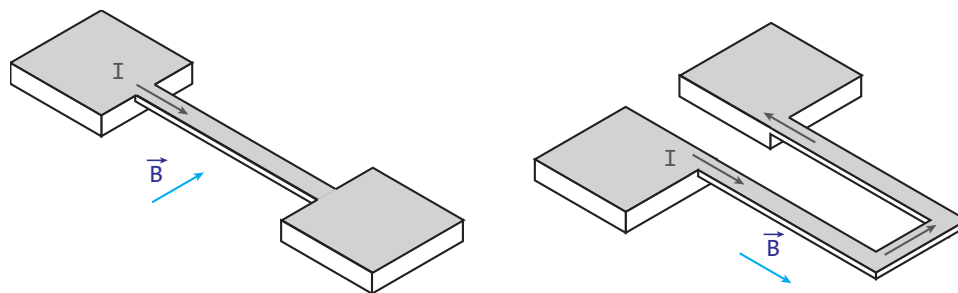
Figure 1.4: Left: Doubly-clamped beam resonator. Right: U-cantilever resonator.

Chapter 2

Device Modelling

Before device fabrication and measurement can be done, we must develop
a mathematical model for the operation of our devices. Such modelling is
important because it places results into context – understanding how our
devices *should* respond better equips us to interpret our results. Further-
more, modelling yields a first approximation as to the types and magnitudes
of signals that we expect to be present in our experiment, hence informing
the design of the apparatus and of the device itself.

In this section of the thesis, we begin with a discussion of modelling
resonator behaviour in the mechanical domain. We then move to a discussion
of device modelling from an electronic perspective, emphasizing how, in
the magnetomotive scheme, the Lorentz force bridges the mechanical and
electrical domains, transducing resonator motion into an electrical signal.
Assuming that the resonator is well approximated as a damped and driven
1-degree-of-freedom (1DOF) simple harmonic oscillator, we derive models
for the frequency-dependent electrical impedance of metallized U-cantilever
and doubly-clamped beam resonators immersed in a uniform magnetic field.
The results of this section reveal that our devices should produce very small
– but measurable – shifts in electrical impedance at resonance.

2.1 Background: Euler-Bernoulli Beam Theory

The study of the transverse vibration of mechanical structures begins with the Euler-Bernoulli beam theory, which describes the flexure of a linear elastic beam under small displacements. In this section, we review a number of key equations that govern the behaviour of the classical linear elastic beam, with an eye towards the assumptions and simplifications made. We will then adapt the classical beam theory to the *dynamic* problem of a driven, vibrating beam. This section, along with the following background sections, are heavily referenced from [35–37].

2.1.1 The Flexure Formula

Working through the development of the theory of linear elastic bending is essential to understanding how to adapt these mathematical tools to model the types of structures present in functionalized NEMS resonant sensors. In order to develop a simple model for the bending deformation of a linear elastic beam, we begin with a few key assumptions:

- Along the length of the beam there exists a *neutral surface* which exhibits zero change in length in the longitudinal direction.

- The longitudinal axis, which lies in the neutral surface, does not undergo a change in length under bending, but becomes a curve. This axis passes through the centroid of each cross-section.

- All cross-sections of the beam remain planar and perpendicular to the longitudinal axis under bending. Furthermore, any deformation of these cross-sections in their own plane are neglected.

Figure 2.1 illustrates an example of such a beam under bending.

Taking into consideration a small cross-sectional slice of the beam of width Δs, as illustrated in Figure 2.2, we find that a small bending deformation yields a strain that is linear in the distance y from the neutral surface. The basic formula for this strain is as follows:
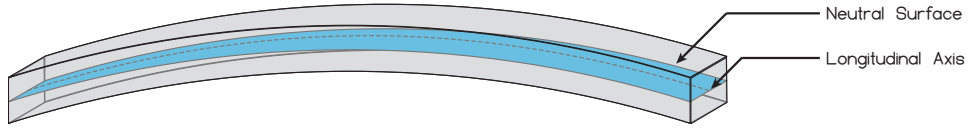
Figure 2.1: Simplified model of a linear elastic beam under flexure. The neutral surface is shown in blue.

$$\epsilon(y) = \lim_{\Delta s -> 0} \frac{\Delta s'(y) - \Delta s}{\Delta s} \tag{2.1}$$

Taking $\Delta\theta$ as the angle between the two faces of the cross-section, ρ as the radius of curvature of bending, Δs as the original width of the segment, and $\Delta s'(y)$ as the deformed width of the segment as a function of y, we realize that $\Delta s = \rho\Delta\theta$ and $\Delta s'(y) = (\rho - y)\Delta\theta$, giving:

$$\epsilon(y) = \lim_{\Delta\theta -> 0} \frac{(\rho - y)\Delta\theta - \rho\Delta\theta}{\rho\Delta\theta} = -\frac{y}{\rho} \tag{2.2}$$

As the material of the beam is assumed to be linear elastic, this linear distribution of strain gives rise to a (potentially piece-wise) linear stress distribution, proportional to the strain through the Young's modulus, E.

At the point on the cross-section farthest from the neutral axis (labelled with distance c), the strain reaches its maximum value of $\epsilon_{\max}$, with a corresponding stress of $\sigma_{\max} = E\epsilon_{\max}$. Requiring the net moment applied to the cross-section by the stress distribution to be equal to the internal bending
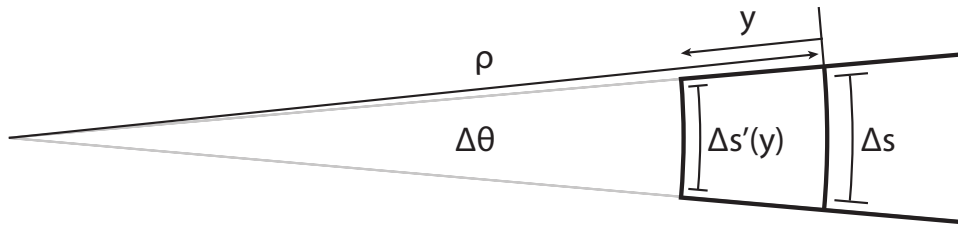
Figure 2.2: Geometry of a small cross-section of the beam, deflected along a circle of radius of curvature ρ. The neutral axis has an arc length of Δs, unchanged from the undeflected case.

14

moment M, we obtain:

$$M = \int_A y \, dF = \int_A y(\sigma(y) dA) = \int_A y(\frac{y}{c}\sigma_{\max}) dA = \frac{\sigma_{\max}}{c} \int_A y^2 \, dA \quad (2.3)$$

Identifying $\int_A y^2 \, dA$ as the second moment of area I of the cross-section, we obtain:

$$\sigma_{\max} = \frac{Mc}{I} \quad (2.4)$$

Realizing that $\sigma(y) = -\frac{y}{c}\sigma_{\max}$ and substituting for $\sigma_{\max}$, we obtain the *Flexure Formula*, which relates the cross-sectional geometry of the beam (through I), and the internal bending moment to the stress distribution in the beam:

$$\sigma(y) = -\frac{My}{I} \quad (2.5)$$

This formula lies at the core of the Euler-Bernoulli beam theory.

2.1.2 Beam Deflection

Noting again that $\sigma(y) = E\epsilon(y)$, substitution of the flexure formula (2.5) for $\epsilon(y)$ in (2.2) gives the relationship between the local curvature of the beam (described by ρ) and the internal bending moment M:

$$\frac{1}{\rho} = \frac{M}{EI} \quad (2.6)$$

From differential calculus, we have the following formula for the radius of curvature of a curve $y = w(x)$:

$$\frac{1}{\rho} = \frac{d^2w/dx^2}{[1 + (dw/dx)^2]^{3/2}} \quad (2.7)$$

Let $w(x)$ be the curve describing the deflection of the beam under a static load. For our purposes, the deflection w and its associated slope dw/dx can be assumed small. Thus, the simplification $(1 + (dw/dx)^2) \approx 1$

holds, simplifying (2.7) to:

$$\frac{1}{\rho} = \frac{d^2 w}{dx^2} \tag{2.8}$$

Combining the above equation with (2.6) yields a second-order differential equation for the beam deflection $w(x)$ as a function of the internal bending moment $M(x)$:

$$\frac{d^2 w}{dx^2} = \frac{M(x)}{EI} \tag{2.9}$$

Where, in general, both E and I are functions of x as well.

Finally, consider the free-body diagram for a small segment of the deflected beam experiencing a distributed load $p(x)$. This segment experiences internal shear forces (V and $V + dV$), bending moments (M and $M + dM$), and a force due to the distributed load, $p(x)dx$. These forces are labeled in accordance with the standard sign convention in Figure. 2.3.

For static equilibrium, we require the net force and moment on the segment to be zero. Force balance yields $V - (V + dV) - p(x)dx = 0$, or:

$$\frac{dV}{dx} = -p(x) \tag{2.10}$$

Likewise, the condition of zero net moment yields $M - (M + dM) + V dx = 0$, or:
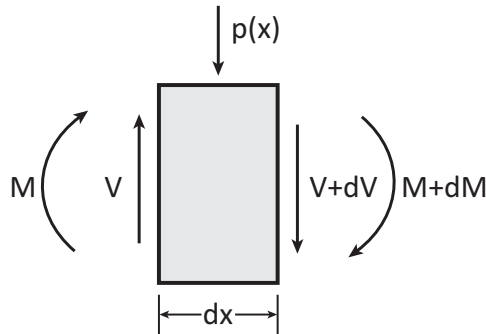
Figure 2.3: Forces and moments on a segment of length dx along the beam.

$$\frac{dM}{dx} = V \tag{2.11}$$

Substituting (2.10) and (2.11) into (2.9) gives the *Euler-Bernoulli Beam Equation*:

$$\frac{d^2}{dx^2}[EI\frac{d^2w}{dx^2}] = p(x) \tag{2.12}$$

This equation, along with boundary conditions, approximates the curve of deflection of a linear elastic beam under an arbitrary applied loading.

2.2 Background: The Dynamic Beam Equation

Beam structures for application in resonant sensors exhibit very little mechanical loss or damping. The amount of damping present in a mechanical resonator is typically communicated using the *quality factor*, denoted Q. The quality factor represents the ratio of the energy stored in the resonator (due to potential and/or kinetic energy) to the energy dissipated per cycle:

$$Q = 2\pi \times \frac{\text{Stored Energy}}{\text{Dissipated Energy per Cycle}} \tag{2.13}$$

Quality factors for mechanical resonant sensors in vacuum easily exceed 10^3, and in the domain of resonant NEMS structures can exceed 10^5, indicating that very little energy is lost due to damping. As a consequence, we may assume the damping forces themselves are small. Thus, for the purposes of modeling the dynamics of beam vibration, we may neglect any effect that this small damping might have on both beam mode-shapes and resonant frequencies.

In the absence of damping, the Euler-Bernoulli beam, taken together with its boundary conditions, represents a physical system subject only to *holonomic* constraints; that is, all constraints of the system are functions *solely* of position and time. As a result, we may neglect damping forces while applying *D'Alembert's principle*, which states that a mechanical system in motion may be analyzed in the manner of a system in equilibrium, so long

as *inertial forces* are introduced into the analysis. These *inertial forces* are simply products of mass and (negative) acceleration, written as:

$$F_{\text{inertial}} = -m_i \ddot{x}_i \qquad (2.14)$$

for some particle i.

The static beam equation (2.12) is, essentially, the equation of force equilibrium for an infinitesimally thin slice of the beam at length-coordinate x. If we denote the area of the cross-section of the beam by $\Omega(x)$, and the mass density by $\rho(x)$, the *inertial force* due to transverse motion of the slice of the beam at x is given by:

$$F_{\text{inertial}}(x) = -\rho(x)\Omega(x)\frac{d^2 w(x,t)}{dt^2} \qquad (2.15)$$

Adding this force to the applied force $p(x)$ in equation (2.12) yields the *Dynamic Beam Equation*:

$$\frac{d^2}{dx^2}\left[E(x)I(x)\frac{d^2 w(x,t)}{dx^2}\right] = p(x,t) - \rho(x)\Omega(x)\frac{d^2 w(x,t)}{dt^2} \qquad (2.16)$$

wherein the position and time dependence of each variable has been made explicit. This equation fully describes the *forced vibration* (through $p(x,t)$) of a lossless Euler-Bernoulli beam, and represents a good approximation to the behaviour of a real beam with low-damping (large Q) oscillating with a small amplitude – precisely the situation present in resonant MEMS and NEMS sensors.

2.2.1 Determination of Resonant Frequency and Mode-Shapes

For simplicity, we assume that E, I, ρ, and Ω are constants, and that the beam undergoes free vibrations; that is, $p(x,t) = 0$. In this situation, the dynamic beam equation reads:

$$\frac{d^2}{dx^2}\left[EI\frac{d^2 w(x,t)}{dx^2}\right] = -\rho\Omega\frac{d^2 w(x,t)}{dt^2} \qquad (2.17)$$

Applying the method of separation of variables (making the substitution $w(x,t) = X(x)T(t)$), we obtain the following ODEs for the modal space and time dependence:

$$\frac{d^2}{dx^2}[EI\frac{d^2X(x)}{dx^2}] - \omega^2\rho\Omega X(x) = 0 \tag{2.18}$$

$$\frac{d^2T(t)}{dt^2} + \omega^2 T(t) = 0 \tag{2.19}$$

The solution to equation (2.19) is simply:

$$T(t) = A\cos(\omega t) + B\sin(\omega t) \tag{2.20}$$

Indicating that mode vibrations are time-harmonic, as expected.

From equation (2.18), the mode-shapes and resonant frequencies are determined by the eigenfunctions $X_n(x)$ and eigenvalues ω_n^2 of the following operator:

$$O\left\{X(x)\right\} = \frac{1}{\rho(x)\Omega x}\frac{\partial^2}{\partial x^2}\left[E(x)I(x)\frac{\partial^2 X(x)}{\partial x^2}\right] \tag{2.21}$$

Together with the boundary conditions for the beam, equation (2.21) represents a boundary value problem (BVP), the solution to which yields the resonant mode-shapes and frequencies. In general, this BVP must be solved numerically; however, for the case of a rectangular beam of constant cross section clamped on one or both ends, it may be solved analytically.

For the case of the singly-clamped beam (cantilever beam) which is clamped at $x = 0$, we have the following boundary conditions:

$$w(0,t) = 0 \qquad\qquad \frac{\partial w}{\partial x}(0,t) = 0$$

$$\frac{\partial^2 w}{\partial x^2}(L,t) = 0 \qquad\qquad \frac{\partial^3 w}{\partial x^3}(L,t) = 0$$

The setup is illustrated in Figure. 2.4.
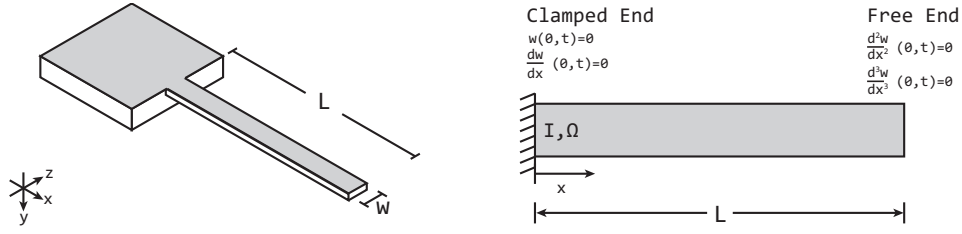
Figure 2.4: Singly-clamped cantilever beam with boundary conditions.

Application of these boundary conditions yields the frequency determining equation:

$$\cos(k_n L)\cosh(k_n L) = -1 \tag{2.22}$$

Each positive root k_n of this equation determines the frequency of vibration of a single resonant mode through the following relation:

$$\omega_n = k_n^2 \sqrt{\frac{EI}{\rho\Omega}} \tag{2.23}$$

And the mode-shape of the n-th mode is given by the following:

$$X_n(x) = \Big\{ \cosh(k_n x) - \cos(k_n x)$$
$$- \frac{\cos(k_n L) + \cosh(k_n L)}{\sin(k_n L) + \sinh(k_n L)} \left[\sinh(k_n x) - \sin(k_n x)\right] \Big\} \tag{2.24}$$

Similarly, for the case of the doubly-clamped beam (clamped at $x = 0$ and $x = L$), we have the following boundary conditions:

$$w(0, t) = 0 \qquad\qquad \frac{\partial w}{\partial x}(0, t) = 0$$

$$w(L, t) = 0 \qquad\qquad \frac{\partial w}{\partial x}(L, t) = 0$$

20

Yielding the following frequency determining equation:

$$\cos(k_n L)\cosh(k_n L) = 1 \qquad (2.25)$$

With the same relationship between k_n and ω_n as elaborated above. The mode-shape is as follows:

$$X_n(x) = \left\{ \cosh(k_n x) - \cos(k_n x) \right.$$
$$\left. - \frac{\cos(k_n L) - \cosh(k_n L)}{\sin(k_n L) - \sinh(k_n L)} \left[\sinh(k_n x) - \sin(k_n x)\right] \right\} \qquad (2.26)$$

For both cases outlined above, the solution for the equation of motion of the beam is given simply by a linear combination of these resonant modes:

$$w(x,t) = \sum_{n=1}^{\infty} X_n(x)\left[A_n \cos(\omega_n t) + B_n \sin(\omega_n t)\right] \qquad (2.27)$$

This solution, though precise, is rather difficult to work with directly due to the complexity of calculation. For the purposes of modelling a driven resonant beam, we will apply a considerably simpler but less precise model that encapsulates the most relevant dynamics of the system. The precise solution given above will serve as a check to this model to verify that the approximations made are acceptable.

2.3 Background: The 1DOF Damped Simple Harmonic Oscillator Approximation

As we can see from eqn. (2.27), each resonant mode of our device will independently undergo simple harmonic motion. Under normal operation, we will excite only one resonant mode in our devices, meaning that the motion will take the form:

$$w(x,t) = X_1(x) \left[A_1 \cos(\omega_1 t) + B_1 \sin(\omega_1 t) \right]$$
$$= C \times X_1(x) \cos(\omega_1 t + \phi) \tag{2.28}$$

Assuming that we only excite a single resonant mode, we introduce the effect of damping by modelling the mode as a driven, one degree-of-freedom (1DOF) damped simple harmonic oscillator. This sort of approximation is applied to great effect in the modelling of micromechanical resonators. [17] The equation of motion for such an oscillator is as follows:

$$\ddot{y} + \frac{\omega_0}{Q}\dot{y} + \omega_0^2 y = F(t)/m \tag{2.29}$$

Where $F(t) = A \times \cos(\omega t + \phi)$ is a harmonic driving force, ω_0 is the resonant frequency of the oscillator, and Q is the quality factor. We typically choose y to refer to the displacement at the end of the resonator. Note that, from the spring-and-mass model for the damped SHO, $\omega_0^2 = k/m$, where k is an *effective* spring constant for the system, and m is an *effective* mass.

Employing the Fourier transform and simplifying, we obtain the following frequency-domain representation for eqn. (2.29):

$$Y(j\omega) = \frac{F(j\omega)/m}{\omega_0^2 - \omega^2 + j\frac{\omega_0 \omega}{Q}} \tag{2.30}$$

Note that the amplitude of oscillation at resonance is given by:

$$\|Y(j\omega)\| = \left\| \frac{F(j\omega)/m}{j\frac{\omega_0^2}{Q}} \right\|$$
$$= \frac{\|F\|/m}{k/m} \times Q \tag{2.31}$$
$$= \|F\|/k \times Q$$

Eqn. (2.31) indicates that the amplitude of oscillation of y, when driven at its resonant frequency by a harmonic force F, is Q times the static displacement of y under application of a static force F.

2.4 Modelling the U-Cantilever Resonator

The U-cantilever resonator is illustrated in Figure. 2.5. The resonator is immersed in a static, uniform magnetic field with flux density B. A time-harmonic current I flows around the loop. In the cross-piece of the "U", the current flow is perpendicular to the magnetic field, generating a Lorentz force which is used to drive the structure into mechanical resonance. This resonance causes the magnetic flux through the loop to vary with time, creating a back EMF which we can use to electronically detect the device motion. Analysis proceeds using the sort of lumped-model analysis described in [17], with an eye towards estimating the effect of changing device parameters on the ultimate measured response.

2.4.1 A Simple Model for the U-Cantilever Resonator

To simplify our calculations, we will treat the U-cantilever as two singly-clamped cantilevers. Beginning with the equation of motion for a 1DOF damped harmonic oscillator, driven by a force F (eqn. (2.29)), we take the position variable y to refer to the displacement of the end of the cantilever from horizontal. To apply this model to the motion of the cantilever, we need to determine the value of the equivalent mass m. This equivalent mass is derived by finding a "spring constant" that relates a *static* force applied to the end of the cantilever to the *static* displacement of the cantilever. The setup is illustrated in Figure. 2.6.

Applying eqn. (2.12) with the boundary conditions for the singly clamped beam gives the displacement y of the end of the beam under a concentrated loading F as:

$$y = -\frac{FL^3}{3EI} \tag{2.32}$$

Rearranging, we have $F = -\frac{3EI}{L^3}y = -ky$, giving the effective spring constant k of a single beam:

$$k = \frac{3EI}{L^3} \tag{2.33}$$
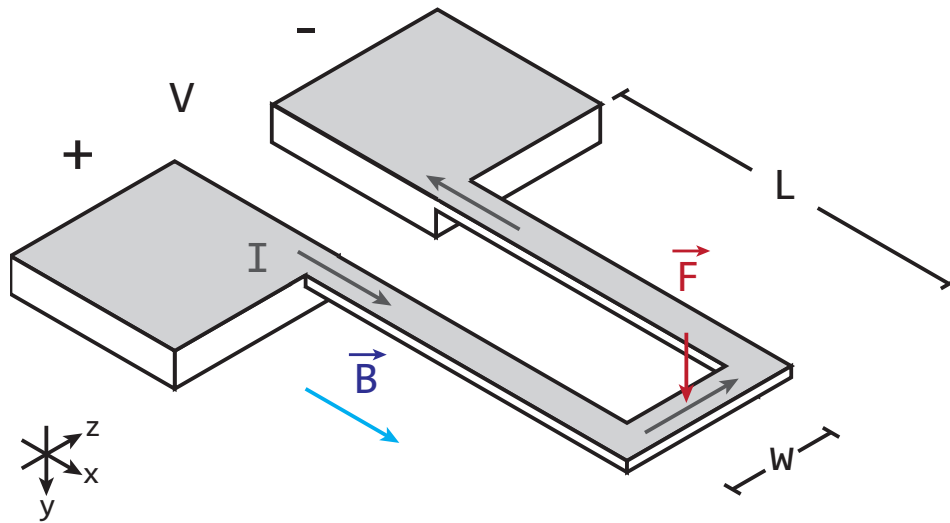
Figure 2.5: U-cantilever resonator with important quantities labelled.
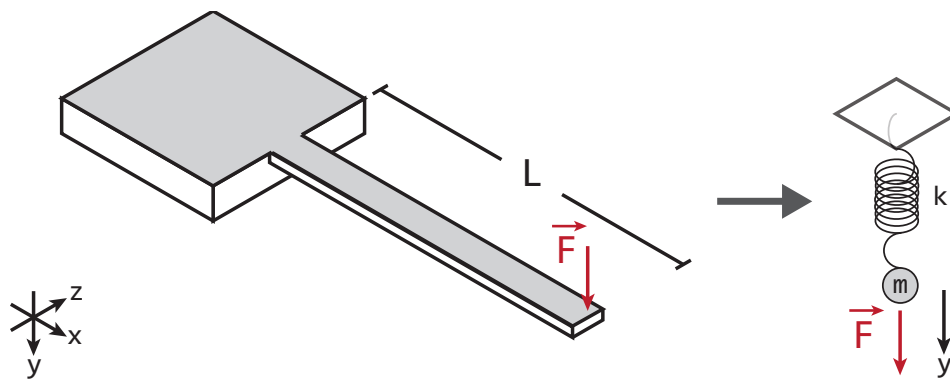
Figure 2.6: Modelling one half of the U-cantilever structure as a spring-and-mass system.

As our system consists of two parallel cantilever beams that share an applied force, our effective spring constant is $k' = 2k$.

From studying the simple harmonic oscillator, we have $m = k'/\omega_0^2$. From eqn. (2.22) and (2.23), we have $\omega_0 = k_1^2 \sqrt{\frac{EI}{\rho\Omega}}$, where $k_1 \approx 1.875/L$ is the first root of the frequency-determining equation (2.22). Combining these equations gives the effective mass:

$$m = \frac{6EI}{\omega_0^2 L^3} \tag{2.34}$$

Next, we assume a time-harmonic current $I(j\omega)$ flows through the resonator. This current generates a Lorentz force $F = IwB$, where w is the width of the cross-piece. Substituting for F in (2.30), we obtain the frequency-domain transfer function between applied current I and the mechanical displacement Y at the end of the resonator:

$$\frac{Y(j\omega)}{I(j\omega)} = \frac{wB}{m} \frac{1}{\omega_0^2 - \omega^2 + j\frac{\omega_0 \omega}{Q}} \tag{2.35}$$

With this current flowing, a voltage will develop across the resonator drive terminals. This voltage will be the sum of the voltage drop due to resistive losses in the conduction path, as well as a back-EMF due to the time-varying magnetic flux through the loop of the "U" as it vibrates. The magnetic flux $\Phi(j\omega)$ through the loop is well-approximated by the following expression:

$$\Phi(j\omega) = B \cdot w \cdot Y(j\omega) \tag{2.36}$$

Where w is the width of the loop. Applying Faraday's law, we arrive at the induced EMF:

$$\begin{aligned}
\epsilon(j\omega) = &- \dot{\Phi}(j\omega) = -j\omega\Phi(j\omega) \\
= &- j\omega Bw \cdot Y(j\omega)
\end{aligned} \tag{2.37}$$

Thus, the total voltage developed across the resonator terminals due to an applied time-harmonic current $I(j\omega)$ is given by the following:

$$
\begin{aligned}
V(j\omega) &= I(j\omega)R + \epsilon(j\omega) \\
&= I(j\omega)R - j\omega Bw \cdot Y(j\omega) \\
&= I(j\omega)R - j\omega \cdot \frac{w^2 \cdot B^2 \cdot I(j\omega)}{m} \frac{1}{\omega_0^2 - \omega^2 + j\frac{\omega_0\omega}{Q}}
\end{aligned}
\tag{2.38}
$$

Finally, we can determine the impedance $Z(j\omega) = V(j\omega)/I(j\omega)$ as a function of frequency:

$$
Z(j\omega) = R - j\omega \cdot \frac{w^2 \cdot B^2}{m} \frac{1}{\omega_0^2 - \omega^2 + j\frac{\omega_0\omega}{Q}}
\tag{2.39}
$$

At resonance, the impedance of the device will be real, and attains its peak deviation from the DC resistance R. Setting $\omega = \omega_0$, we obtain:

$$
Z_{\text{resonance}} = R - Q\frac{w^2 B^2}{m\omega_0}
\tag{2.40}
$$

Substituting for ω_0 and m yields the following:

$$
Z_{\text{resonance}} = R - QC_1\frac{w^2 B^2 L}{6\sqrt{EI\rho\Omega}}
\tag{2.41}
$$

In which $C_1 \approx (1.875)^2$ is a constant.

The peak deviation in impedance at resonance $\Delta Z_{\text{resonance}}$ from the DC impedance R is then:

$$
\Delta Z_{\text{resonance}} = -QC_1\frac{w^2 B^2 L}{6\sqrt{EI\rho\Omega}}
\tag{2.42}
$$

From (2.42) we can make a number of observations. First of all, higher Q resonators experience a larger change in impedance at resonance than lower Q resonators. This makes sense – higher Q resonators experience a greater amplitude of oscillation at resonance (eqn. (2.31)), thereby experiencing a larger motional EMF which acts to reduce the impedance seen at the device terminals.

Perhaps unsurprisingly, longer (higher L) and wider (higher w) res-

onators produce a larger response. As the deviation in impedance is proportional to w, we can compensate for reducing the length of the resonator by a factor of two by increasing the device width by a factor of $\sqrt{2}$. This rule-of-thumb is useful for dimensioning U-cantilever resonators.

At this point, we are well-equipped to estimate the electronic behavior of a U-cantilever resonator. For the sake of illustration, consider a rather large resonator with $L = 10$ μm, $w = 3$ μm, $E = 165$ GPa (the Young's modulus of silicon), a density of $\rho = 2330$ kg/m^3, a beam-width of $b = 1$ μm, and a beam thickness of $t = 145$ nm. For this resonator, $\Omega = b \cdot t$ and $I = b \cdot t^3/12$. Furthermore, assume that the magnetic field strength is 1 T and that $Q = 1000$. Substituting, we obtain:

$$\Delta Z_{\text{resonance}} = -443\text{m}\Omega$$

For comparison, let us estimate R. We will assume that the cantilever is metallized using an aluminum thin film with a thickness of $20nm$. Furthermore, for simplicity, we will assume the aluminum film exhibits the same resistivity as the bulk material. Bulk aluminum has a resistivity of $\rho = 2.7 \times 10^{-8}$ $\Omega \cdot m$. The sheet resistance for the 20 nm thick film is then $R_s = \rho/t = 1.35$ Ω/square. Dividing the cantilever surface into squares of side-length 1 μm, we count a total of 23 squares, meaning that the resistance R of the structure is roughly $R = 23 \times R_s = 31$ Ω, meaning that

$$\frac{\Delta Z}{Z} = -1.43\%$$

demonstrating that, even for large resonators, the change of impedance at resonance is minuscule. Performing the above calculations, again, for a resonator of length $L = 5$ μm and $w = 1$ μm gives an impedance change of only -0.02% at resonance! Detecting these minuscule impedance shifts is the subject of Chapter 5.

2.4.2 A More Accurate Model for the U-Cantilever

The model in section 2.4.1 is useful in that it provides a rough, qualitative description of the behavior of the U-cantilever resonator. Unfortunately, it is not quantitatively accurate, as it neglects the presence of the cross-beam entirely. The cross-beam is expected to have a large effect on the resonant frequency of the structure, due to its effective mass-loading of the end of the beam. The presence of this additional mass is expected to lower the resonant frequency of the beam, with the effect being larger the wider (and thus, more massive) the cross-bar. For design and analysis of our resonators, we would benefit greatly from a more accurate method for determining ω_0.

We can obtain a more accurate model for the resonant frequency of the U cantilever resonator by considering the mechanical effect of the cross-bar. We begin by assuming the cantilever deflects only in the y direction (down), and that this deflection is independent of z. Next, consider the cross-section half-way along the cross-bar when the resonator is vibrating in its fundamental mode. Due to symmetry, there should be zero stress on this cross-section. As a result, we can split the U-cantilever down the middle, and consider only one half of the structure.

We proceed to model the half-cantilever as a multi-span beam, as shown in Figure. 2.7. Examples of similar analysis of multi-span beam vibration abound in the literature of civil and mechanical engineering. [38] [39] Herein, we solve this problem in the context of the U-cantilever resonator. The first span of the beam consists of the cantilever arm of length $L_1 = L - b$ and width b, while the second span consists of the half-cross-bar of length $L_2 = b$ and width $w/2+b$. These two beam sections will have different area moments of inertia $I^{(1)}, I^{(2)}$, as well as different cross-sectional areas $\Omega^{(1)}, \Omega^{(2)}$. In the interest of simplifying calculations, we reference the position x along the first span from the left of the beam, and the position x' along the second span from the right.

Under free vibration, the deflection $w^{(1)}, w^{(2)}$ of each span must independently satisfy the dynamic beam equation; namely,
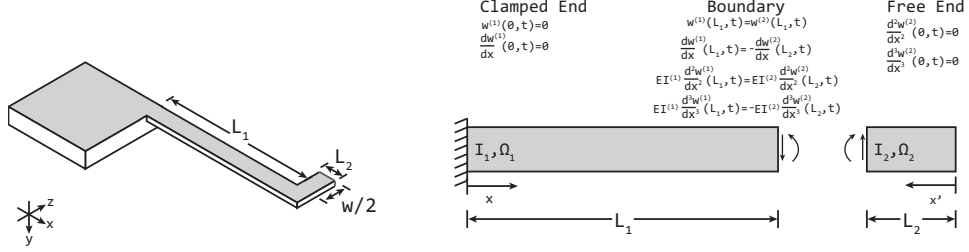
Figure 2.7: Multi-span beam model for the U-Cantilever resonator. Important quantities and boundary conditions are labeled on the diagram.

$$\frac{\partial^4 w^{(1,2)}(x,t)}{\partial x^4} + \frac{\rho\Omega^{(1,2)}}{EI^{(1,2)}}\frac{\partial^2 w^{(1,2)}(x,t)}{\partial t^2} = 0 \tag{2.43}$$

Applying separation of variables as in subsection 2.2.1, we find that the solutions $w_n^{(1,2)}(x,t)$ may be expressed as the product of a time-independent modeshape function $X_n^{(1,2)}(x)$ and a position-independent time-harmonic function $T_n^{(1,2)}(t) = A_n^{(1,2)}\cos(\omega_n^{(1,2)}t) + B_n^{(1,2)}\sin(\omega_n^{(1,2)}t)$. From here on, we will only consider the fundamental mode, where $n = 1$. The most general expression for the modeshape function $X^{(1,2)}(x)$ is:

$$\begin{aligned}X^{(1,2)}(x) =&C_1^{(1,2)}\cos(k^{(1,2)}x) + C_2^{(1,2)}\cosh(k^{(1,2)}x)\\ &+ C_3^{(1,2)}\sin(k^{(1,2)}x) + C_4^{(1,2)}\sinh(k^{(1,2)}x)\end{aligned} \tag{2.44}$$

in which $\omega^{2(1,2)} = k^{4(1,2)} = \frac{\rho\Omega^{(1,2)}}{EI^{(1,2)}}$, and $C_1^{(1,2)}$ through $C_4^{(1,2)}$ are constants.

The boundary conditions at the clamped end force $C_2^{(1)} = -C_1^{(1)}$ and $C_4^{(1)} = -C_3^{(1)}$, meaning $X^{(1)}$ has the form

$$\begin{aligned}X^{(1)}(x) =&C_1^{(1)}\left[\cos(k^{(1)}x) - \cosh(k^{(1)}x)\right]\\ &+C_3^{(1)}\left[\sin(k^{(1)}x) - \sinh(k^{(1)}x)\right]\end{aligned} \tag{2.45}$$

Similarly, the boundary conditions on the free end impose $C_1^{(2)} = C_2^{(2)}$ and $C_3^{(2)} = C_4^{(2)}$, meaning $X^{(2)}$ has the form

$$X^{(2)}(x') = C_1^{(2)} \left[\cos(k^{(2)}x') + \cosh(k^{(2)}x') \right]$$
$$+ C_3^{(2)} \left[\sin(k^{(2)}x') + \sinh(k^{(2)}x') \right] \tag{2.46}$$

Imposition of the boundary conditions at the interface between the two spans results in the following matrix equation:

$$\mathbf{A}\vec{\mathbf{C}} = \mathbf{0} \tag{2.47}$$

in which $\vec{\mathbf{C}}$ is the vector of constants

$$\vec{\mathbf{C}} = \begin{Bmatrix} C_1^{(1)} \\ C_3^{(1)} \\ C_1^{(2)} \\ C_3^{(2)} \end{Bmatrix} \tag{2.48}$$

and $\mathbf{A}$ is given by the following:

$$\mathbf{A} = \begin{bmatrix} A_{11} & A_{12} & A_{13} & A_{14} \\ A_{21} & A_{22} & A_{23} & A_{24} \\ A_{31} & A_{32} & A_{33} & A_{34} \\ A_{41} & A_{42} & A_{43} & A_{44} \end{bmatrix} \tag{2.49}$$

where

$A_{11} = \cos(k^{(1)}L_1) - \cosh(k^{(1)}L_1)$

$A_{12} = \sin(k^{(1)}L_1) - \sinh(k^{(1)}L_1)$

$A_{13} = - \left[\cos(k^{(2)}L_2) + \cosh(k^{(2)}L_2) \right]$

$A_{14} = - \left[\sin(k^{(2)}L_2) + \sinh(k^{(2)}L_2) \right]$

$A_{21} = k^{(1)} \left[-\sin(k^{(1)}L_1) - \sinh(k^{(1)}L_1) \right]$

$A_{22} = k^{(1)} \left[\cos(k^{(1)}L_1) - \cosh(k^{(1)}L_1) \right]$

$A_{23} = k^{(2)} \left[-\sin(k^{(2)}L_2) + \sinh(k^{(2)}L_2) \right]$

$A_{24} = k^{(2)} \left[\cos(k^{(2)}L_2) + \cosh(k^{(2)}L_2) \right]$

$A_{31} = I^{(1)}k^{2(1)} \left[-\cos(k^{(1)}L_1) - \cosh(k^{(1)}L_1) \right]$

$A_{32} = I^{(1)}k^{2(1)} \left[-\sin(k^{(1)}L_1) - \sinh(k^{(1)}L_1) \right]$

$A_{33} = -I^{(2)}k^{2(2)} \left[-\cos(k^{(2)}L_2) + \cosh(k^{(2)}L_2) \right]$

$A_{34} = -I^{(2)}k^{2(2)} \left[-\sin(k^{(2)}L_2) + \sinh(k^{(2)}L_2) \right]$

$A_{41} = I^{(1)}k^{3(1)} \left[\sin(k^{(1)}L_1) - \sinh(k^{(1)}L_1) \right]$

$A_{42} = I^{(1)}k^{3(1)} \left[-\cos(k^{(1)}L_1) - \cosh(k^{(1)}L_1) \right]$

$A_{43} = I^{(2)}k^{3(2)} \left[\sin(k^{(2)}L_2) + \sinh(k^{(2)}L_2) \right]$

$A_{44} = I^{(2)}k^{3(2)} \left[-\cos(k^{(2)}L_2) + \cosh(k^{(2)}L_2) \right]$

Let $\det \mathbf{A} = f(k^{(1)}, k^{(2)})$. For non-trivial solutions, we require

$$f(k^{(1)}, k^{(2)}) = 0 \tag{2.50}$$

We reduce the dimensionality of the problem by recognizing that the fact that $\omega^{(1)} = \omega^{(2)}$ fixes the ratio of $k^{(1)}$ and $k^{(2)}$. In fact, we have

$$k_r = \frac{k^{(2)}}{k^{(1)}} = \left(\frac{I^{(1)}}{I^{(2)}} \times \frac{w/2 + b}{b} \right)^{1/4} \tag{2.51}$$

Thus, we have reduced the problem to a one-dimensional root finding problem, i.e., finding k such that

$$g(k) = f(k, k \cdot k_r) = 0 \tag{2.52}$$

For the sake of computation, we may use $k_{\text{est}} = 1.875/(L_1 + L_2)$ from the basic cantilever model as an initial guess for k. At this point, any one-dimensional root-finding algorithm may be used to compute k. Once k is determined, the resonant frequency f_0 follows as

$$f_0 = \frac{\omega_0}{2\pi} = \frac{k^2}{2\pi} \sqrt{\frac{EI^{(1)}}{\rho \Omega^{(1)}}} \tag{2.53}$$

A MATLAB implementation of this technique is included as Appendix A. Note that care must be taken to ensure the condition number of $\mathbf{A}$ is kept small. See the included code for the details of our approach.

To verify this model, we check the resonant frequencies calculated using eqn. (2.53) against predictions made by finite element modeling (FEM). Resonators with $t = 145$ nm, $b = 1$ μm, $L = 2, 3, 4, 5, 7$ and 10 μm and $w = 1, 3$ and 5 μm were meshed, and an eigenvalue analysis was run using Elmer. [40] Zero-displacement boundary conditions were applied at the clamped end. For the purposes of analysis, $E = 165$ GPa, $\rho = 2330$ kg/m^3, and $v = 0.22$.

Figure. 2.8 pictures one of the meshes from the FEM survey. FEM analysis produces both an eigenmode (mode-shape) as well as an eigenvalue λ, which must be converted into a resonant frequency. The eigenvalues are

Mesh for FEM Analysis
W=5 μm, L=10 μm

Eigenmode from FEM Analysis
$\lambda = 8.215359 \times 10^{13}$
f = 1.44 MHz

Zero-Displacement
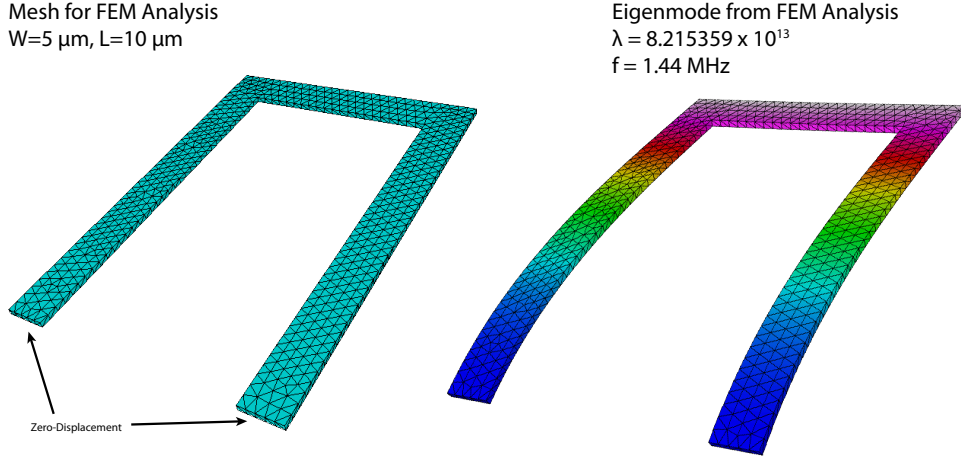
Figure 2.8: FEM mesh (left) and corresponding eigenmode solution (right).

related to frequency by the following:

$$f = \sqrt{\lambda}/2\pi \tag{2.54}$$

Calculated frequencies from our model are compared with the frequencies predicted by FEM in Figure. 2.9. The formula used to calculate percent difference (error) for the sake of our comparison is

$$\text{Percent Error } (\%) = \frac{f_{\text{model}} - f_{\text{FEM}}}{f_{\text{FEM}}} \times 100\% \tag{2.55}$$

From the plot in Figure. 2.9 we immediately note that long and narrow resonators agree extremely well with our model, while shorter and wider resonators deviate substantially from what we would expect. A plot of percent error vs. aspect ratio (Figure. 2.10) reveals this trend in more detail.

Figure. 2.10 makes clear the relationship between model accuracy and aspect ratio. Resonators with aspect ratio > 1 are within $\pm 1\%$ of our model, while resonators with aspect ratio < 1 do not agree with our calculations. The trouble is that the assumption that the resonator deflection is independent of z breaks down as the resonators become short and wide.

Consider, for example, the extreme case where the resonator is composed
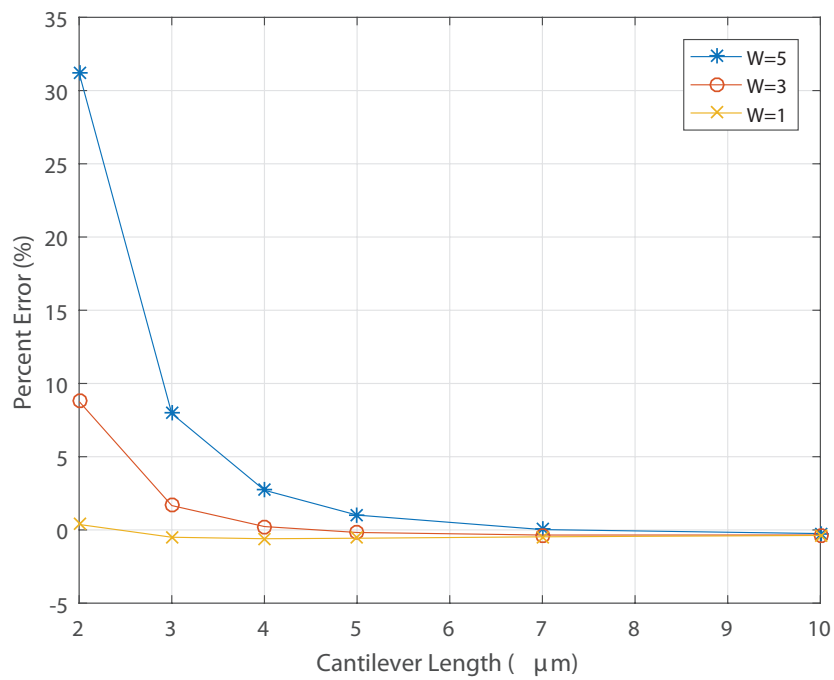
Figure 2.9: Percent difference (error) between FEM-calculated resonant frequencies and those predicted by our model for resonators of various widths and lengths. Note that low aspect-ratio (w/L) devices exhibit the largest error.
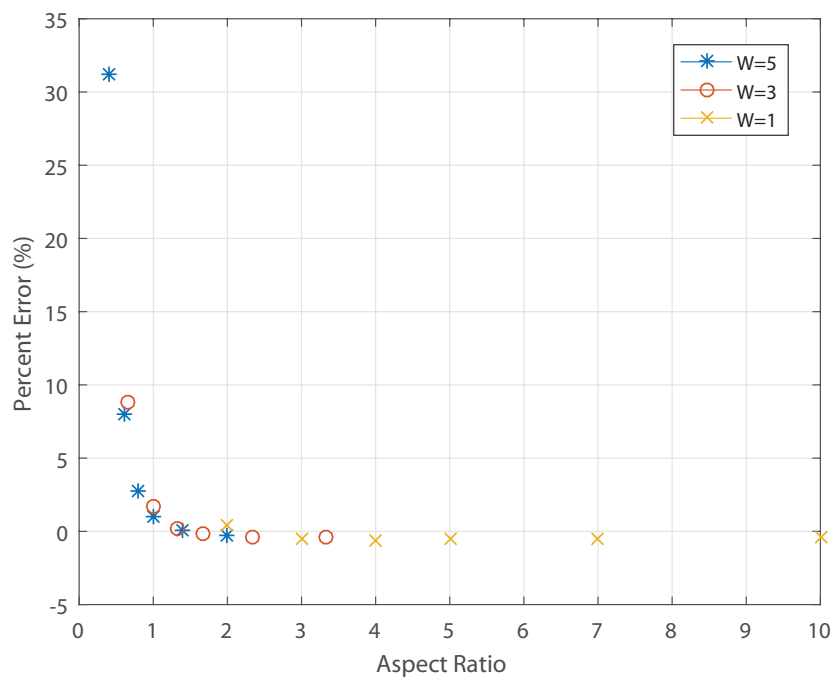
Figure 2.10: Percent difference (error) between FEM-calculated resonant frequencies and those predicted by our model for resonators of various aspect ratio (w/L). Resonators with aspect ratio > 1 are within $\pm 1\%$ of our model.

only of the crossbar, which is clamped at two points (the equivalent of cantilevers of zero length which, themselves, are clamped). Such a beam would behave closer to a doubly-clamped beam than to a singly-clamped cantilever – the middle of the crossbar would experience the greatest deflection, and the edges would remain more-or-less stationary; *i.e.* the crossbar deflection would have a strong z dependence, in stark contrast with our earlier assumptions.

In reality, low aspect-ratio cantilevers are half-way between these two extremes, but the error can be attributed to this z dependence of deflection that becomes more significant as aspect ratio decreases. Figure. 2.11 shows the fundamental mode-shape calculated for a short ($L = 2~\mu$m) and wide ($w = 5~\mu$m) U-cantilever resonator via FEM, along with its strong z dependence.

Ultimately, though, we wish to design our resonators to have an aspect ratio > 1, as the corresponding uniform deflection of the U structure results in more flux cutting, and thereby creates a larger, more measurable response. As such, our model is sufficient for directing future design efforts involving U-cantilever resonant sensors.

Effective Spring Constant for the Multi-Span Model

We may also apply the multi-span modelling technique to obtain a more accurate model for the effective spring constant of the U-cantilever beam, as well as for the effective mass. To do so, we consider, once again, the half-cantilever of Figure. 2.7. We assume a constant y-directed force F is incident at the right-end of the second span ($x' = 0$). Solving the static beam equation (eqn. (2.12)) with the appropriate boundary conditions yields the deflection at the end of the beam ($w(x')$ at $x' = 0$). Taking the ratio of the deflection and the applied force F yields the spring constant of the half-cantilever, which is determined to be

$$
\begin{aligned}
k = 3EI^{(1)}I^{(2)}/(I^{(1)}L_1^3 - I^{(1)}L^3 + 2I^{(2)}L_1^3 - 3I^{(1)}LL_1^2 \\
+ 3I^{(1)}L^2L_1 - 6I^{(2)}LL_1^2 + 3I^{(2)}L^2L_1)
\end{aligned}
\tag{2.56}
$$
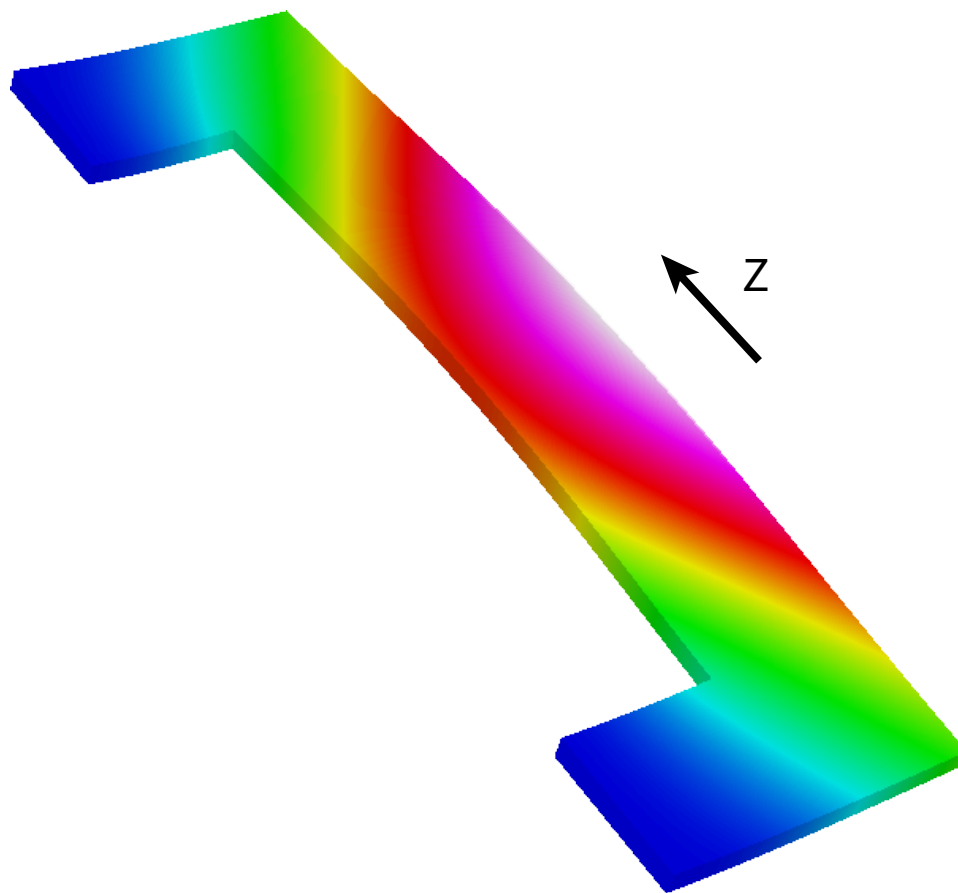
Figure 2.11: The assumption that vertical ($y-$ direction) deflection is independent of z breaks down as aspect ratio shrinks. The fundamental mode-shape for this short cantilever, with a width of 5 μm and a length of 2 μm exhibits a strong dependence on z. This z dependence leads to an error in the calculated resonant frequency.

in which $L = L_1 + L_2$.

The effective spring constant for the full cantilever is then $k_{\text{eff}} = 2k$, and the effective mass is $m_{\text{eff}} = k_{\text{eff}}/\omega_0^2$, where ω_0 is determined using the technique of the previous section.

Extensions of the Multi-Span Model

The enhanced model for the U-cantilever is trivially (if, perhaps, laboriously) able to be extended to modelling the effect of undercut on the resonant frequency of the cantilever. The undercut section of the anchor pad on the left of the cantilever may, itself, be treated as a segment of the multi-span beam, being clamped on one end, and attached to the arm of the cantilever on the other. This segment is attached to the cantilever arm using the same sort of boundary conditions as were present at the interface between spans in the above model for the U-cantilever (see Figure. 2.7). Evaluation of all of the boundary conditions (there are quite a few) yields a matrix equation of the same form as eqn. (2.47). Assigning $k^{(1)}$, $k^{(2)}$ and $k^{(3)}$ to the three spans, the condition $\det \mathbf{A} = f(k^{(1)}, k^{(2)}, k^{(3)}) = 0$ is enforced to ensure a non-trivial solution. Requiring all segments to resonate at the same angular frequency ω_0 fixes the ratios $k_{r1} = k^{(2)}/k^{(1)}$ and $k_{r2} = k^{(3)}/k^{(1)}$, reducing the calculation to a one-dimensional root finding problem; *i.e.*, finding k such that $g(k) = f(k, k \cdot k_{r1}, k \cdot k_{r2}) = 0$. Once k is determined, ω_0 follows from $\omega_0 = k^2 \sqrt{\frac{EI^{(1)}}{\rho \Omega^{(1)}}}$.

The multi-span model may also be applied to the analysis of beams partially covered with a thin film. For instance, consider the cantilever beam of Figure. 2.12, in which a thin film coats a singly-clamped cantilever along a span of length L_{f} from the clamping point. We label the span that includes the film as span 1, and the uncoated span as span 2. The film will modify the effective density $\rho^{(1)}$, cross-sectional area $\Omega^{(1)}$, and moment of inertia $I^{(1)}$ of the beam along the first span, depending on the film thickness and material properties. The techniques of the above section allow the determination of the resonant frequency of such a device.
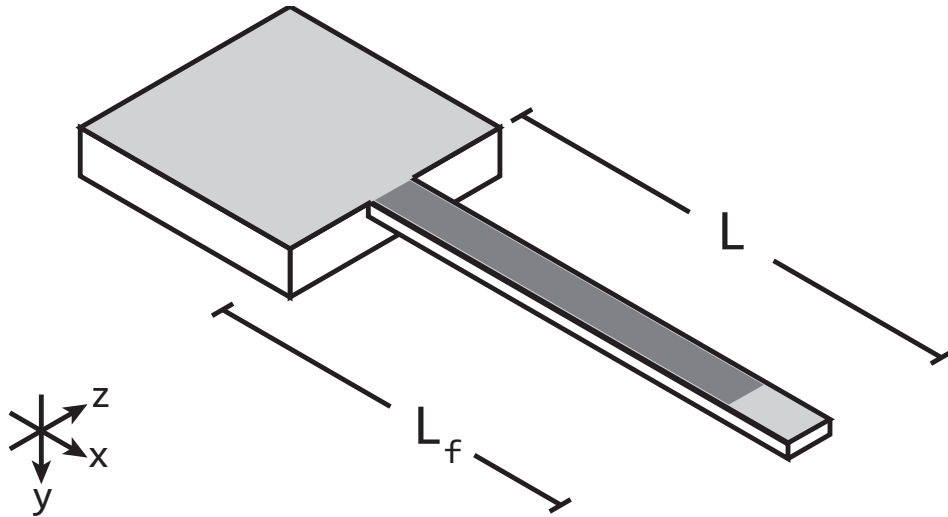
Figure 2.12: A singly-clamped cantilever beam, partially coated with a thin film. L_f denotes the length of the coated span of the beam.

2.4.3   A Note on Torsional Modes

If the U-cantilever is rotated such that the magnetic field is perpendicular to the arms of the "U", equal and opposite time-varying forces will be present along both arms (Figure. 2.13). The result should be a torsional, twisting motion. The motion of both cantilever arms through the magnetic field is expected to produce a large back-EMF, which might simplify detection. In our experiments (chapter 6), we look for evidence of these vibrational modes.

2.5   Modelling the Doubly-Clamped Beam Resonator

The doubly-clamped beam (DCB) resonator is illustrated in Figure. 2.14. The resonator is immersed in a uniform magnetic field with flux density B, oriented perpendicular to the beam. A time-harmonic current I flows through the beam. The flow of charges perpendicular to the field creates a Lorentz-force in the y direction which acts to drive the beam into motion. This force is uniformly distributed along the length of the beam, represented by the distributed load P. Vibration of the beam in the presence of
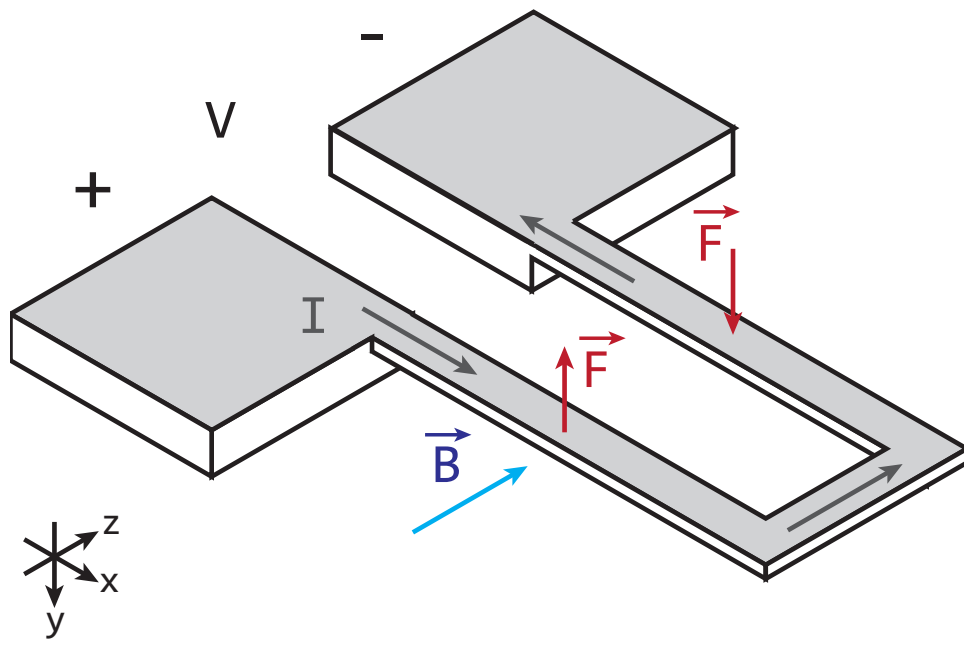
Figure 2.13: "Torsional" excitation of a U-cantilever resonator.

the magnetic field creates a motional EMF which can be used to electronically detect device resonance. Analysis proceeds using a lumped-element approximation as in [17], with more of an eye towards estimating the effect of device parameters on the measured electrical response of the resonator.

From our analysis in section 2.2.1, we have $\omega_0 = k_1^2 \sqrt{\frac{EI}{\rho\Omega}}$ for the doubly-clamped beam, where $k_1 \approx 4.7300/L$ is the first root of eqn. (2.25).

For the sake of simplifying calculations, we will assume that the fundamental mode-shape for the DCB is well-approximated by the static deflection of the beam subject to a (static) distributed load P. Solving the static beam equation (eqn. 2.12) with the appropriate boundary conditions gives the static deflection $\Delta(x)$ as:

$$\Delta(x) = \frac{P}{24EI}x^2(L-x)^2 \tag{2.57}$$

This simplified model is, in fact, quite accurate. Figure. 2.15 plots both the fundamental mode (eqn. (2.26)) and the static deflection profile (eqn. (2.57)) on the same set of axes, each curve normalized to a maximum displacement of 1. The close agreement between these curves justifies the approximation $X_1(x) \approx \Delta(x)$.

In the frequency domain, we have $Y(x, j\omega) = \Delta(x)e^{j\omega t}$. The induced motional EMF along the beam is given by:

$$\begin{aligned}
\epsilon &= \oint \vec{f_{\mathrm{mag}}} \cdot \vec{dl} \\
&= \int_{x=0}^{x=L} -\frac{\partial Y(x,t)}{\partial t} \cdot B dx \\
&= -j\omega B \int_{x=0}^{x=L} \Delta(x) dx \\
&= -j\omega B \frac{PL^5}{720EI}
\end{aligned} \tag{2.58}$$

From basic electromagnetics, we know that P arises due to the Lorentz force, and has a value of $P = I \cdot B$.

From this point, we take the center of the beam $(x = L/2)$ as a point of reference. The deflection here is
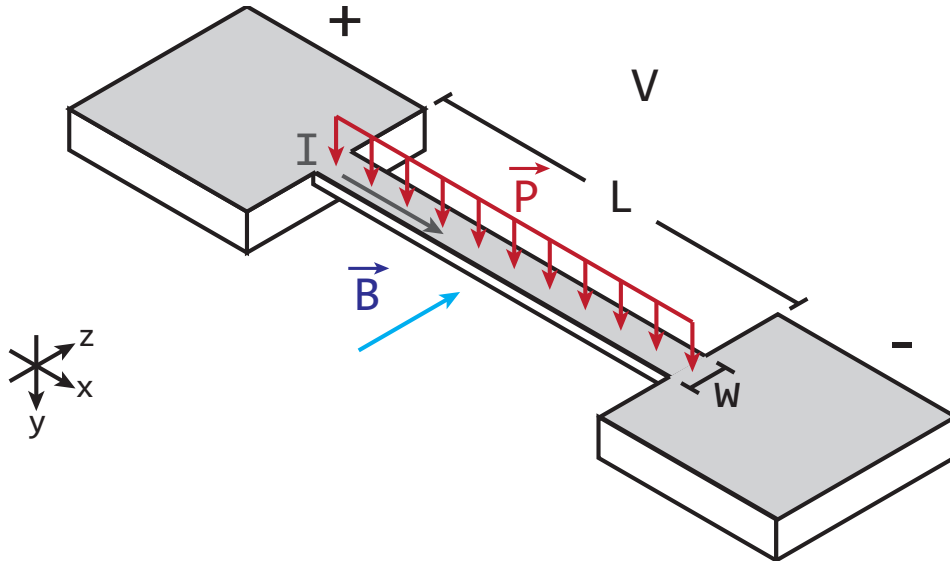
Figure 2.14: DCB resonator with important quantities labelled.

$$\Delta(L/2) = \Delta_{\text{max}} = \frac{PL^4}{384EI} \qquad (2.59)$$

As we are assuming linearity, we may assign a constant of proportionality k between the total applied force $F = P \cdot L = ILB$ and the deflection of the center of the beam Δ_{max}:

$$F = ILB = k\Delta_{\text{max}}$$
$$\Rightarrow k = \frac{384EI}{L^3} \qquad (2.60)$$

This k is the effective spring constant for the doubly-clamped beam. Treating the system as a 1DOF SHO, we have the relation

$$m = \frac{k}{\omega_0^2} \qquad (2.61)$$

in which m is the "equivalent mass" of the resonator; *i.e.* the quantity that relates driving force and vibration amplitude. Letting $C = k_1 L \approx 4.7300408$, we obtain:
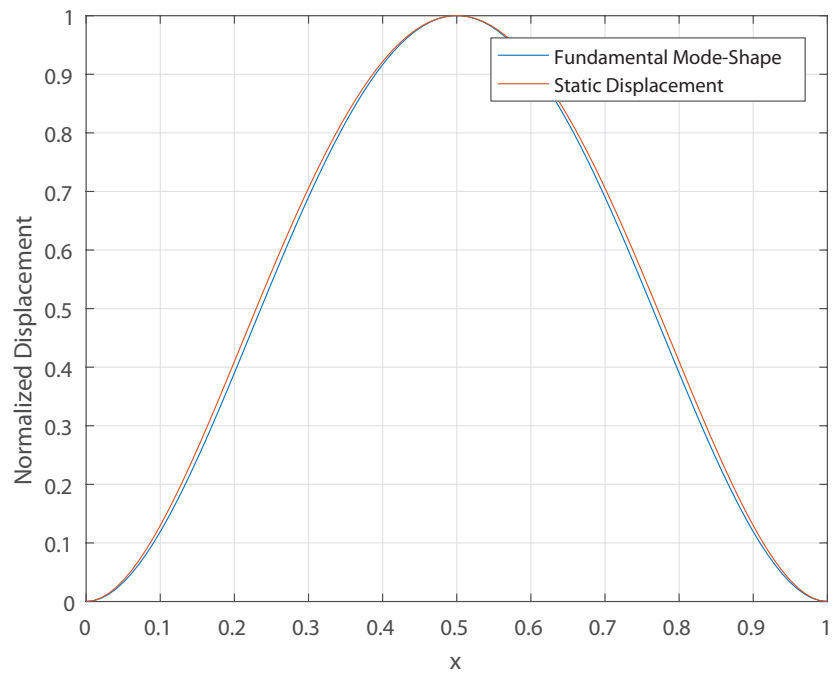
Figure 2.15: Mode-shape function $X_1(x)$ from eqn. (2.26) plotted alongside the static deflection profile $\Delta(x)$ from eqn. (2.57). Each curve is normalized to take on a maximum value of 1. The close agreement between these curves justifies the approximation $X_1(x) \approx \Delta(x)$ made in this section.

$$m = \frac{384\rho\Omega L}{C^4} \tag{2.62}$$

From the theory of the 1DOF SHO, we have the following frequency-domain relation:

$$
\begin{aligned}
\Delta_{\max}(j\omega) &= \frac{F(j\omega)}{m} \frac{1}{\omega_0^2 - \omega^2 + j\frac{\omega_0\omega}{Q}} \\
&= \frac{ILB}{m} \frac{1}{\omega_0^2 - \omega^2 + j\frac{\omega_0\omega}{Q}}
\end{aligned}
\tag{2.63}
$$

Re-stating ϵ from eqn. (2.58) in terms of Δ_{max}, we have:

$$\epsilon = -j\omega \cdot \frac{8BL}{15}\Delta_{\max} \tag{2.64}$$

The net voltage $V(j\omega)$ developed across the terminals of the resonator is

$$
\begin{aligned}
V(j\omega) &= IR + \epsilon(j\omega) \\
&= IR - j\omega \cdot \frac{8BL}{15}\Delta_{\max}(j\omega) \\
&= IR - j\omega \cdot I \cdot \frac{8B^2L^2}{15m} \frac{1}{\omega_0^2 - \omega^2 + j\frac{\omega_0\omega}{Q}}
\end{aligned}
\tag{2.65}
$$

The frequency-dependent electrical impedance of the resonator $Z(j\omega)$ is then:

$$
\begin{aligned}
Z(j\omega) &= \frac{V(j\omega)}{I(k\omega)} \\
&= R - j\omega \cdot \frac{8B^2L^2}{15m} \frac{1}{\omega_0^2 - \omega^2 + j\frac{\omega_0\omega}{Q}}
\end{aligned}
\tag{2.66}
$$

At resonance, the impedance of the device will be real, and attains its peak deviation from the DC resistance R. Setting $\omega = \omega_0$, we obtain:

$$Z_{\text{resonance}} = R - Q\frac{8B^2L^2}{15m\omega_0} \tag{2.67}$$

Substituting for m and ω_0, we obtain the change in impedance at reso-

nance, $\Delta Z_{\text{resonance}} = Z_{\text{resonance}} - R$:

$$\Delta Z_{\text{resonance}} = -Q \frac{C^2 B^2 L^3}{720\sqrt{EI\rho\Omega}} \qquad (2.68)$$

The magnitude of the response is a strong function of both B and L, with the latter being extremely significant – all else held equal, doubling the length of a DCB resonator is expected to increase the response by a factor of 8! Like the U-cantilever resonator (eqn. 2.42), increasing the magnetic flux density B greatly increases the response.

To get a handle on the electronic behavior of the DCB resonator, let us calculate R and $\Delta Z_{\text{resonance}}$ for a large device. Take $L = 10~\mu$m, $w = 1$ μm, $E = 165$ GPa (the Young's modulus of silicon), a density of $\rho = 2330$ kg/m^3, and a beam thickness of $t = 145$ nm. For this resonator, $\Omega = w \cdot t$ and $I = w \cdot t^3/12$. Furthermore, assume that the magnetic field strength is 1 T and that $Q = 1000$. Substituting, we obtain:

$$\Delta Z_{\text{resonance}} = -261\text{m}\Omega$$

For comparison, we estimate R, assuming that the DCB is metallized with a thin film of aluminum with a thickness of 20 nm. Assuming the aluminum film has the same resistivity as the bulk material $\rho = 2.7 \times 10^{-8}$ Ω·m for simplicity, we obtain a sheet resistance of $R_s = \rho/t = 1.35~\Omega$/square. The cantilever measures 10 squares from end to end, meaning that R is roughly $R = 10 \times R_s = 13.5~\Omega$, giving:

$$\frac{\Delta Z}{Z} = -1.93\%$$

This is roughly in line with the figure calculated for the 10 μm long U-cantilever resonator in the previous section, suggesting that the change in impedance obtained from our DCB resonators will be about the same order of magnitude as that of our U-cantilever resonators. Shrinking the device length to $L = 5~\mu$m gives an impedance change of only -0.48% at resonance. Clearly, shorter DCB resonators will be more difficult to measure electronically than longer ones.

2.5.1 Effect of Residual Stress on DCB

The above model for the DCB resonator is qualitatively useful, but not quantitatively so. In particular, the effective spring constant k and the resonant frequency ω_0 are functions of the residual stress in the DCB structure. This stress is inevitably introduced as a result of the manufacturing process, and may be due to stresses already present in the substrate, stresses introduced by deposited films, or thermal mismatch between materials.

The treatment of the DCB subject to residual stress depends on whether the stress is *tensile* or *compressive*. A foundational study of the effect of residual compressive stress on beams can be found in [41], while a study of the effect of tensile stress is presented in [42]. In short, tensile stress tends to increase the effective stiffness of the DCB, increasing the resonant frequency and the effective spring constant k. Compressive stress has the opposite effect, with k and ω_0 decreasing as compressive stress increases.

At a critical value of compressive stress, the effective spring constant goes to zero, and the beam buckles. This value of stress, called the *Euler buckling limit*, is given by the following equation: [37]

$$\sigma_{\text{Euler}} = -\frac{\pi^2}{3} \frac{EH^2}{L^2} \tag{2.69}$$

Because σ_{Euler} goes as $1/L^2$, buckling is a common failure mode for longer beams.

Bokaian [41] gives an approximate formula for the natural frequency ω_0 of a beam under *compressive* stress as:

$$\omega_0 = \omega_{0,\text{unstressed}} \sqrt{1 - \frac{\sigma}{\sigma_{\text{Euler}}}} \tag{2.70}$$

in which $\sigma_{0,\text{unstressed}} = k_1^2 \sqrt{\frac{EI}{\rho\Omega}}$ as we calculated before, and σ_{Euler} is the critical buckling stress of the beam.

Similarly, [42] gives the natural frequency of a doubly clamped beam under *tension* as:

$$\omega_0 = \omega_{0,\text{unstressed}} \sqrt{1 + \gamma \frac{\sigma}{\sigma_{\text{Euler}}}} \qquad (2.71)$$

where $\gamma = 0.97$ for the doubly-clamped beam. These formulas may be used to estimate σ from a set of measurements of DCB resonators from a single fabrication run by means of curve fitting.

2.6 Thin-Film Loadings and Effects on Beam Stiffness

The presence of one or more thin film layers affects both the mass and the stiffness of a resonator, which will modify the resonant frequency of the device. In order to reliably apply our models to real-world magnetomotive resonators, we must take these effects into account.

As a first approximation, we neglect the effect of the non-zero modulus of elasticity of the thin film coating, and consider it purely as a mass-loading. This approximation, used in [12] and based off of the technique presented in [43] should hold well for thin films with small E (such as GLAD films), as well as films with thicknesses that are very small compared with the thickness of the resonating structure. The approximation is as follows: we notice that the factor $\rho\Omega$ may be alternatively expressed as a mass per unit length λ. We substitute λ' for λ, where λ' is given by

$$\lambda' = \rho_{\text{film}}\Omega_{\text{film}} + \rho_{\text{beam}}\Omega_{\text{beam}} \qquad (2.72)$$

and $\Omega_{\text{film}}, \Omega_{\text{beam}}$ are the cross-sectional areas of the film and the beam, respectively. This substitution completes the model.

For a more accurate model for the effect of thin-film coatings on the resonant frequency, we use the *transformed section method* [35] to transform the different thin-film coatings into equivalent cross-sections of the beam material. This method transforms a difference in E between dissimilar materials into an equivalent difference in I for each layer. This transformation is done by multiplying the width of the layer by a factor $n = E_{\text{layer}}/E_{\text{beam}}$. The

46

total area moment of inertia I' for the transformed structure is then determined using the parallel axis theorem. Substitution of I' and λ' completes the model.

2.7 Conclusion

In this section, we began by reviewing the basic mathematical tools for modeling the vibration of continuous beams. We then applied those tools, alongside basic electrodynamics, to estimate the shift in electrical impedance of magnetomotive U-cantilevers and doubly-clamped beams at resonance. These impedance shifts are expected to be very small, especially in the case of narrow U-cantilever resonators. Measuring these small impedance shifts is the subject of chapter 5.

In the course of analyzing the expected behavior of our devices, we derived a more accurate model for the U-cantilever resonator based on a multi-span approximation, which accurately predicts the resonant frequency of the U-shaped structure for aspect ratios > 1. This model will be invaluable in the future, when evaluating the operational performance of fabricated resonators. Furthermore, we discussed the effect of residual stresses on the DCB resonator, which have a profound effect on the resonant frequency of those devices.

Finally, we discussed the impact of the thin-film metallization layers on both mass-loading and beam stiffness. Simple substitutions allow the models derived in this section to be applied to beams laminated with arbitrary stacks of thin film materials. These models will be invaluable in analysis of our results, and for motivating device design and optimization in the future.

Chapter 3

Fabrication and Characterization

One of the major goals of this project was to develop a process flow for fabrication of magnetomotive MEMS resonators that are amenable to functionalization by GLAD films. The requirement of simultaneous control over feature sizes on the scale of 10s or 100s of nanometres (the size scale of our resonators) as well as features on the order of millimetres (the size scale of our electronic instrumentation) necessitates the use of a combination of patterning technologies. In this work, we combine the high resolution of electron-beam lithography (EBL) with more conventional photolithography to bridge six orders of magnitude of feature size on our device chip. The EBL process flow borrows heavily from the work of Westwood *et al.* [11,12]

Our process flow performs electron beam lithography first, patterning our resonators into a layer of electron beam resist. A plasma etch transfers this pattern into the device layer of our chip (Figure. 3.1a). A second round of patterning using contact photolithography defines the wires and contact pads that carry electrical signals to and from our resonators (Figure. 3.1b). Once both of these patterns have been transferred, the devices are released using a buffered-oxide etch, dried, and coated with a conductive metal layer using an electron-beam evaporation process, creating metallized magnetomotive resonators that are ready for functionalization with GLAD.
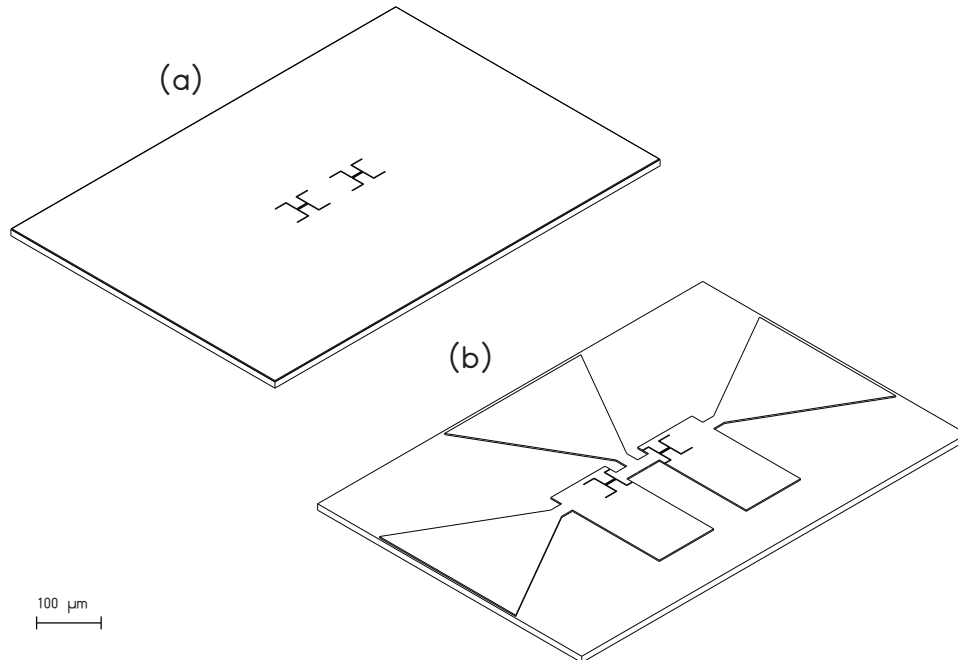
Figure 3.1: Illustration of how the devices are built up from the overlap of (a) electron-beam lithography and (b) photolithography patterns.

3.1 Fabrication Process Flow

Fabrication begins with the substrate; in our case, a SOITECH silicon-on-insulator RF-MEMS wafer. Manufactured using SOITECH's proprietary *SmartCut* technology [44], the substrate consists of a silicon handle layer, upon which a 1 μm buried oxide (BOX) layer and a 145 nm monocrystalline Si device layer are bonded. (See Step 1 in Figure. 3.2.) The silicon device layer is undoped (intrinsic), and exhibits an extremely high electrical resistance, on the order of 1 MΩ·cm. Over the course of fabrication, the Si device layer is patterned to create the devices and electrical contacts. The BOX layer is then isotropically etched, mechanically releasing the resonators from the wafer. Subsequent metallization renders the devices electrically conductive, enabling magnetomotive actuation and detection.

Before carrying out fabrication, the wafer was diced into 1 cm×1 cm square chips. Working with chips of uniform size aids reproducibility in fabrication as well as eases the mechanical design of instrumentation. The wafer was cleaved into quarters, and a quarter wafer was diced using a DiscoDAD precision silicon dicing saw. The individual diced chips were

1. Piranha Cleaned SOI Chip

145nm — Device Layer

1μm — Buried Oxide Layer (BOX)

700μm — Handle Layer
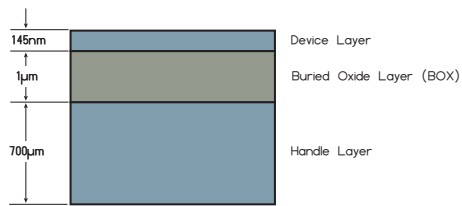
2. Spin-on 1:1 ZEP520A : Anisole
Bake at 170 °C for 10 min

140nm

ZEP520A
Electron Beam Resist
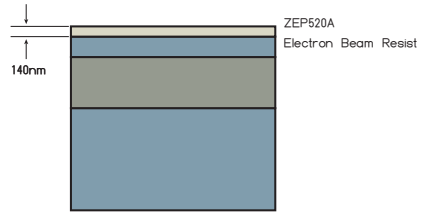
3. Electron Beam Write using Raith 150-two

Exposed Resist

Electron Beam
10 kV, 10 μm Aperture
Dose: 42 μC/cm^2
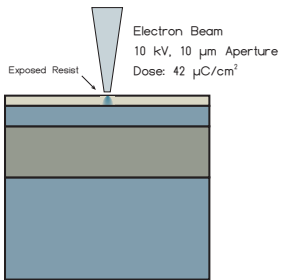
4. Development with ZED N50 Developer Followed by IPA
ZED N50: 40 s, IPA: 20 s

Feature Width
100nm-500nm
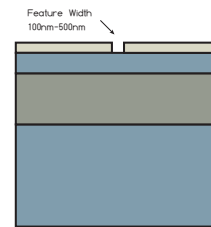
5. Anisotropic Silicon Etch using Oxford Estrelas Standard Unswitched Recipe, 50 s

C_4F_8 / SF_6 Process Gasses
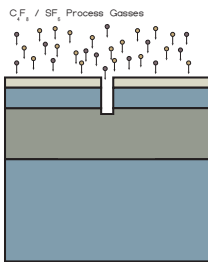
6. Resist Strip and Clean Using Piranha Solution
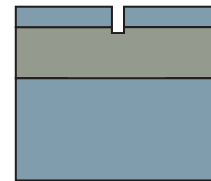
7. Spin-on 2:1 HPR504 : Ethyl Lactate Soft-Bake at 115 °C for 90 seconds

375nm

HPR504
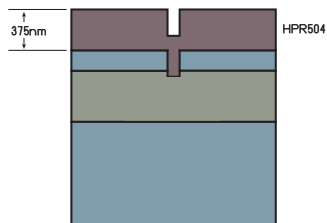
8. Expose resist to UV light through photomask using contact photolithography

Ultraviolet Light

Photomask
Mask Chrome
Exposed Resist
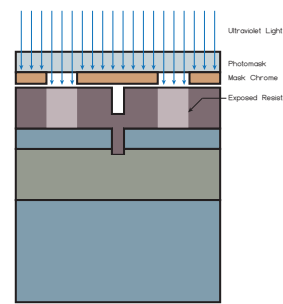
9. Develop photoresist using 354 developer solution for 20 s

Feature Width >2μm
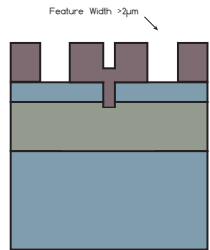
10. Anisotropic Silicon Etch using Oxford Estrelas Standard Unswitched Recipe, 50 s

C_4F_8 / SF_6 Process Gasses
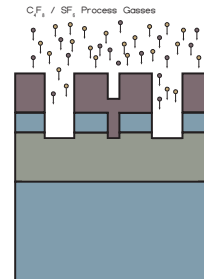
11. Strip resist using acetone. Remove etch residues using EKC265 residue remover at 65 °C for 15 min, followed by IPA rinse and Piranha clean.
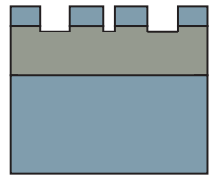
12. Buffered-Oxide Etch to release devices, followed by Critical Point Dry to remove solvents while preventing stictioning.
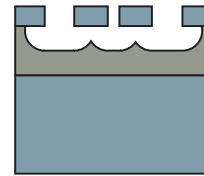
13. Metallization of devices by Physical Vapour Deposition Deposition of 5 nm of Ti, followed by 30 nm of Al

35nm
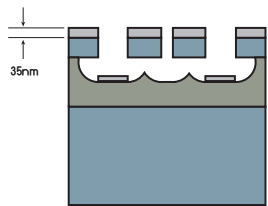
14. Deposition of SiO2 GLAD film for high-surface-area enhancement.

Vertical Posts

300nm
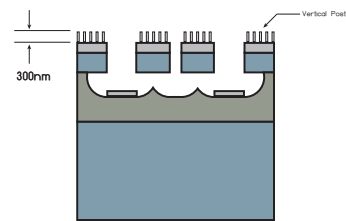
Figure 3.2: Illustrated fabrication process, starting from a piranha cleaned 1 cm×1 cm SOI chip. Details about the individual process steps follow in the text below.

then separated and used as substrates for the remainder of the fabrication process.

The first step of fabrication is to clean any residual dust or debris off of the chip surface. Any dust particles on the chip will disrupt the resist spinning process, leading to defects. For cleaning, we used the standard nanoFAB piranha cleaning process, in which the chips are immersed in freshly mixed piranha bath consisting of a 3:1 mixture of H_2SO_4:H_2O_2 for 15 min. The exothermic nature of the mixing process causes the bath to self-heat as high as 120 °C, accelerating the cleaning process. Piranha solution aggressively attacks any organic contaminants on the chip, leaving a pristine surface for subsequent resist spinning and patterning. Once the 15 minutes has elapsed, the substrates are removed from the piranha bath, rinsed thoroughly with deionized (DI) water, and dried with a nitrogen gun.

After piranha cleaning, we proceed with EBL. The first step of the e-beam lithography process is to coat the substrate with a uniform layer of a suitable resist. For the e-beam resist, we have chosen *Zeon Corporation*'s ZEP520A for its high resolution and sensitivity, along with resistance to subsequent dry-etch processing. [45] To conserve the expensive resist, we dilute the resist with an equal volume of anisole. Important to note is that the diluted resist forms a thinner layer on the chip, which must be accounted for when optimizing the electron beam exposure.

The chip is centered on a vacuum chuck in a Brewer resist spinner, and enough resist to fully cover the chip is dispensed using a micropipette. The chip is then spun at 500 RPM for 5 s to spread the resist, and then spun at 5000 RPM for 40 s to create a uniform thin coating. Typical measured resist thickness is approximately 140 nm when these parameters are used.

The chip is then removed from the resist spinner, and clipped upside-down in a plastic clamp. Supporting the chip in the clamp, the backside of the chip is lightly scrubbed using a cleanroom swab and acetone to remove any resist that may have migrated underneath the chip. This step is essential as any resist underneath the chip would prevent the chip from laying flat in the e-beam patterning tool, compromising the focus of the electron beam as it scans across the chip. The chip is then baked for 10 min at 170 °C on a

Brewer hotplate to drive off any remaining resist solvent. The resist-coated chip is shown in Figure. 3.3.

The next step of the process is to expose the e-beam resist. We used the Raith 150-TWO EBL tool in the nanoFAB to perform the e-beam write, using a 10 μm aperture and a 10 kV accelerating voltage to produce a tight beam capable of high resolution writing. Our write pattern was generated using the excellent Raith GDSII MATLAB toolbox. [46] Apart from the configuration of the electron beam, one key parameter for an electron beam write is the *dose*, or the amount of charge deposited per unit area by the beam in order to expose the resist. For our process, we found a dose of 42 μC/cm^2 sufficient to fully expose the resist without producing noticeable artifacts.

After writing, the resist is developed in *Zeon Corporation* ZED-N50 developer – comprised of n-amyl acetate, for 40 s. This developer preferentially attacks the resist that has been exposed to the electron beam in the Raith system, transferring the e-beam write pattern to the resist film. The chips are then immediately transfered to IPA for 20 s to halt the development. After IPA immersion, the chips are rinsed with DI water and dried with an N$_2$ gun. The chips are immediately inspected with an optical microscope in the cleanroom to verify that the resist write and development were successful.

After the resist has been patterned, the next step in fabrication is to transfer the resist pattern to the Si device layer with an anisotropic etch. For this etch process, we use the Oxford Estrelas Deep-Silicon Etcher in the nanoFAB – an inductively coupled plasma reactive ion etcher (ICPRIE). This machine, pictured in Figure. 3.4, implements a number of state-of-the-art anisotropic etching techniques, including Bosch and cryogenic etch processes, which are appropriate for deep etches into silicon (potentially hundreds of microns in depth). As our Si device layer is itself extremely thin (145 nm), we do not require as extreme a level of anisotropy, and can instead run a (much simpler) unswitched etch process. In the unswitched mode, the chips are exposed to a plasma consisting of C$_4$F$_8$ and SF$_6$ species. Species due to SF$_6$ in the plasma bombard the chips. Due to the biasing of the substrate in the ICPRIE system, these ions are mostly incident normal
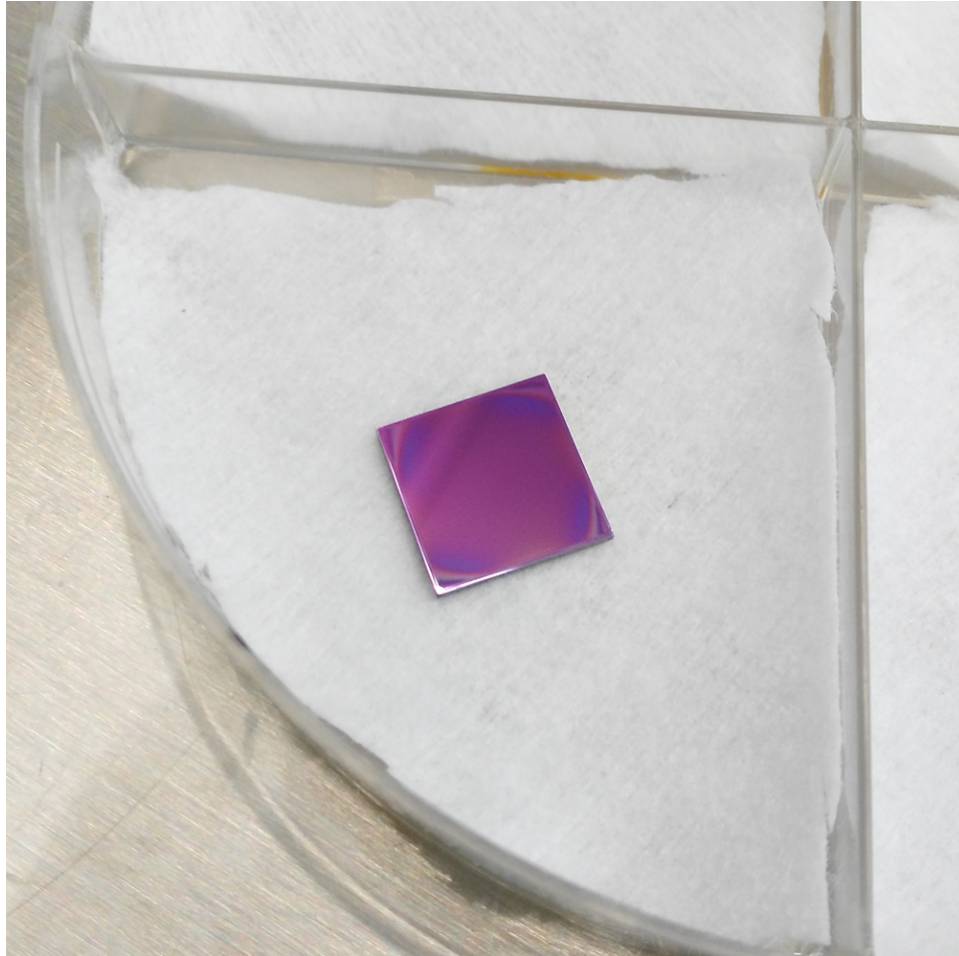
Figure 3.3: Photograph of a 1 cm×1 cm SOI chip after coating with ZEP520A electron beam resist. The color gradient indicates good uniformity, with only mild thickening of the resist near the corners of the chip.

to the chip surface, generating an anisotropic etch. Species due to C_4F_8 in the plasma deposit a Teflon-like polymer on the chip that further inhibits sidewall etching, enhancing anisotropy. The SF_6 etch is highly selective against SiO_2, allowing the BOX layer to double as an etch-stop for this process. Selectivity against ZEP520A prevents the resist layer from being significantly degraded over the course of the etch, leading to correct pattern transfer.

As the etching tool only accepts standard-size (100 mm or 150 mm diameter) wafers, our 1 cm×1 cm chips must be bonded to a carrier before the etch can take place. Rather significantly, adequate and consistent thermal contact is required for the etch to proceed correctly – inadequate thermal contact causes the chip to heat and the etch properties to change, potentially creating 'grass' defects and affecting the etch rate. The chips were bonded to an oxidized Si 150 mm carrier wafer using Crystalbond adhesive on a hotplate at 65 °C. Following this step, the etch was carried out for 50 seconds using the standard 'Unswitched' process on the tool. After etching, the chips were then removed from the carrier by re-heating the carrier wafer on the hotplate.

Following etching, the e-beam resist must be stripped. We use piranha solution to simultaneously strip the (organic) resist, any residual polymer from the etching process, as well as clean the chips in preparation for photolithography. The cleaning process used here is identical to that used prior to EBL.

Following cleaning, we spin-coat the chips with photoresist. This process is complicated by the fact that, in order to maximize the number of devices on a chip, we would like to pattern all the way to the edge of the chip. Typical resists for photolithography have a resist thickness on the order of microns. This rather thick layer beads up at the corners of the chip during the spinning process. The resulting lack of uniformity severely limits the patternable area on the chip, severely limiting the utility of photolithography in patterning a small chip.

The solution to this problem is two-fold. First of all, we may increase the spin speed during resist spinning. Increases in spin speed lead to a pre-

Figure 3.4: The Oxford Estrelas Deep Silicon Etcher (DSE). This load-locked system is capable of a wide variety of silicon etching techniques, including Bosch processing, cryogenic etching, and more.

dictable decrease in film thickness, which should lead to a smaller edge-bead. This approach works to an extent; however, the effect of further increasing spin speed diminishes rapidly, leaving us with a thicker resist than we would like. The other approach is to dilute the resist, lowering the viscosity in order to yield a thinner film. This approach requires great care, as the chemical composition of the photoresist has already been carefully optimized by the manufacturer – diverting from the standard formulation can create a host of issues, ranging from nucleation and particulate generation to expedited aging of solution, changes in sensitivity, *etc.* When applied with care, however, dilution is a powerful tool for thinning the resist layer.

For our resist, we chose HPR504 from *OCG Microelectronic Materials.* This commonly available positive photoresist has the thinnest film thickness of the entire HPR500 resist series, making it a good starting point for a diluted resist. We dilute two parts HPR504 solution in one part of ethyl lactate solvent, which is the native solvent of the resist. Dilution of the resist in its own solvent minimizes the chances of degrading the resist due to interaction between different chemical species. The dilution was carried out on a stir-plate, the HPR504 being stirred continuously at 120 RPM while the ethyl lactate solvent was slowly added. This mixing process prevents the formation of an ethyl lactate-to-HPR504 interface which may result in particulate generation. After mixing, the resist was poured into a bottle and stored in a chemical fridge for future use.

The spin-coating process for photolithography closely mirrors the EBL resist spinning process. Each chip is carefully centered on a vacuum chuck in a Solitec resist spinner. Enough diluted resist to cover the chip is dispensed manually using a micropipette, taking care not to introduce any bubbles. The chip is then spun at 500 RPM for 5 s to spread the resist, followed by spinning at 7000 RPM for 40 s to produce an extremely thin resist layer with minimal edge bead. After spinning, the chip is removed from the spinner, and the backside of the chip wiped with a cleanroom swab and acetone to remove any resist that would prevent the chip from laying flat during photolithography. The chip is then baked at 115 °C for 90 s under vacuum in order to drive off the resist solvent. Following the baking process, the

chips are left to rehydrate in the cleanroom atmosphere for at least 15 min. A deficit of water in the resist layer would prevent photobleaching from taking place, preventing proper exposure of the resist.

The resist-coated chip is then transferred to an ABM mask aligner for alignment and exposure. The photomask – cleaned in cold piranha solution for 15 minutes beforehand – is mounted in the mask aligner, and aligned to alignment marks patterned on the chip during the e-beam lithography process. Once alignment is satisfactory, a contact vacuum in the mask aligner brings the mask and chip into mechanical contact. The chip is then exposed to UV light through the photomask. We expose our chips with a total dose of 85 mJ/cm^2. See Figure. 3.5 for an example of a photomask pattern used in fabricating our devices.

After exposure, the chips are removed from the mask aligner and developed in *Microposit* 354 developer solution for 22 seconds, then rinsed with DI water and dried with an N$_2$ gun. The chips are then immediately inspected under an optical microscope in the cleanroom to check for proper development.

Once the photoresist has been successfully patterned, the resist pattern is transferred to the device layer using the Oxford Estrelas DSE using an etch process identical to that used for etching the EBL pattern. The etched chips are pictured in Figure. 3.6. After this etch step, the device layer is fully patterned. All that remains is to release the devices, metallize the device layer, and deposit the high surface area GLAD film. Fabrication proceeds first with a Piranha clean step to strip the photoresist and clean the surface of the chip. This piranha clean is critical as this is the final time that the chips may be wet-processed – any subsequent dust or debris that contaminates the chip will be very difficult to remove. The piranha clean is carried out using the standard 15 min process. The cleaned chips are pictured in Figure. 3.7.

After piranha cleaning, the chips are clipped into plastic clamps, face down, in preparation for immersion in a Buffered-Oxide Etch (BOE) solution. The face-down clipping ensures that any debris introduced by the etch process falls down and away from the chip surface rather than onto it, as
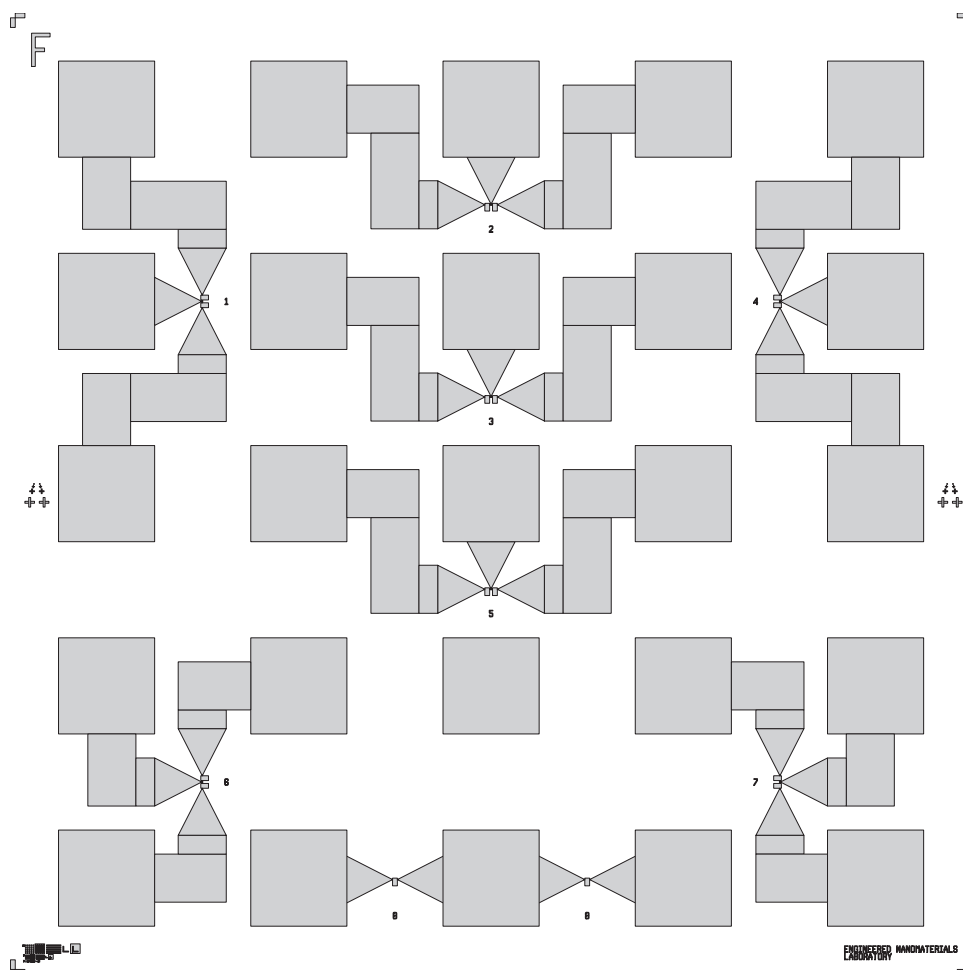
Figure 3.5: Photomask pattern used for U-shaped cantilever resonators. The array of 25 contact pads is clearly visible. Alignment marks on the left and right of the chip allow for precise registration with electron-beam-patterned resonators. Shaded areas correspond to chrome on the mask.
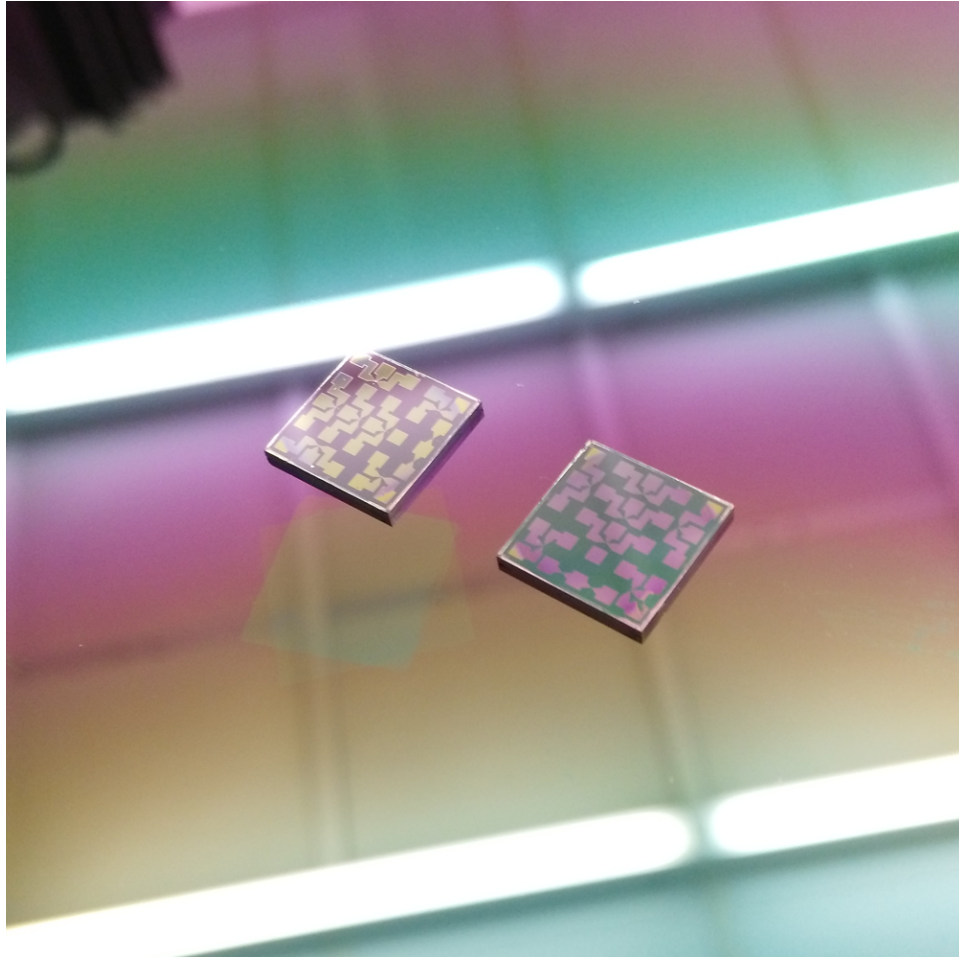
Figure 3.6: Photograph of SOI chips bonded to a carrier wafer for processing with the Oxford Estrelas DSE.
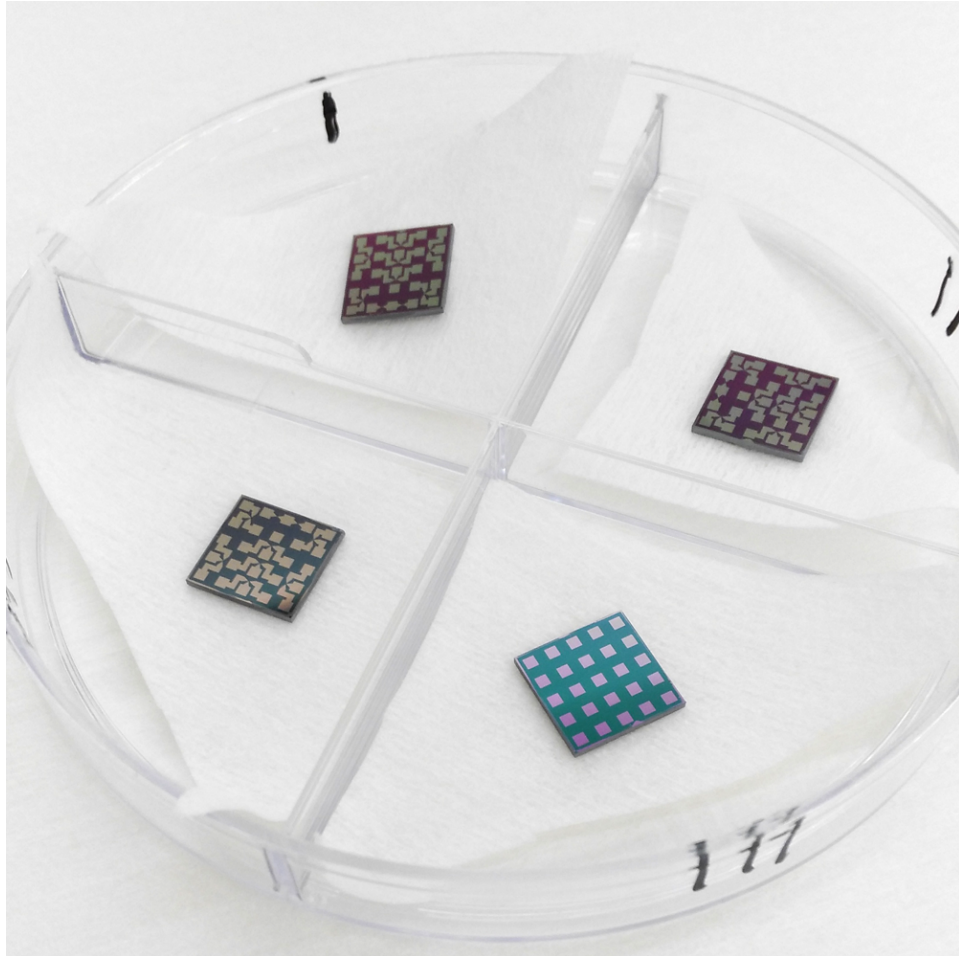
Figure 3.7: Photograph of SOI chips after photolithographic patterning, etching, and piranha cleaning. The use of diluted resist allows repeatable patterning all the way to the chip edges, including in the corners.

well as preventing the surface of the chip from being masked by the teeth of the clamp. BOE isotropically etches the buried oxide layer, undercutting all features that were patterned on the device layer. The length of the BOE etch is chosen long enough to ensure that all resonating structures are fully released from the substrate. As a result, the required length of this etch depends primarily on the width of the resonators on the chip.

Once the BOE etch is complete, the chips are rinsed in three successive DI water baths, before being transfered to an IPA bath for transport to the critical point dryer (CPD). Chip transfer between solutions is carried out as rapidly as possible to prevent evaporation of liquid from the chip surface which may cause stiction of devices. The CPD system is filled with IPA, and then the samples are loaded. The critical point drier removes the IPA from the chip without crossing a liquid-vapour phase boundary, preventing stiction from occurring.

With the devices released and the solvent removed, the chips are ready for metallization. This step is done using an electron-beam evaporation system. A bulk film of Ti a few nanometers in thickness is first evaporated onto the chip. The Ti serves as an adhesion layer, as well as providing resistance to mechanical abrasion. Following the Ti deposition, a bulk film of Al a few 10s of nanometres in thickness is evaporated onto the chips in order to enhance electrical conductivity. Both films are deposited with an incident flux angle α of 45° and with continuous substrate rotation to enhance uniformity.

In this fabrication scheme, the undercut generated by the BOE process is responsible for the ultimate electrical isolation between devices. Because PVD film growth is largely a ballistic process, the overhanging Si device layer physically shadows the undercut BOX layer at the edges of patterned features on the chip, preventing metal deposition along the feature perimeter. The result of this shadowing is complete electrical isolation of the devices. In practice, any dust, defect or debris along the perimeter of a given device can compromise this isolation; as a result, extreme care is necessary during fabrication to keep the devices clean.

At this point, the fabrication of the resonators is essentially complete.

As the devices are fully released and electrically conductive, they may be actuated using the magnetomotive technique, and may be used as a platform for investigation of the application of nanomaterials to gravimetric NEMS sensing. Furthermore, imaging the fabricated devices using scanning electron microscopy (SEM) allows us to check for stress induced bending, buckling, and/or stictioning of our devices. For SEM characterization, we used the excellent Zeiss Sigma Field-Emission SEM in the University of Alberta NanoFab. A metallized U-cantilever resonator is pictured in Figure. 3.8.

To create a nanomaterial-enhanced sensor, all that remains is to deposit the nanomaterial; in our case, a GLAD film. We deposit a vertical-post structure GLAD film of SiO_2 using electron-beam evaporation at a highly oblique α of 80° and a target column height of 300 nm. The SiO_2 GLAD film produces a large surface-area enhancement, with the goal of increasing the sensitivity of our devices to an analyte gas. Important to note is that silica (SiO_2) as a material is very amenable to later chemical functionalization [15, 16], producing a possible road towards specific sensing using this platform.

3.2 Fabrication Challenges

3.2.1 Stiction

Stiction is a concern whenever devices are released using a liquid-phase process. A stictioned device is pictured in Figure. 3.9. In our process flow, stiction is most likely to occur between the beginning of the BOE etch step and the end of the CPD step. During sample transfer, the wet-processed chip is briefly exposed to atmosphere, providing an opportunity for solvent evaporation which may lead to stiction. To mitigate this issue, we take great care to minimize sample exposure to air during transfer from container to container. Sample transfer is done as quickly as possible, while keeping the sample face-down so as to maintain a droplet of solvent on the sample surface. Furthermore, we significantly over-etch the BOX layer during the BOE release step, creating a larger separation between released structures and the remaining oxide on the substrate. This larger separation should
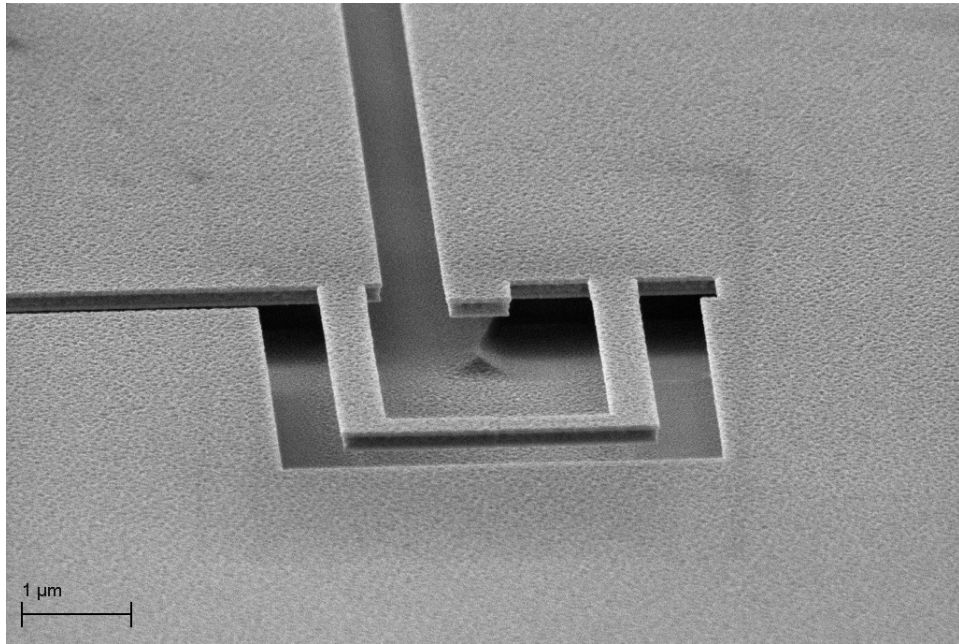
Figure 3.8: Scanning electron micrograph of a metallized U-cantilever resonator, captured using a field-emission SEM. The small pyramid of SiO_2 below the small protrusion in the device layer is evidence of the isotropic character of the BOE undercut process.

reduce the chance of stiction.

Future work will substitute the BOE wet processing step and the subsequent critical point dry with a vapour-phase HF release process. The vapour-phase process is expected to be gentler on the devices, allowing repeatable release of stiction-prone long cantilever resonators. Furthermore, elimination of the wet process release step greatly simplifies the fabrication procedure, resulting in less hand-manipulation of chips during this most critical phase of processing.

3.2.2 Buckling

Buckling is the primary failure mode for the doubly-clamped beam resonators, and occurs when the beam is subject to a compressive stress greater than some critical value σ_{Euler}, which is difficult to predict. The compressive stress is primarily due to the metallization layer, which contracts biaxially as a result of temperature changes during or after deposition. A buckled doubly-clamped beam resonator is pictured below, in figure 3.10.

For a perfect doubly-clamped Euler-Bernoulli beam experiencing first-order buckling, the *Euler buckling limit* is given by the following:

$$\sigma_{\text{Euler}} = -\frac{\pi^2}{3}\frac{EH^2}{L^2} \tag{3.1}$$

Eqn. (3.1) indicates that shorter beams are significantly more resistant to buckling than long beams. This is consistent with our observations – only the longest beams (>5 μm) were observed to buckle. However, even in the absence of buckling, the presence of compressive stress in a doubly-clamped beam is expected to lower the beam's resonant frequency. This property seriously limits the application of doubly-clamped beam resonant sensors when design for a precise operating frequency is required.

3.2.3 Incompatibility of Metallization with BOE

A more traditional process flow might have the metallization process occur *before* the buffered oxide etch release step, rather than after. Pre-release
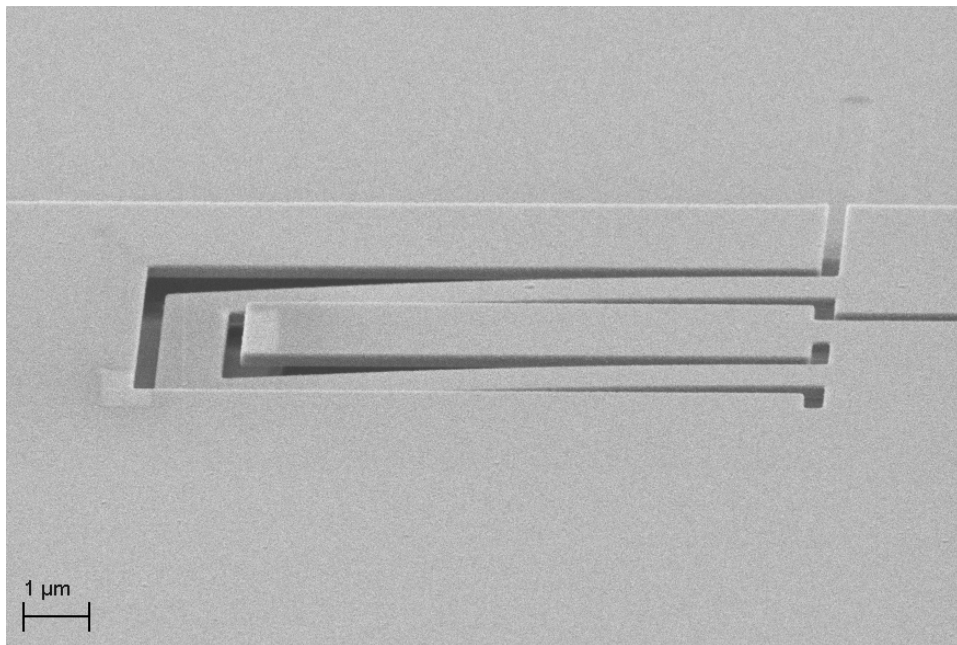
Figure 3.9: Micrograph of a metallized U-cantilever that has stictioned downward, adhering to the substrate. The out-of-plane bending is apparent.
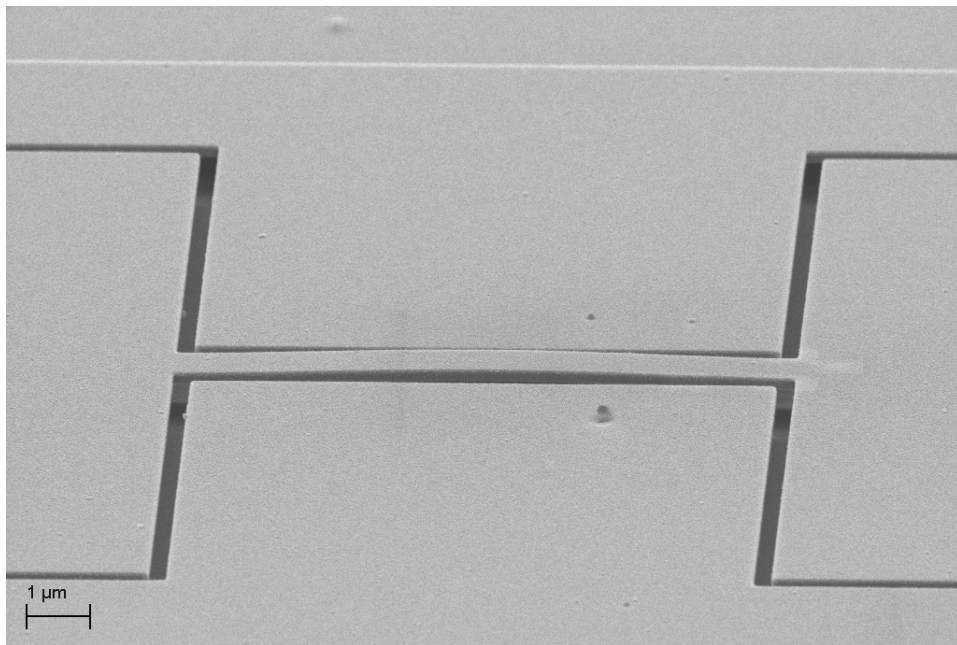
Figure 3.10: Micrograph of a metallized DCB resonator that has buckled upward, due to compressive stress.

metallization would have a number of distinct advantages. First of all, cantilevers and beams would not bend or buckle during the deposition, as they would remain anchored to the substrate, preventing any motion of the structures during deposition from affecting the uniformity of the deposited film. Second, a patterned metal layer could double as an etch mask for the second RIE silicon etch. Metal on the SiO_2 BOX layer could be patterned away, preventing electrical shorts between devices and substantially increasing device reliability and yield.

Unfortunately, during early testing, we noticed that our BOE process readily attacked our aluminum metallization layer. The aluminum seemed to delaminate in large flakes during the BOE treatment, in addition to dissolving. These flakes were observed floating in the BOE solution after treatment of our metallized chips. Subsequent SEM revealed small bits of (presumably Al) debris on the chip, with no bulk metal film present.

At this time, we are not certain as to what is causing the BOE to attack the metallization layer. One potential hypothesis is that the aluminum that we deposit is highly contaminated with carbon due to being deposited via e-beam evaporation with a graphite crucible liner. This carbon-contaminated aluminum might be more susceptible to oxidation, the oxidized Al_2O_3 being attacked by the BOE solution. Alternatively, heating Al and Al_2O_3 in the presence of the graphite crucible might lead to some incorporation of carbon in the melt. [47] Contamination might compromise film adhesion as well. Performing an aluminum deposition with an alternative (non-graphite) crucible liner and comparing the resulting film under BOE treatment with an Al film deposited from a graphite crucible-liner could give further insight into this issue.

3.2.4 Photoresist Stripping and Residue Removal Post-Etch

Early in our work, we noticed a tendency for the photolithographically patterned features (wires and contact pads) to become electrically shorted to the ground plane after metallization. Inspection under SEM revealed the cuprit: long thin strands of material were found littered about the edges

of the photolithographically-defined topography (see Figure. 3.11). These strands of material, after metallization, formed electrical bridges between the contact pads and the ground plane, shorting out our devices.

The fact that these strands of material were concentrated near feature edges suggests that whatever material was responsible for the shorting was introduced during the etch process. Our hypothesis is that the material is a Teflon-like polymer, deposited during the dry etching step. This polymer would be chemically resistant to attack by Piranha solution, preventing its removal during the post-etch cleaning stage of processing.

The solution is to incorporate a post-etch cleaning regimen to target this sidewall polymer and ensure that all resist and etch residue is removed from the chip prior to release. After the dry etch process, we strip the photoresist residue with an acetone spray, followed by an IPA spray and a deionized water rinse. We then submerge the chips in a bath of EKC265 post-etch residue remover, heated to 65 °C., followed by another IPA rinse, DI water rinse, and N_2 dry. Finally, we proceed with piranha cleaning to remove any remaining dust or debris immediately prior to BOE release.

3.3 Conclusion and Future Work

Ultimately, our fabrication process was successful. Many fabricated devices functioned as expected (chapter 6). That said, issues with stiction of large devices, general issues of yield, as well as open questions regarding potential thin-film contamination suggest there is still some work to be done in fine-tuning our fabrication work-flow.

Perhaps the most immediate issue to address is the BOE attacking the Al metallization layer of our devices. The potential culprit – contamination of our Al films with carbon – might also be responsible for mechanical losses in our devices (see section 6.4.2). Fabricating devices using thin-films evaporated from carbon-free crucible liners (tungsten or boron nitride) would address both of these questions at once.

The fact that some devices were observed to buckle or snap suggests that the thin films we are depositing are holding our devices in compressive
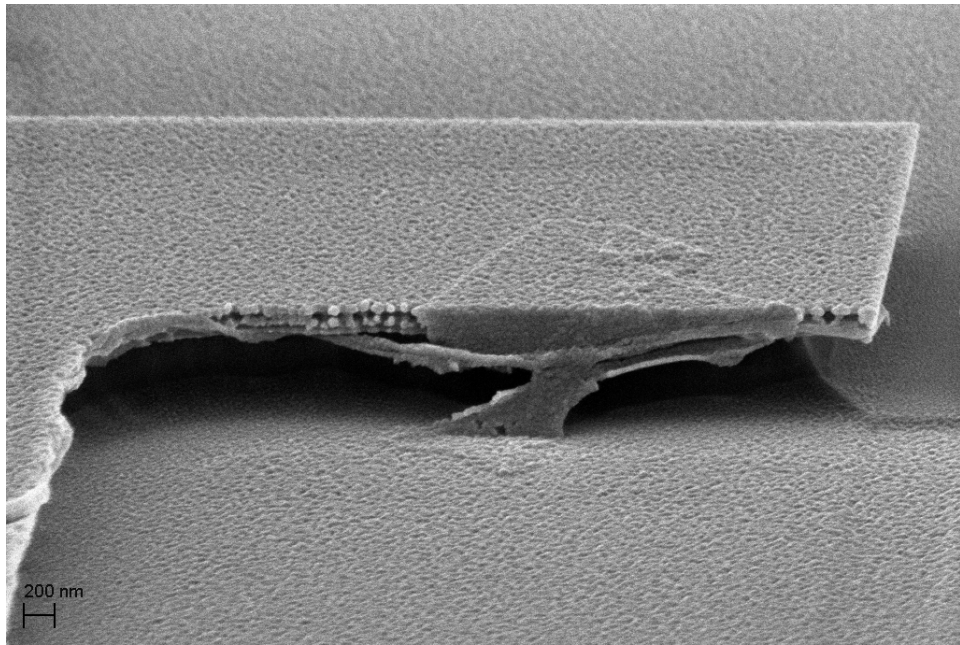
Figure 3.11: Metallized residue responsible for electrical short-circuits on a completed chip.

stress. Use of different thin-film materials for metallization might reduce the severity of this effect.

Finally, a common failure mode in the as-fabricated devices is an electrical short to the metallized ground-plane. In the future, if the issue with the BOE process attacking the Al metallization layer can be resolved, a lift-off patterning procedure could be used to define the contact pads and wires, eliminating the metallized ground plane altogether. This metal layer could double as an etch mask during RIE, simplifying the fabrication process.

Chapter 4

Instrumentation Design – Mechanical

Mechanical design of a low-cost system for magnetomotive actuation and detection of NEMS resonators presents a number of significant challenges. In order to actuate and characterize our devices, we require a test system capable of feeding high-frequency electrical test signals into a controlled environment. As we are using the magnetomotive technique for both actuation and detection, this environment must include some means of generating and sustaining a powerful, uniform magnetic field, along with a means of mechanically securing our devices in the field. It is also necessary to make electrical contact with the contact pads on our chip, and route these signals to electrical cables for later instrumentation. Furthermore, the gas pressure of the environment must be variable between atmosphere and about 1 mTorr. Operation at (near) vacuum eliminates mechanical damping due to the presence of air, allowing us to measure the resonance parameters of our devices independent of air damping.

4.1 Vacuum Design

We designed and built a custom vacuum system to satisfy the design objectives. A large vacuum chamber houses a permanent magnet assembly, which

generates a powerful uniform magnetic field throughout a small cylindrical cavity. This chamber is outfitted with both a roughing port and a high vacuum port. The high vacuum port is connected through a gate valve to a turbomolecular pump, which itself is backed by the roughing pump. A dry nitrogen line is connected to the main chamber through a ball valve, allowing the chamber to be vented at a controllable rate. Nitrogen may also be flowed into the system while pumping in order to vary the system pressure. Together, the nitrogen venting valve, the turbomolecular pump, and the roughing pump provide access to pressures ranging from atmosphere to well under 1 mTorr.

The main chamber is outfitted with two capacitance manometers for pressure monitoring. Together, these two sensors cover an operational pressure range of 1 mTorr to 1000 Torr. Though pressures of <1 mTorr are routinely reached while running the turbopump, these low pressures cannot be measured with the apparatus as it currently stands. Installation of an ion gauge sensor would allow pressures down to 10^{-10} Torr to be measured, far beyond the expected system base pressure.

A pair of RF coaxial feedthroughs on the chamber lid allow RF signals to be conducted into and out of the main chamber. A second multi-pin electrical feedthrough carries power and control signals into the chamber for interfacing with in-chamber electronics.

The main system schematic is presented below, in Figure. 4.1. The following sections of this chapter elaborate on some of the systems present, and the considerations that went into their design.

4.2   Magnetics

For instrumentation and measurement of our sensors, we require a powerful, uniform magnetic field. As the electrical response of our resonators is expected to scale as B^2 (see chapter 2), a more powerful field yields ever increasing gains in output signal strength. All else held equal, a stronger magnetic field allows for measurement of smaller, more sensitive, higher-frequency resonators, increasing the achievable performance of our system.
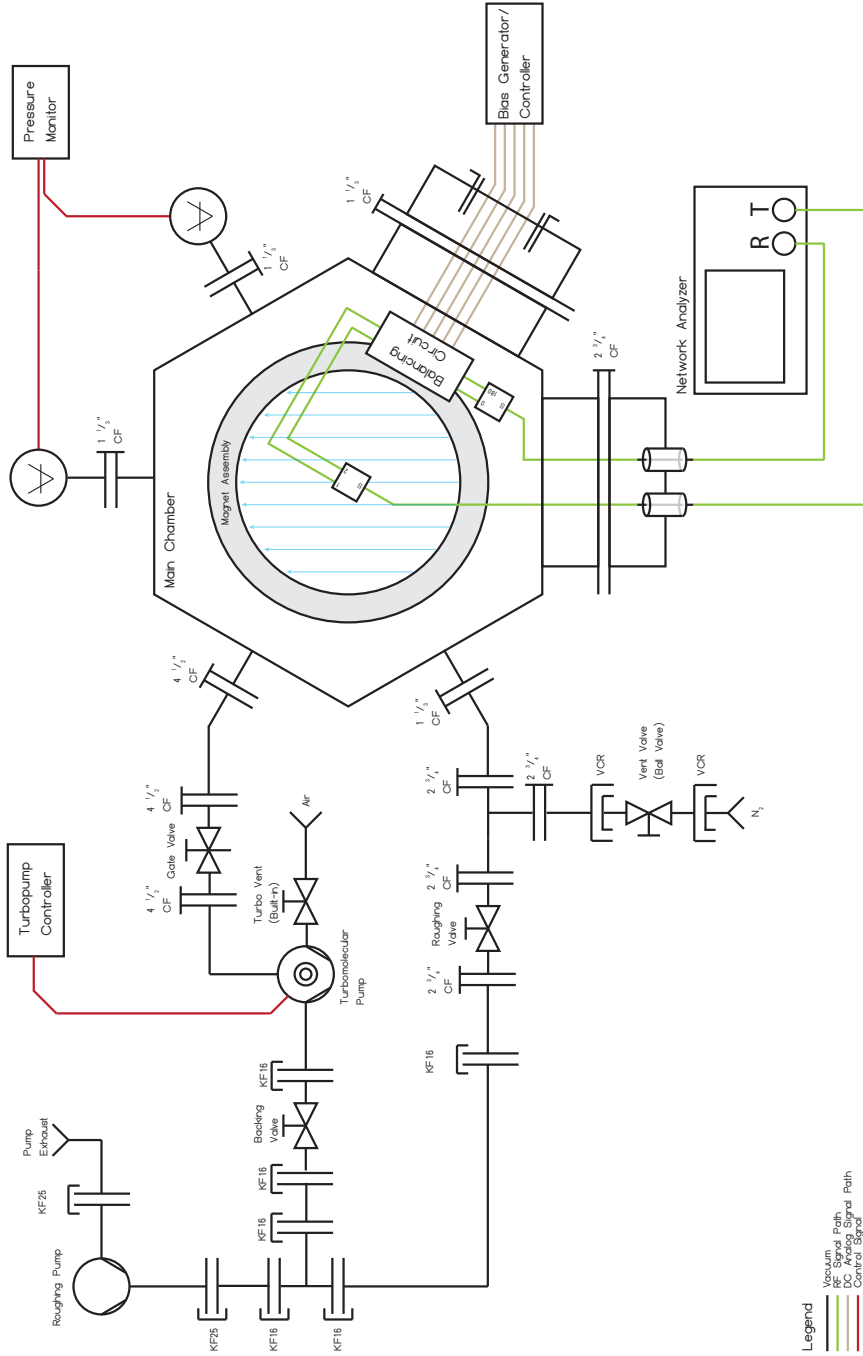
Figure 4.1: Full schematic of the vacuum system, including electrical control signals and the RF signal path. All valves are manually actuated. Details about the design and operation of the electrical instrumentation are found in Chapter 5.

Figure 4.2: Photograph of the complete system, as assembled on a rolling cart. The main chamber lid, outfitted with dual RF feedthroughs, is visible on the right side of the photo. In the center of the photo, the gate valve, turbomolecular pump, and backing valves are visible. The roughing pump is visible in the bottom right of the cart.

Traditionally, the large magnetic flux densities required for this application (on the order of 1 T) have been generated using superconducting magnets. These magnets represent the highest achievable performance for generating static, uniform fields. Early work by Dr. Ekinci and the Roukes group on balanced magnetomotive instrumentation employed a superconducting magnet capable of sustaining an 8 T field, yielding detectable resonances at frequencies as high as 200 MHz without special consideration for fine-tuning the electrical balance of the system. [27] The other advantage of these systems is that the magnetic flux density may be varied, so as to investigate the effect of field strength on device resonance.

The unfortunate reality, however, is that superconducting magnet assemblies are out of reach for many researchers, for reasons of cost. Where superconducting assemblies are prohibitively expensive or unwieldy, permanent magnet assemblies become competitive. Modern rare-earth magnets fabricated from NdFeB materials represent the state of the art in permanent magnets, due to their high remnance and coercivity — in short, they are capable of sustaining a strong magnetic field, while simultaneously resisting demagnetization. Such magnets are attractive for generating powerful, static magnetic fields.

In order to achieve maximum field strength and uniformity, the spatial orientation of the magnets is paramount. For our system, we use a configuration known as a Halbach array to generate a uniform and powerful magnetic field. Eight NdFeB magnets are oriented in a ring structure, with the direction of magnetization making two full rotations around the ring. This orientation of magnets concentrates and collimates the magnetic flux in the interior cavity, while simultaneously canceling the majority of the flux outside the ring. Our Halbach magnet assembly was ordered from *E-Magnets UK*, and generates a uniform 1 Tesla field in a 30 mm diameter and 40 mm deep cavity.

In contrast with superconducting magnet assemblies, permanent magnet assemblies are *always on*, and thus present a significant safety hazard. These powerful magnets can easily crush fingers or even hands if they become pinched between the magnet and a ferromagnetic material. For this reason,

great care was taken in installing the magnet assembly in our system.

As some components of the complete system (notably, the cart which houses the equipment) are ferromagnetic, the magnet was installed in the main chamber prior to complete system assembly. This was done to avoid the possibility of injury from the magnet being attracted to the cart during assembly. To ensure continued safety, we had a retaining bracket fabricated out of aluminum (a non-ferromagnetic material) to secure the magnet in the chamber and prevent the assembly from catastrophically "jumping out" of the system and creating risk of injury. The assembly of the magnet, retaining bracket, and chamber is illustrated in Figure. 4.3. The as-assembled main chamber is shown in Figure. 4.4. With the bracket in place, the main remaining hazard associated with the magnet is having ferromagnetic tools pulled into the cavity. In any case, the researcher must take great care to keep ferromagnetic materials out of the vicinity of the magnet assembly, and warnings are posted to that effect.

It is important to note that NdFeB magnets have a low Curie temperature, rendering them incompatible with high-temperature vacuum bake-out processes. This is likely not a major concern in this application, as the quality of vacuum is not critical – the system need only operate down to about 1 mTorr of pressure, and bakeout is used only when much lower pressures must be reached.

Finally, we note that the main chamber of the system is fabricated from austenitic stainless steel, which is only weakly ferromagnetic, so the effect of the chamber on the field in the cavity of the magnet assembly should be insignificant.

4.3 Test Fixture

We designed and built a mechanical test fixture to both secure our chip in the magnetic field, and to make repeatable, electrical contact with the contact pads on the chip surface. The test fixture is a two-piece assembly. The bottom part of the assembly is constructed from an aluminum cylinder, with a pocket milled out to hold the chip in place. Two small grooves

Chamber Lid

Magnet
Retaining Bracket

Magnet Assembly
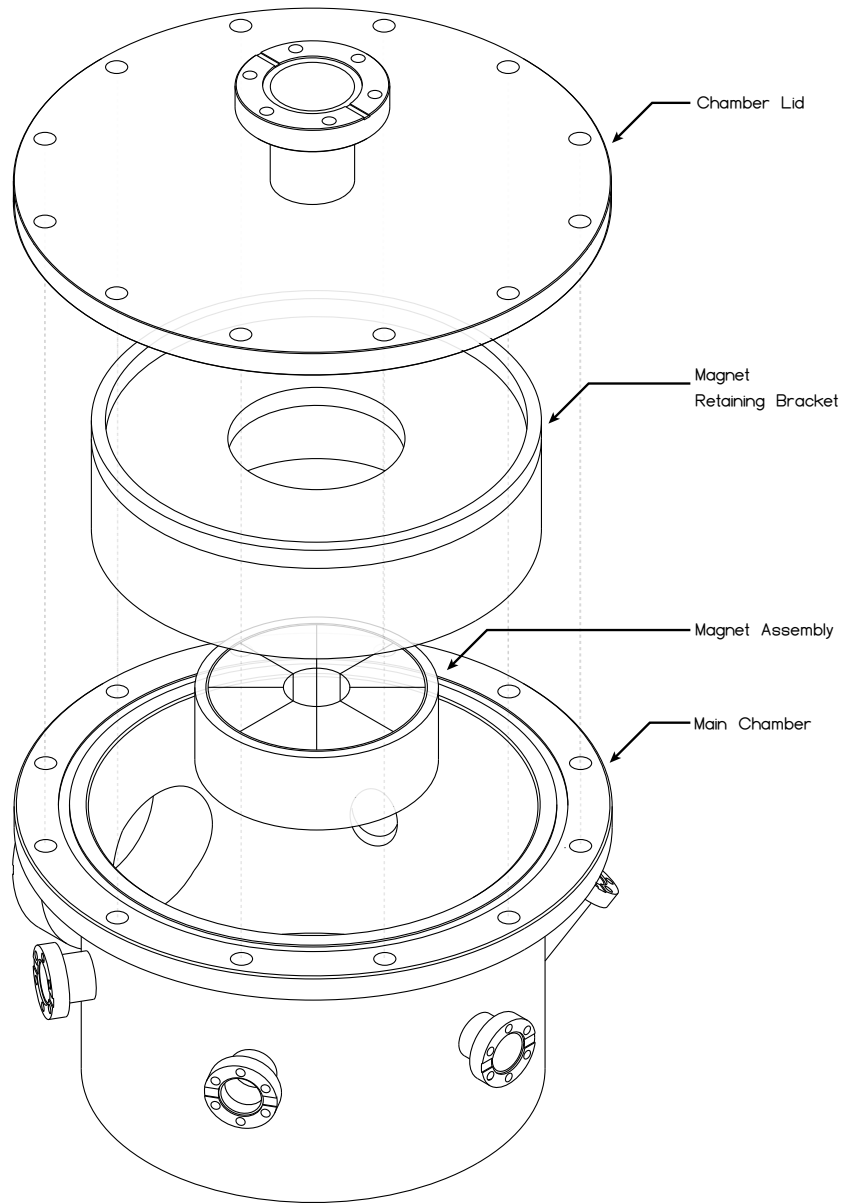
Main Chamber

Figure 4.3: Exploded view of the main chamber of the vacuum system. The retaining bracket slides over the magnet array and locks it in place, controlling the hazard associated with the extremely powerful magnetic field.

Figure 4.4: Photograph of interior of the main chamber, with the magnet assembly and retaining bracket installed. The cables visible in the bottom of the photo carry control signals from the multi-pin electrical feedthrough to in-chamber electronics.

adjacent to the chip pocket allow the chip to be inserted and removed with fine-tipped tweezers. Two brass alignment pins extend from the cylinder, acting as guides to prevent lateral motion of the contact pin array when pressing the pins and chip into contact. Two threaded screw holes allow the contact pin array to be secured to the chip holder by means of brass screws, squeezing the assembly together and preventing the chip or contact pins from moving during measurement. The depth of the pocket was chosen so that the contact pins experience 50% compression when the fixture is closed with a chip in place. The complete assembly is illustrated in Figure. 4.5, while the relationship between the contact pin array and the chip is detailed in Figure. 4.6.

The top portion of the test fixture is a contact pin array, fabricated using traditional printed circuit board (PCB) techniques. Twenty five plated-through holes serve as attachment points for spring-loaded contact pins, which are soldered into place. Narrow traces on the top-side of the pin-array PCB carry instrumentation signals to arrays of plated holes around the board perimeter. Coaxial cables are soldered to these plated holes, carrying electrical signals to and from the board. Four un-plated holes serve to align the contact pin array board to the bottom half of the assembly, as well as to allow the two halves of the assembly to be joined together with brass screws.

For proper and repeatable electrical grounding of the test fixture, the grounded shields of each of the coaxial lines that connect to the perimeter of the test fixture board are soldered together with a fine wire. This wire is then taped to the aluminum body of the test fixture after the two halves are screwed together. Forming a ground connection at the test fixture provides a return path for current to flow in the coaxial cable, allowing the cable to function as a transmission line. The ground connections are taped to the aluminum body at multiple points, creating a lower-inductance path to ground, which reduces electrical parasitics associated with the test fixture. These parasitics appear as inductances in series with the ground connections in the equivalent circuit for the system, creating a potentially complex and unpredictable frequency response. Minimizing the length of electrical

Brass Screws

Contact Pin Circuit Board

Spring-Loaded Contact Pin Array

Halbach Magnet Assembly

Brass Alignment Pins

Aluminum Chip Holder
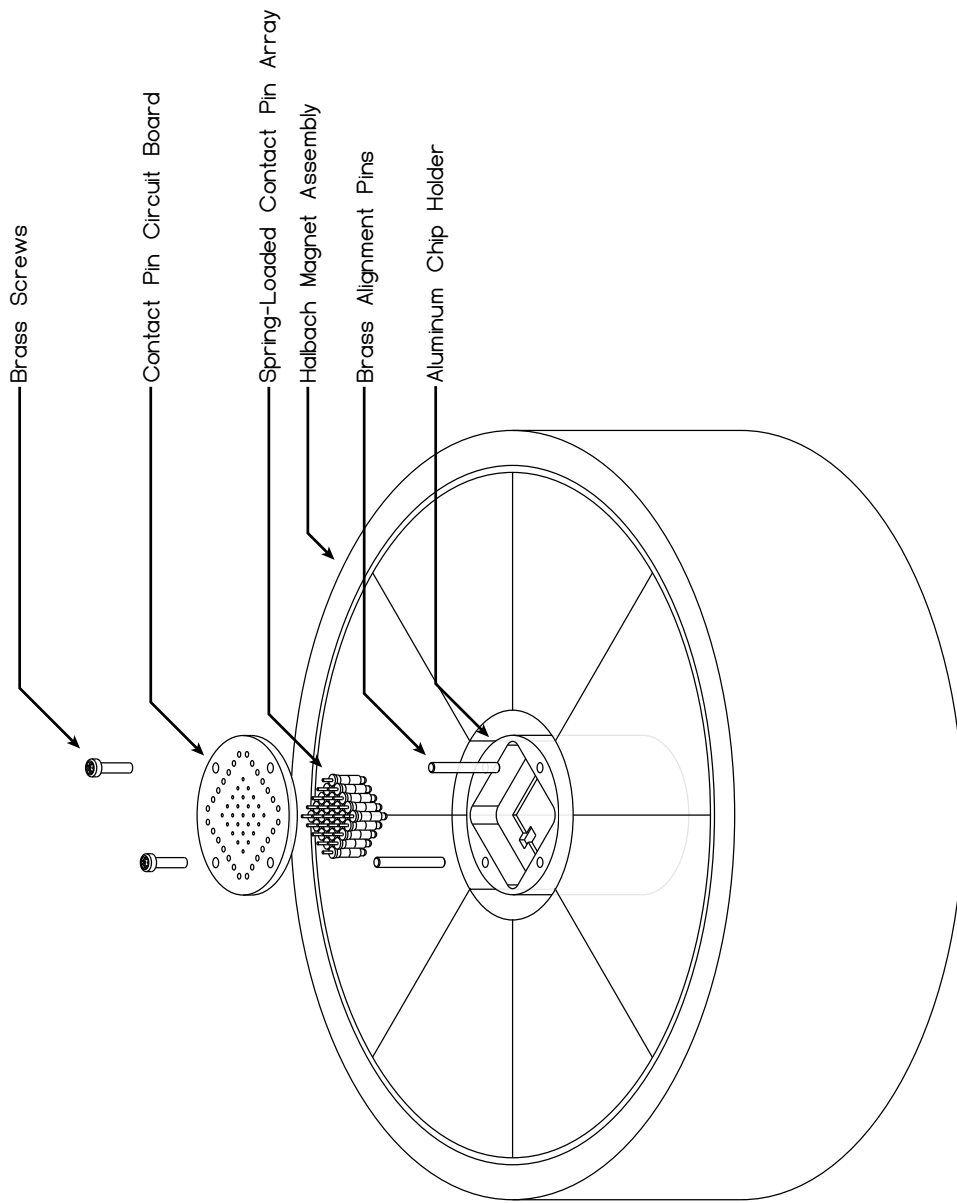
Figure 4.5: Test fixture for magnetomotive actuation and detection of resonators, exploded view.
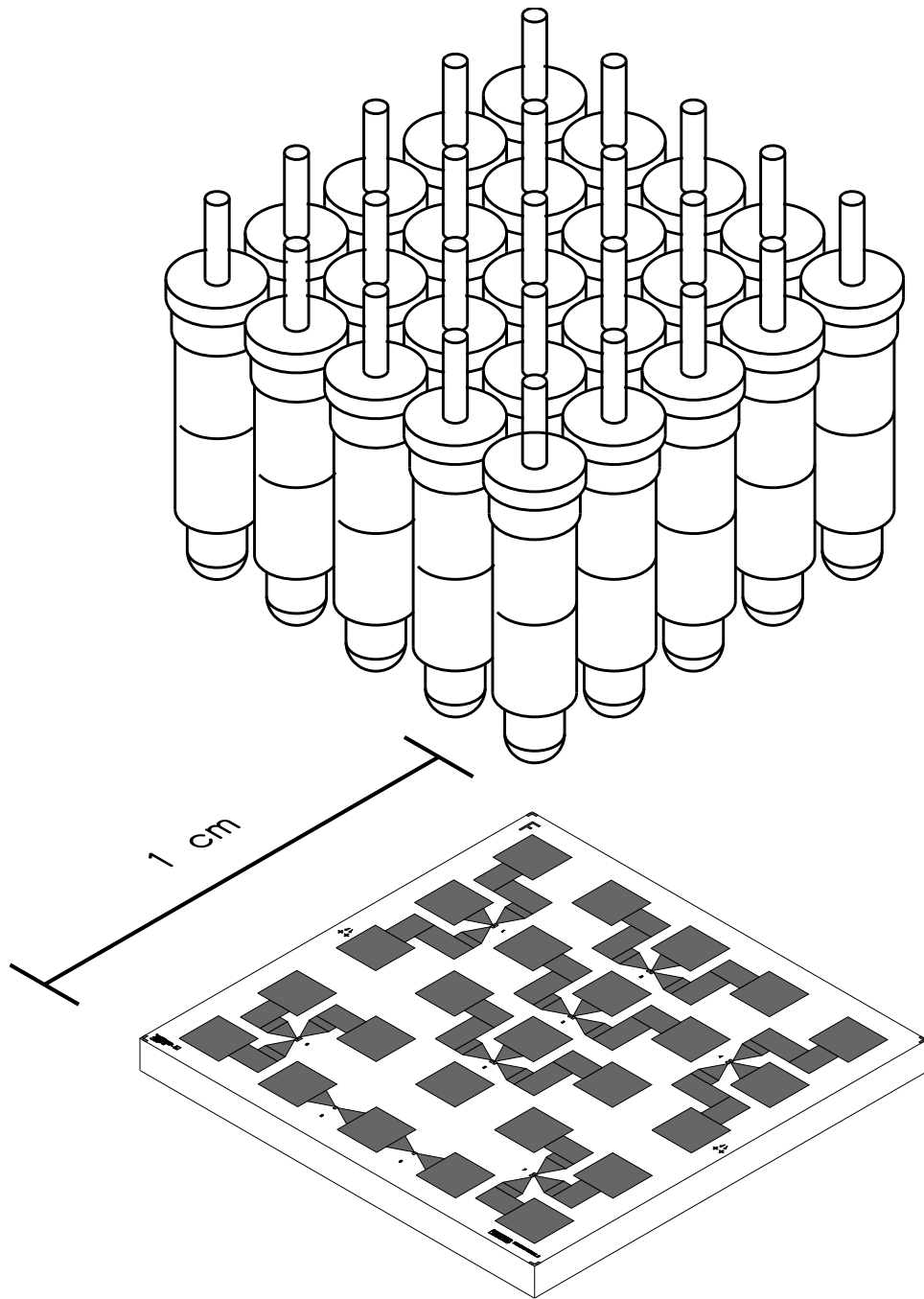
Figure 4.6: Detail of contact pin array interfacing with the contact pads on the chip.

connections on the board and in the test fixture helps to mitigate this issue.

Of course, these parasitics cannot be defeated entirely. The small traces that convey the instrumentation signals to the contact pins, as well as the contact pins themselves, each exhibit a small amount of parasitic inductance. Considering that each contact pin behaves as a small segment of wire with a length of 0.65 cm and a diameter of 1.5 mm, each pin is expected to contribute on the order of 1 nH of series inductance to the test setup. The thin traces (0.250 mm wide, about 1 cm long) on the contact PCB each contribute a few nanohenries of series inductance as well. Finally, parasitic capacitance between the contact pins and traces gives rise to crosstalk which threatens to swamp the electrical response of resonators on the chip. The precise values of inductance are difficult to calculate, as they depend strongly on the spatial arrangement of the current-carrying elements.

These issues can be greatly reduced by use of a *balanced* measurement configuration. Exciting two nearly-identical resonators in anti-phase causes crosstalk to partially cancel. The impact of parasitic elements in each signal branch is reduced as well, as only the relative *difference* between the parasitics, rather than their absolute magnitude, contributes to the system response. By exploiting symmetry, and by roughly matching the electrical lengths of the signal traces on the PCB corresponding to a particular set of devices, the effect of these unavoidable parasitics and crosstalk can be reduced by orders of magnitude. Careful electrical tuning can further null the effect of mismatch. This topic is elaborated further in Chapter 5.

4.4   Future Improvements

As designed, the vacuum system is capable of performing the most basic measurements on resonant MEMS and NEMS devices. A number of improvements to the system would unlock the ability to do much more exhaustive sensor characterization. For instance, the integration of a gas delivery system would allow for testing sensor speed and specificity with a variety of test gasses. This could be accomplished by running a gas line inside the chamber, with an exit point in the test fixture, ensuring gasses

are delivered directly to the chip. Another possible improvement would be to substitute the vent and/or roughing valves with a computer-controlled valve, so as to automate pressure control, simplifying experimentation with different damping regimes.

Chapter 5

Instrumentation Design – Electrical

5.1 Introduction

It not surprising that the small dimensions of our resonant MEMS and NEMS devices present a serious challenge in terms of instrumentation for detection of motion. As devices are scaled down in size, so too are the effects that we exploit to measure their behavior. For instance, tiny devices yield vanishingly small position-dependent capacitances, rendering capacitive actuation and detection a significant engineering challenge for all but the largest resonant sensors [17]. Traditional piezoresistive readout techniques suffer too: small piezoresistive resonators exhibit a large electrical resistance, which creates a low-pass filter when coupled with parasitic capacitances in the chip or measurement apparatus [5]. Furthermore, the application of magnetomotive actuation and detection schemes are complicated by the fact that the electrical impedance of geometrically-small devices changes only by a minuscule amount at resonance.

Gated time-domain techniques were developed to separate drive and readout signals in magnetomotive devices [4], but these techniques are difficult to scale to high-frequencies. Optical readout can in some cases address the issue of the detection of small displacements [17], but at the expense of

integration, and considerable complexity of apparatus.

The solution to this issue of electrical readout in small resonators appears to be the use of balanced-bridge measurement techniques. Pioneered by Dr. Ekinci with the Roukes group in 2002 [27], this family of measurement strategies are all variations on a simple theme: an electronic bridge, delicately balanced when out of resonance, is unbalanced by the mechanical resonance of one of its elements. The signal from the common port of the bridge is then amplified and detected, allowing fundamental resonance parameters such as resonant frequency and quality factor to be measured. Furthermore, the amplified signal from the bridge can be integrated into a phase-locked loop (PLL) so as to perform sensing experiments [29], measurements of resonator stability [48], and more. Figure. 5.1 shows the general measurement configuration.

Crucial to the success of this measurement strategy is that the bridge be as finely balanced as possible when just out of resonance. Any intrinsic unbalance in the system gives rise to an insidious background signal which can easily swamp out small resonances [27]. This unbalance can be due to unavoidable variations between devices or bridge elements, imperfections in the test fixture, differences in electrical length between the two signal branches, as well as frequency-dependent amplitude and phase unbalance in the splitter. These errors are pervasive, and together act to raise the background signal level. For instance, a typical 180° splitter [49] has an amplitude unbalance specified as 0.5 dB. This error alone, assuming perfect summing of the two signal branches, yields a background signal only 60 dB below the drive signal power. The often minuscule resonator response rides on top of this background signal, making detection difficult. In practice, all of the non-idealities of the system conspire to produce a complex and unpredictable frequency-dependent background signal. Figure. 5.2 illustrates a typical resonator response in the presence of a significant background signal.

This problem of background nulling can be addressed by fine-tuning the amplitude and phase of both drive signals at the time of measurement so as to minimize the background signal. Insertion of a precision variable attenuator and phase shifter in each signal branch allows the bridge to be
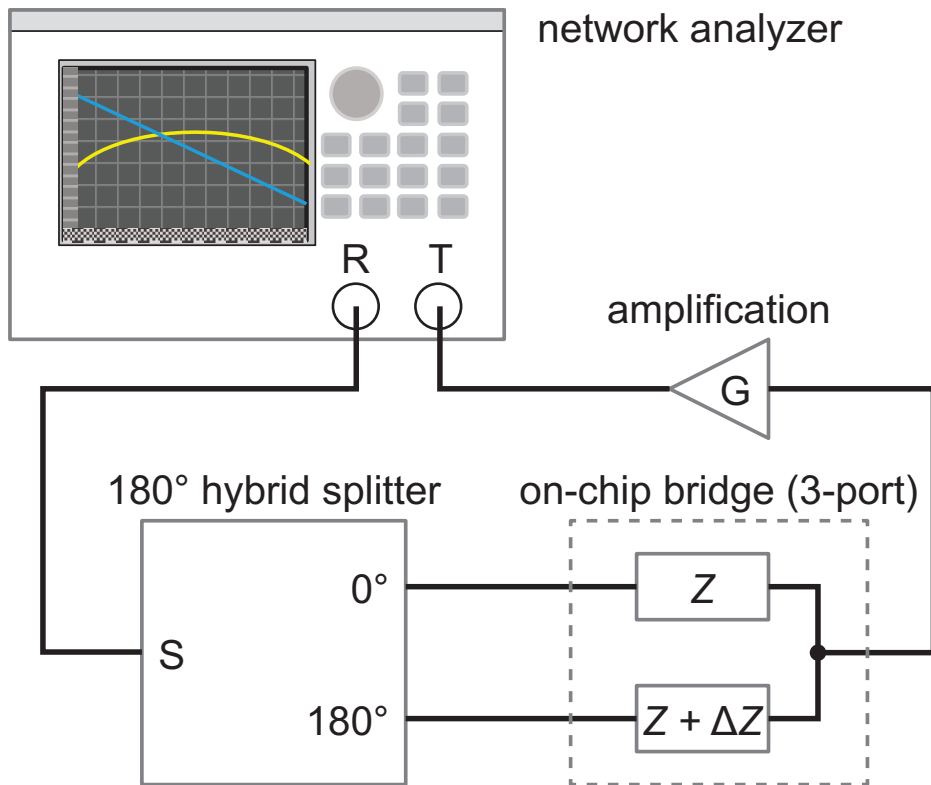
Figure 5.1: Basic configuration for the balanced-bridge measurement scheme — A 180° splitter generates two anti-phase drive signals that are summed using an on-chip bridge. Note that both bridge elements are nearly identical MEMS or NEMS resonators. ΔZ represents the change in impedance of a single bridge element due to mechanical resonance. The resonance of this element upsets the delicate balance of the electronic bridge, and the resulting unbalance signal is amplified and detected.
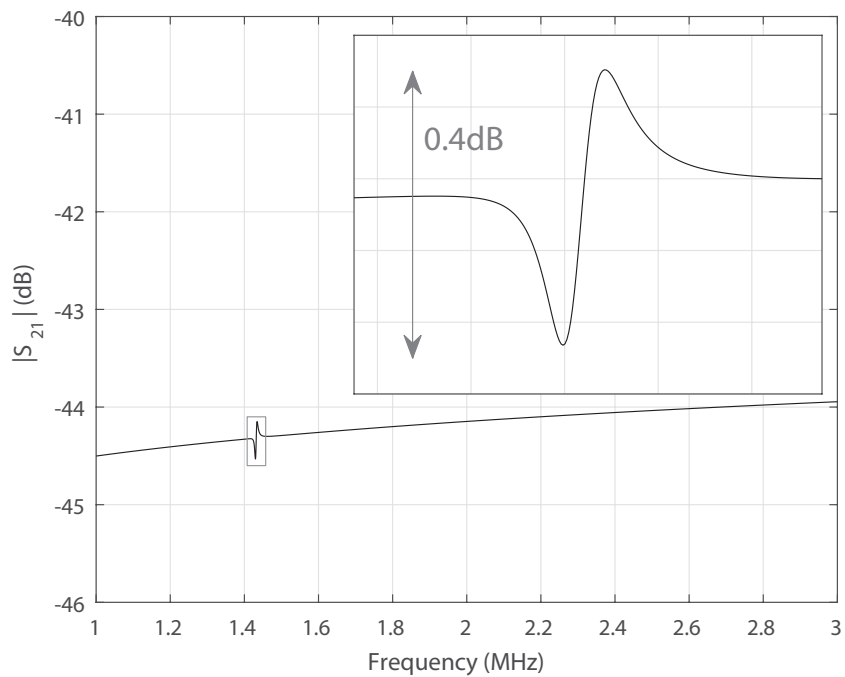
Figure 5.2: Typical resonator response in a system with imperfect balance — The background swamps out the signal due to the resonator, and significantly decreases the maximum peak excursion of the resonator response, making measurement difficult. Inset: Expanded view of resonator response.

adjusted for maximum off-resonance signal cancellation. This approach has been demonstrated in the domain of UHF NEMS, using precision attenuators and variable delay lines [48].

The challenge, then, is to scale the technique in [48] down to the more accessible field of HF and VHF NEMS resonator instrumentation in an accessible way. Unfortunately, wideband phase-shifter modules that cover both the HF and VHF bands are hard-to-find specialty parts, and when they do exist, they typically have a problematically narrow range of adjustability at the low-frequency end. Furthermore, commercial precision variable attenuators are typically adjustable over a rather large range, making the milli-decibel adjustments called for in this background nulling application difficult. Finally, these modules are expensive — the researcher is paying for *accuracy* when the application only calls for *precision*. These conflating factors suggest a unique opportunity to introduce a custom balancing circuit to solve the problem of making fine adjustments over a wide frequency range and at a low cost.

This section of the thesis concerns itself with the design, implementation, and testing of an electronically-adjustable balancing circuit for application in MEMS and NEMS sensing. The circuit as presented is broadband, and suitable for integration with a wide variety of balanced measurement schemes. Four points of adjustment allow the amplitude and phase in both signal branches to be controlled with extreme precision, allowing signal cancellation to better than 100 dB when summed directly. We evaluate the performance of our design by verification with a vector network analyzer, as well as through *in situ* testing using two previously reported variations on the balanced measurement technique.

5.2 Balancing Circuit Design and Methodology

A block diagram of the balancing circuit is shown in Figure. 5.3, while a schematic of one half of the balancing circuit is shown in Figure. 5.4. A precision variable attenuator and a phase shifter are placed in each signal branch to allow the relative amplitude and phase of the two signals to be

adjusted. Such amplitude and phase adjustments, properly executed, can summarily compensate for the various sources of unbalance in the measurement system, reducing the background response.

The ultimate design goal of maximum background signal cancellation requires that the adjustments made be extremely precise. For the purpose of fine-tunability, we require that the signal attenuation be adjustable only over a narrow range of about 2 dB. Furthermore, we require that the phase of each branch be adjustable over a range of at least $0.5°$ across the operational bandwidth. This range of phase adjustment is required to allow for compensation of typical splitter unbalance and electrical length mismatch in the measurement apparatus. Finally, we would like our balancing circuit to maintain a 50 Ω characteristic impedance for easy interfacing with standard RF test equipment.

These requirements are, fortunately, easily met using off-the-shelf components. We implemented a current-controlled, precision variable attenuator using a long-carrier-lifetime PIN diode as a bias-controlled, variable AC resistance. The diode was designed into a standard resistive pi-attenuator, with a series resistor providing the bulk of the attenuation, decreasing the range of adjustment of attenuation and hence increasing precision. The use of a long-carrier-lifetime PIN diode allows operation at frequencies down to 1 MHz, and at signal powers of up to 1 mW (0 dBm). With the component values shown, the attenuator provides a good match to 50 Ω over the design bias range from 0–30 mA.
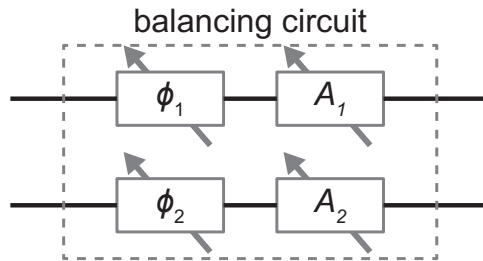
Figure 5.3: Block diagram for the balancing circuit.
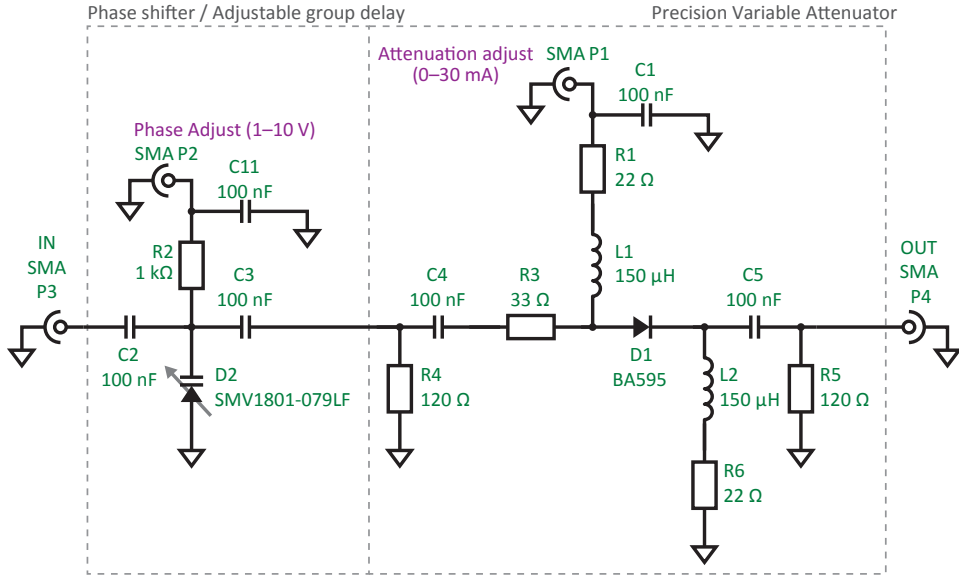
Figure 5.4: Schematic of one of two identical branches of the balancing circuit. A current-controlled precision variable attenuator follows a voltage-controlled phase shifter.

In order to deliver a finely-adjustable phase shift, we use a shunt variable-capacitance diode. The small diode capacitance, in combination with input and output impedances, implements a single-pole R-C low-pass filter with $R = 25$ Ω. For frequencies $f \ll 1/(2\pi RC(V))$, this circuit approximates a voltage-variable group delay of $2\pi RC(V)$ seconds — a natural compensation for electrical length mismatches in the system. This variable group delay corresponds to a range of phase adjustment of $1°$ at 1 MHz and $100°$ at 100 MHz, though violation of the above criterion at high frequency and low reverse bias limits the achievable phase shift at 100 MHz to a range of about $50°$, as will be elaborated on shortly. The small amount of amplitude loss due to the low-pass action of this stage can be compensated through adjustment of the variable attenuator.

Note that the attenuation and phase shift are not expected to be linear functions of bias. At low bias, the attenuation will change rapidly, as will the phase shift. This non-linear bias dependence is, in fact, an advantage:

the bulk of the unbalance in the system can be compensated for in one signal branch operating in this more sensitive region of bias. So long as the bias in the first branch is stable, the other branch of the circuit can then be operated in the less sensitive region — a powerful combination of coarse and fine tuning control. This additional level of control is a tremendous advantage over, for example, the bridge balancing technique in [50], which provides only two points of adjustment, each of which varies in sensitivity with frequency.

5.2.1   Biasing Considerations

Biasing of RF circuits can be a challenging problem. Ideally, a biasing network should have no effect on the RF signal path. Of course, perfect isolation of the biasing circuitry and the RF signal path is not possible. In practice, we ensure that the impedance of the biasing network is large compared to the impedances in the signal path over the design frequency range so that the biasing network interacts only minimally with the RF circuit.

In the case of the voltage-controlled phase shifter, biasing is easy: simply use a large-value resistor (Figure. 5.5). In our design, we use a 1 kΩ resistor to reverse bias the varactor diode D2. As 1 kΩ is large compared to the impedance of the signal path (50 Ω), very little signal is expected to couple back from the RF signal path.

Biasing the current-controlled variable attenuator is considerably more difficult. Consider first that both ends of the diode D1 must be isolated from the bias circuitry and ground. Next, consider that up to 30 mA of current must flow through the biasing network. The solution using resistive isolation, as shown in Figure. 5.5, would place a 1 kΩ resistor between the anode of D1 and the bias current supplied through connector P1, as well as another resistor 1 kΩ resistor between the cathode of D1 and ground. This current would drop 60 V across the biasing resistors alone, dissipating a massive 1.8 Watts of power. Clearly, a better solution is needed for biasing the PIN diode.
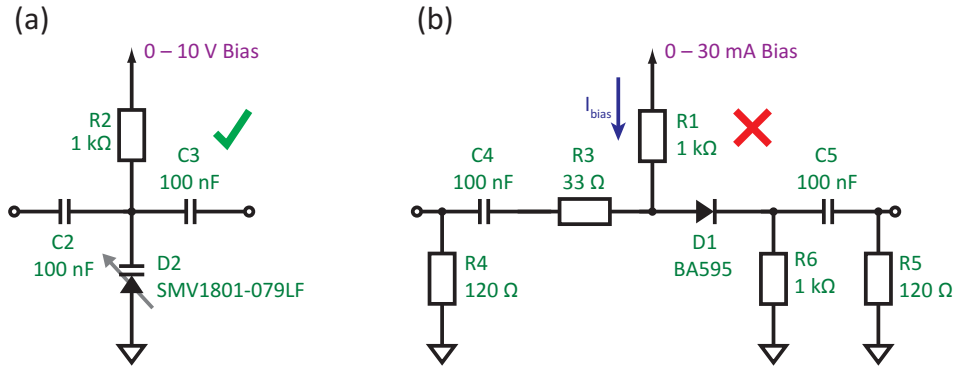
Figure 5.5: Resistive biasing of the voltage-variable phase shifter (a), and the current-controlled variable attenuator (b). Though this technique works for (a), in (b) the power dissipated in R1 and R6 makes this biasing scheme unattractive for the variable attenuator.

The solution is to use inductors in the bias path to provide isolation at design frequencies. The required inductance must be large enough to provide about 1 kΩ of impedance at the lowest operating frequency, which is 1 MHz. Considering that $|Z_\mathrm{L}| = 2\pi f L$ for an inductor, this gives a lower bound of inductance of about 159 μH.

Were inductors anything near ideal components, this calculation would be sufficient, and we could use any inductor with $L > 159\mu$H to isolate the bias circuit from the RF signal path. In reality, however, inductors suffer parasitic capacitance and resistance which together serve to limit their performance. This parasitic capacitance is, in part, a distributed capacitance associated with energy stored in the electric field between the inductor windings. Figure. 5.6 shows an equivalent circuit which models the performance of the inductor in the presence of parasitic effects [1], while Figure. 5.7 displays a log-log plot of the absolute magnitude of impedance vs. frequency for a real inductor.

As can be seen from the plot in Figure. 5.7, the impedance of the real inductor begins by rising linearly in frequency, and well approximates an ideal inductor. In this regime, the parasitic capacitance exhibits a very large reactance in comparison to the small reactance of the inductor, and

Ideal Inductor   Real Inductor
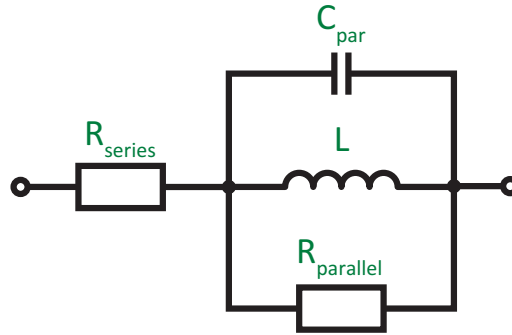
Figure 5.6: Equivalent circuit for a real inductor, including resistive losses and parasitic capacitance. [1] The resistance R_{series} models equivalent series resistance of the coil. The parallel resistance $R_{parallel}$ is typically very large $> 1k\Omega$ and models losses in the inductor. In a modelling sense, $R_{parallel}$ determines the maximum impedance of the inductor, which is reached at self-resonance.

can be neglected. At a frequency known as the self-resonant frequency, or SRF, the reactances of the parasitic capacitance and the inductance are equal and opposite, forming a parallel-resonant LC circuit. This resonance causes the impedance of the inductor to peak at a large real value, limited by losses in the inductor.

Beyond the SRF, the impedance of the real inductor decreases approximately linearly with frequency, and thus behaves like a capacitor. This happens when the reactance of the parasitic capacitance is much smaller in magnitude than the reactance of the inductor, essentially bypassing the inductor. When used to isolate an RF signal and a biasing network at frequencies beyond the SRF, the isolation will *decrease* with increasing frequency – quite the opposite of what we would expect from an ideal inductor!

Finally, the SRF of an inductor tends to decrease with increasing inductor value. This unavoidable trend is made clear when we consider the approximate formula for the SRF of the real inductor: $\text{SRF} = \frac{1}{2\pi\sqrt{LC_{par}}}$.

All else held equal, a larger value of inductance gives a lower SRF, which negatively impacts isolation at high frequencies. Worse yet, larger-value inductors tend to exhibit a larger parasitic capacitance C_{par} due to increased capacitance between the windings. These conflating factors suggest that we use the smallest serviceable inductor to isolate our biasing circuitry from our signal path.

For our application, we consider the Murata LQH3NPN151NG0L 150 μH inductor, which has a minimum rated SRF of 10 MHz. [51] To a first approximation, $C_{\text{par}} = \frac{1}{4\pi^2 f_{\text{SRF}}^2 L}$, which gives a parasitic capacitance of only 1.7 pF. At the highest operating frequency of 100 MHz, we are a decade beyond the SRF, and can safely treat the (real) inductor as a 1.7pF capacitor. The impedance of such a capacitor at 100 MHz is 936 Ω, just shy of our 1 kΩ target, but serviceable nonetheless. Figure. 5.7 shows the design criterion of $|Z_{\text{inductor}}| > 1k\Omega$ superimposed on a log-log plot of impedance vs. frequency for this particular inductor.

5.3   Balancing Circuit Modelling

In this section, we develop a simplified model for the attenuation and phase shift of a single branch of the balancing circuit. This model is useful when considering the effect of part substitutions on balancing circuit performance. We analyze the behavior of the attenuator and phase-shifter separately, assuming that each successive stage of the circuit presents a 50 Ω characteristic impedance load to the previous section.

5.3.1   Current-Controlled Variable Attenuator

The current controlled variable attenuator is essentially a standard π attenuator, with part of the series resistance contributed by the PIN diode. A pi-attenuator with shunt resistances R_1, series resistance R_2, and a characteristic impedance Z_0 of 50 Ω introduces an attenuation A as follows:

$$A = -20 \log \left(2 \frac{R_1}{R_1 + Z_0} \frac{R_1 || Z_0}{2(R_1 || Z_0) + R_2} \right) \tag{5.1}$$
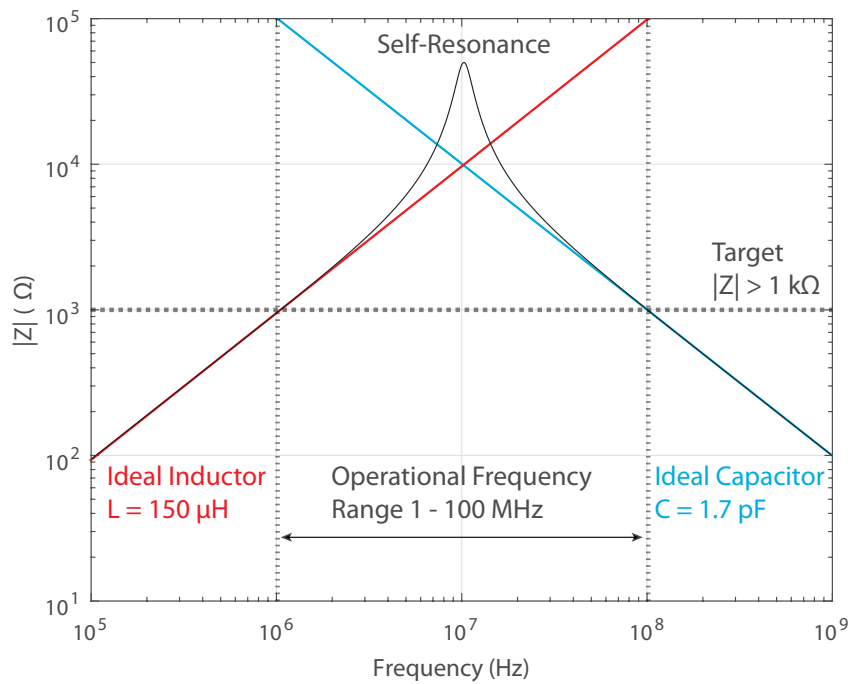
Figure 5.7: Impedance of a real 150 μH inductor on a log-log plot, with superimposed impedances of an ideal inductor and capacitor. The operational frequency range and minimum impedance design criterion are labelled on the plot. Note that the inductor near-perfectly satisfies the design criterion of $|Z| > 1k\Omega$ for our required frequency range.

In our circuit, R_2 is replaced by the series combination of a resistor R_s and the PIN diode, represented as a current-controlled resistance $R_D(I_{\text{bias}})$. Analysis of this circuit, pictured in Figure. 5.8, gives the following:

$$A = -20\log\left(2\frac{R_1}{R_1 + Z_0}\frac{R_1||Z_0}{2(R_1||Z_0) + R_s + R_D(I_{\text{bias}})}\right) \qquad (5.2)$$

All that remains is to determine the form of R_D. The basic physical model for the AC resistance of the PIN diode in forward bias is as follows: [52]

$$R_D = \frac{W^2}{(\mu_n + \mu_p) \times \tau I_{bias}} \qquad (5.3)$$

For the purposes of design, we are not interested in the precise values of these additional parameters. What is important, rather, is that the model predicts that the AC resistance of the diode goes as $(I_{bias})^{-1}$. Furthermore, in a real diode, the packaging and contacts contribute a small, fixed resistance that cannot be neglected. [52] These considerations, taken together, suggest the following model for the PIN diode:

$$R_D = \frac{p_1}{I_{bias}} + p_2 \qquad (5.4)$$

In which parameter p_1 absorbs all the device parameters from (5.3) and p_2 models the fixed packaging and contact resistances. Fitting this model to the forward resistance vs. bias current curve of the PIN diode datasheet
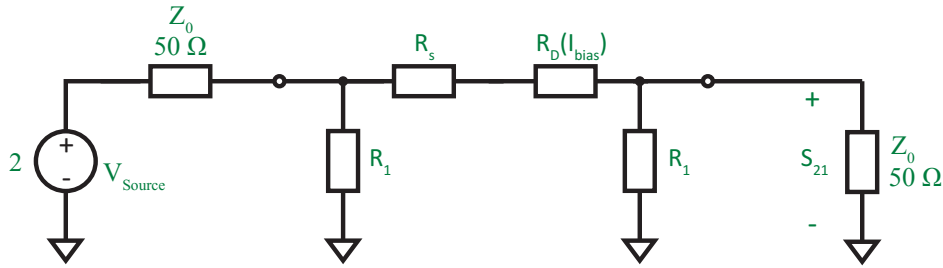
Figure 5.8: Simplified circuit model for the PIN diode attenuator. Note that attenuation $A = -20\log(S_{21})$ dB.

using least-squares regression (Figure. 5.9) completes the PIN diode model.

With this model in hand, we substitute for R_D in (5.2). The theoretical model is plotted alongside measured data from both circuit branches below, in Figure. 5.10, demonstrating exceptional agreement between theory and experiment. The small amount of additional attenuation in the measured data (about 0.1 dB) can be explained by the coupling of a small amount of signal power into the PIN diode bias network.

5.3.2 Voltage-Controlled Phase Shifter

The voltage-controlled phase shifter is essentially a shunt variable capacitor to ground. This variable capacitor $C_{shunt}(V_{bias})$ is implemented by varying the reverse-bias voltage across a varactor diode. We may obtain a more accurate model by considering the effect of the (small) series resistance of the varactor diode R_s, as well as by considering the effect of the 1 kΩ biasing resistor R_{bias}, which appears in parallel with the shunt capacitance. The circuit for our analysis is illustrated below, in Figure. 5.11.

For this circuit, the (vector) transmission coefficient is calculated as follows:

$$S_{21} = 2 \frac{Z_0 || R_{bias} || (R_s + Z_C(V_{bias}))}{Z_0 + Z_0 || R_{bias} || (R_s + Z_C(V_{bias}))} \tag{5.5}$$

Where $Z_C(V_{bias}) = -j/2\pi f C(V_{bias})$ represents the voltage and frequency dependent impedance of the varactor diode capacitance.

All that remains to complete our model is to determine R_s and $C(V_{bias})$. From the datasheet for our varactor diode [53], $R_s \leq 1.2\Omega$. Diode junction capacitance $C_J(V_{bias})$ can be modelled using the following equation: [54]

$$C_J(V_{bias}) = \frac{C_{J0}}{\left(1 + \frac{V_{bias}}{V_J}\right)^M} \tag{5.6}$$

In which C_{J0}, V_J, and M are device-dependent parameters. A real varactor diode will have some associated capacitance C_P due to packaging [54], yielding the following formula for the total capacitance $C_T(V_{bias})$ of the
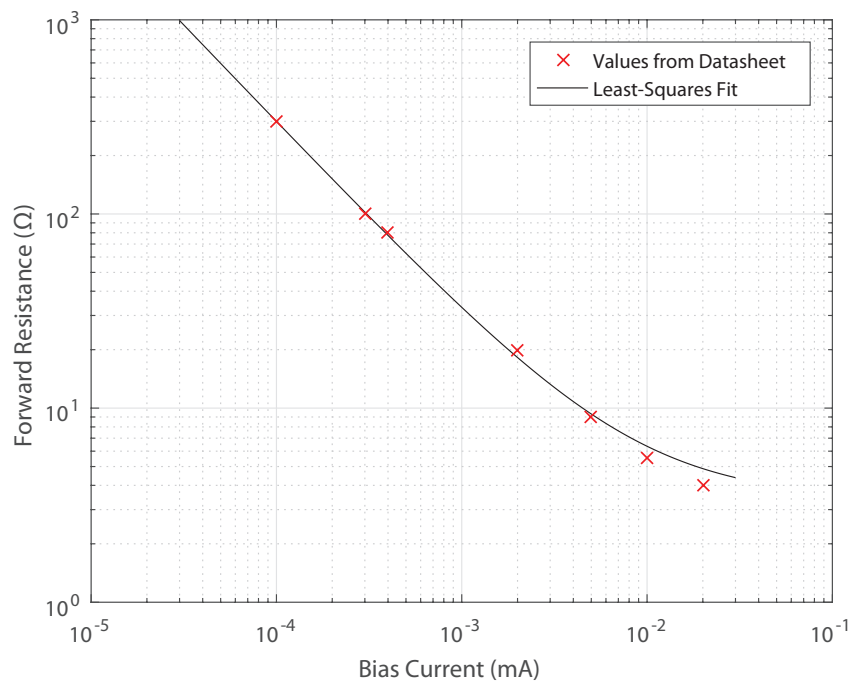
Figure 5.9: Least-squares regression fit of the model in (5.4) to the datasheet. Fit parameters $[p_1, p_2] = [29.7\text{mV}, 3.40\Omega]$
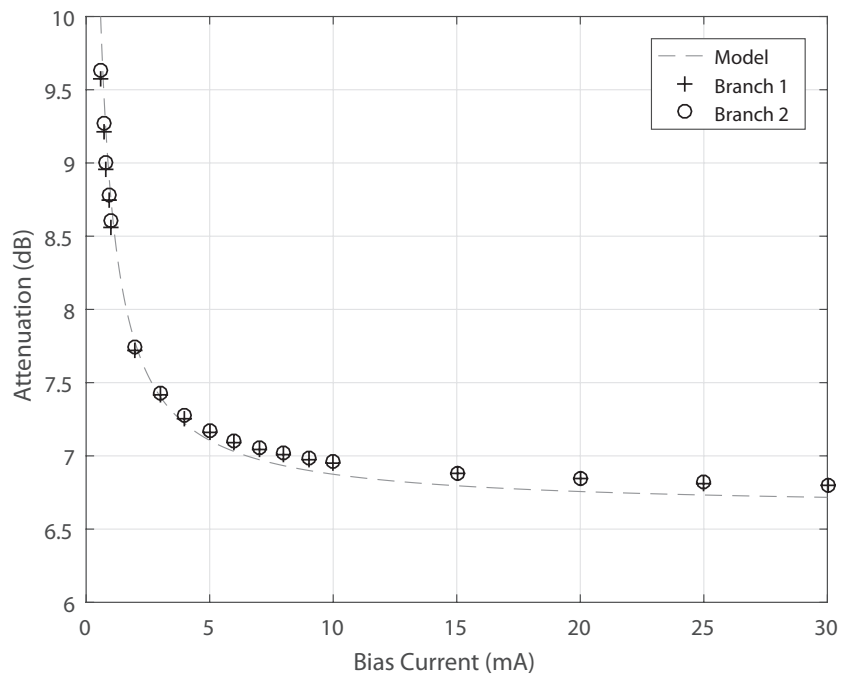
Figure 5.10: Model of attenuation vs. bias current, plotted alongside measured data from both signal branches of the balancing circuit, demonstrating exceptional agreement between theoretical (designed) and measured performance. Attenuation was measured at a test frequency of 10 MHz.
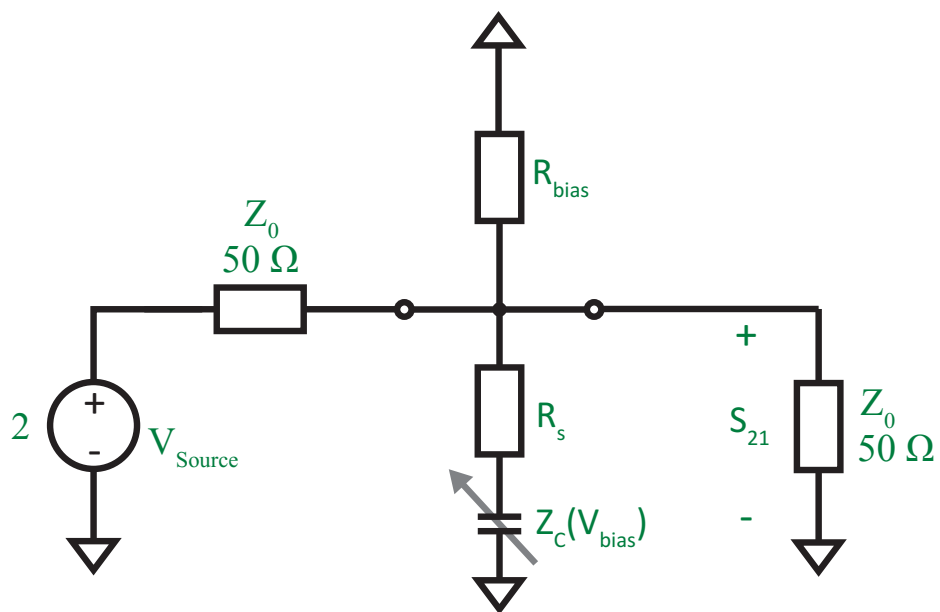
Figure 5.11: Simplified circuit model for analysis of the voltage-controlled phase shifter.

varactor as a function of reverse bias voltage:

$$C_T(V_{bias}) = \frac{C_{J0}}{\left(1 + \frac{V_{bias}}{V_J}\right)^M} + C_P \tag{5.7}$$

For the purposes of our modelling, we substitute these physical device parameters with modelling parameters p_1 through p_4, giving the following model to fit to the capacitance vs. reverse voltage data given in the varactor datasheet:

$$C_T(V_{bias}) = \frac{p_1}{\left(1 + \frac{V_{bias}}{p_2}\right)^{p_3}} + p_4 \tag{5.8}$$

The result of fitting the model in (5.8) to the capacitance curve in the datasheet is displayed in Figure.5.12.

For the purposes of our model, we choose $R_s = 1\Omega$ for simplicity. Substituting $Z_C(V_{bias}) = -j/2\pi f C_T(V_{bias})$ into (5.5) completes our model.

In Figure.5.13, we compare a family of phase-shift vs. frequency curves generated by our model to the measured set of curves from one branch of the balancing circuit. At both low and high reverse-bias voltage, our model accurately reproduces the behavior of the real phase shifter. At medium reverse-bias, the curves of our model are somewhat offset from the measured curves. This effect is likely due to manufacturing variations across varactor diodes.

Of particular interest for our application is the range of phase adjustability of the phase-shifter vs. frequency. The phase adjustment range is calculated by subtracting the phase-shift vs. frequency curve at 0V reverse bias from that at 10V reverse bias. The model is plotted alongside the measured phase adjustment range vs. frequency from both signal branches of the balancing circuit in Figure. 5.14, and exhibits remarkable agreement with our model.
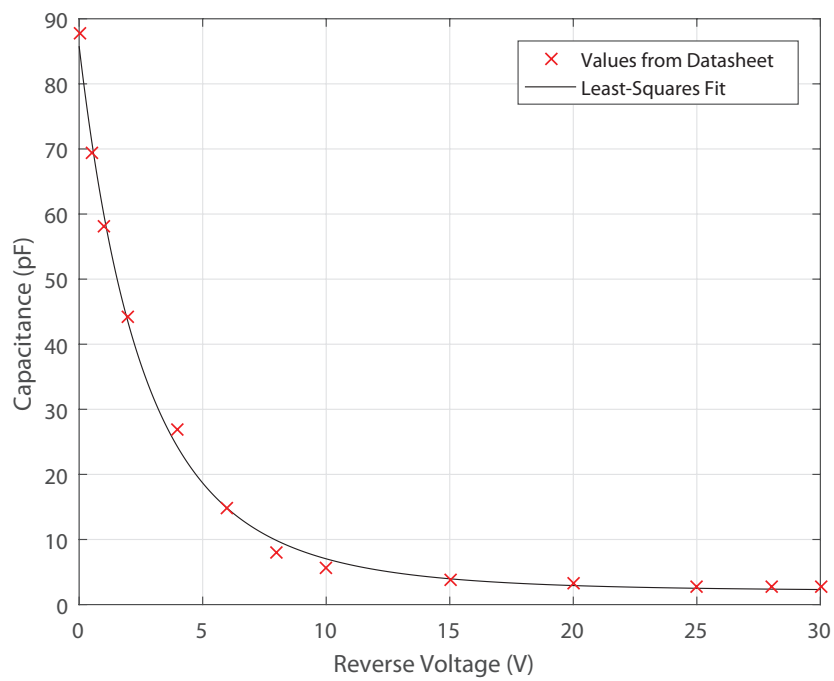
Figure 5.12: Least-squares regression fit of the model in (5.4) to the datasheet. Fitting parameters: $[p_1, p_2, p_3, p_4] = [83.71\text{pF}, 12.59\text{V}, 4.84, 2.08\text{pF}]$
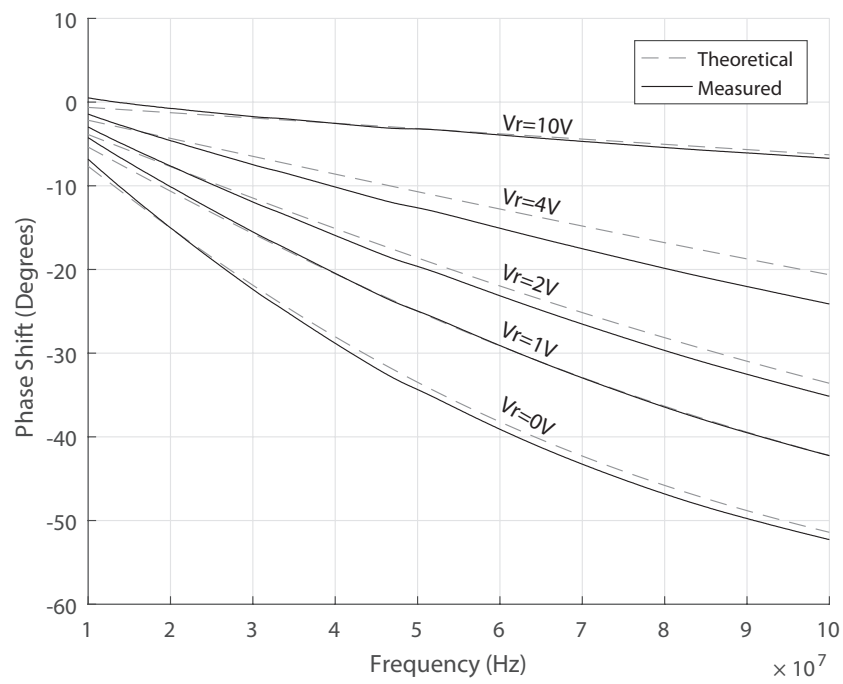
Figure 5.13: Family of phase-shift vs. frequency curves for one branch of the balancing circuit for several varactor reverse-bias voltages. Performance is consistent with our model.
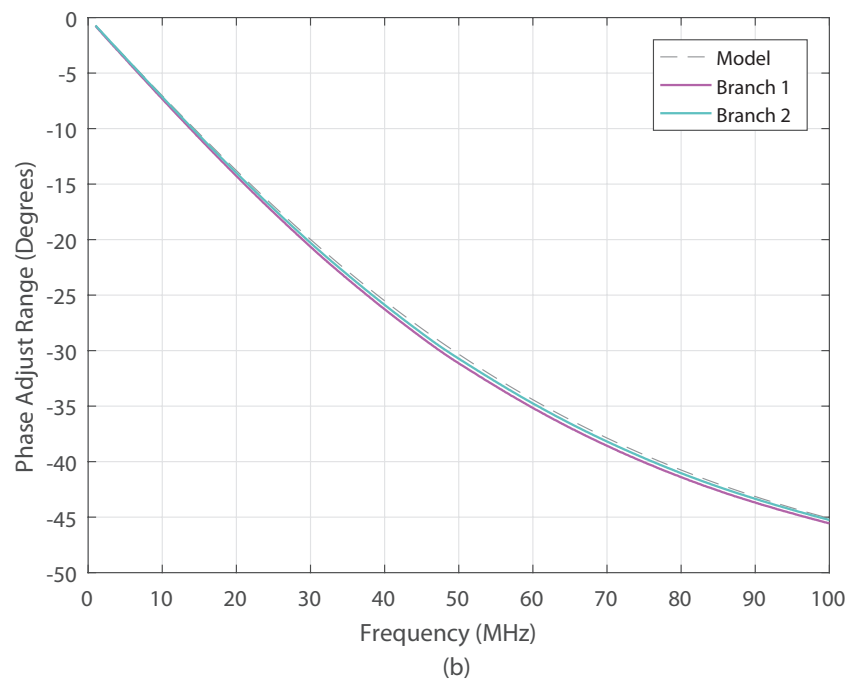
Figure 5.14: Phase adjustment range as predicted by our model, compared with the measured phase adjustment range of both branches of the balancing circuit. The measured data exhibits exceptional agreement with our model.

5.4 Control Circuit Design and Methodology

In order to control the balancing circuit, we require four independently-variable bias signals: two variable voltages for controlling the phase shifters, and two variable currents for control of the variable attenuators. These signals must be variable with extreme precision – the more precision we can achieve, the more finely we can balance our bridge circuit, improving the quality of our measurements. Furthermore, we require these bias signals to be both time and temperature insensitive, so that the generated output does not drift over time. Stable biasing allows us to collect data over a long time period without compromising our measurement, improving our ability to distinguish resonator response from noise. Finally, we need to ensure that the bias generator is stable under realistic loading – oscillation of bias signals would make balancing the bridge impossible.

One possibility is to use a collection of precision variable power supplies to bias the balancing circuit, but this approach would be difficult due to the level of precision required. For control of the variable attenuators, we need micro-ampere scale resolution. Likewise, for control of the phase shifters, we require millivolt-scale adjustability with concomitant stability. Furthermore, the amount of output ripple on a run-of-the-mill lab power supply is already on the order of a millivolt peak-to-peak, which would cause significant problems with biasing. (For instance, see the specifications sheet for the Keysight E3620A, a popular variable-output DC power supply. [55]) High-end power supplies can provide the precision and stability we require, but only at significant financial cost.

The solution we have chosen is to design a custom control circuit / bias generator to supply precision variable bias signals to the balancing circuit. Using 10-turn potentiometers to control the bias setpoints gives the precision we need for our application. The use of a time and temperature-stable voltage reference mitigates the effect of bias voltage drift, while precision resistors are used to precisely set the bias current. We use stability analysis to ensure that our circuit produces a non-oscillatory output for all reasonable loadings. Finally, we take extra precaution by filtering and regulating the

power supply of the circuit to prevent noise from being coupled from the power supply to the bias signals.

5.4.1 Precision Variable Voltage Sources

We generate the variable voltage bias for our balancing circuit using a voltage follower referenced off of a precision 10V voltage reference, as pictured in Figure. 5.15. For this application, we use the LMC6482AI CMOS-frontend operational amplifier. [56] This amplifier features an extremely-low input bias current, specified as 20fA typical, which prevents loading-down of the set-point potentiometer RV3, preserving the linear relationship between the potentiometer position (in degrees) and the output voltage. The small input offset voltage of this amplifier, rated as 750μV max, can be compensated simply by adjusting the potentiometer. More importantly, the input offset voltage drift is rated as only 1μV/$°$C, meaning that the output voltage will be extremely temperature insensitive.

Temperature Drift

The major coupling between temperature changes and output in this circuit occurs in the voltage reference, which has a typical temperature coefficient of 3ppm/$°$C, which at a full-scale output of 10V corresponds to 30μV/$°$C.

Propagating this 3ppm/$°$C bias drift through our model for the phase shifter, we can extract a family of curves for setpoint-dependent drift in $°$/$°$C, as a function of bias voltage and frequency (Figure. 5.16a). Furthermore, assuming we can set the potentiometer to within $1°$ (a conservative estimate), we can extract a family of curves describing the resolution to which we can reliably adjust the phase (Figure. 5.16b). The amount of temperature dependent drift is much smaller than the resolution with which we are capable of adjusting the phase, as required.

5.4.2 Precision Variable Current Sources

We use high-side current source circuits for generating the attenuator bias signals. Our circuit is pictured in Figure. 5.17. Potentiometer RV1 sets the
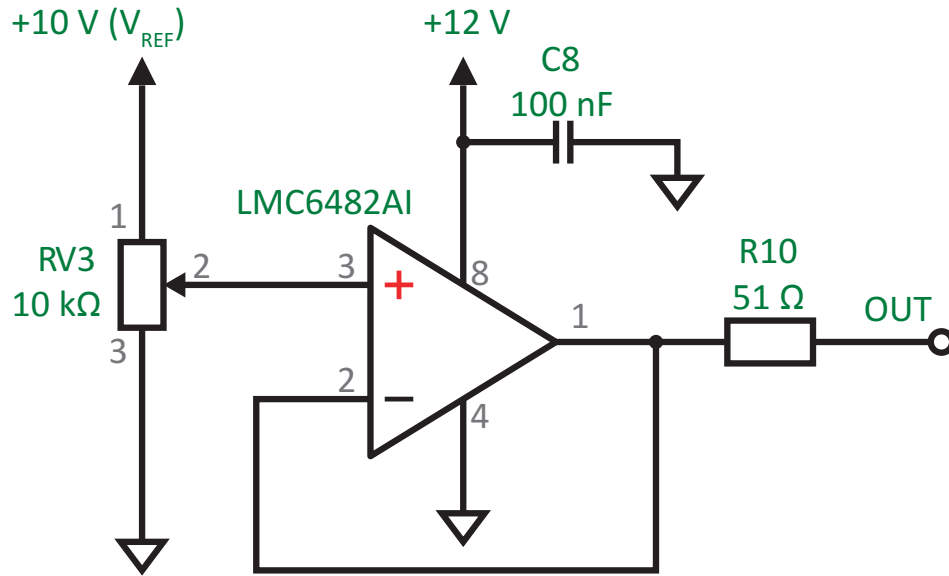
Figure 5.15: Variable voltage bias generator circuit (one of two identical subcircuits), based around a voltage follower. V_{REF} is generated using a precision 10V reference, the ADR01ARZ [2].
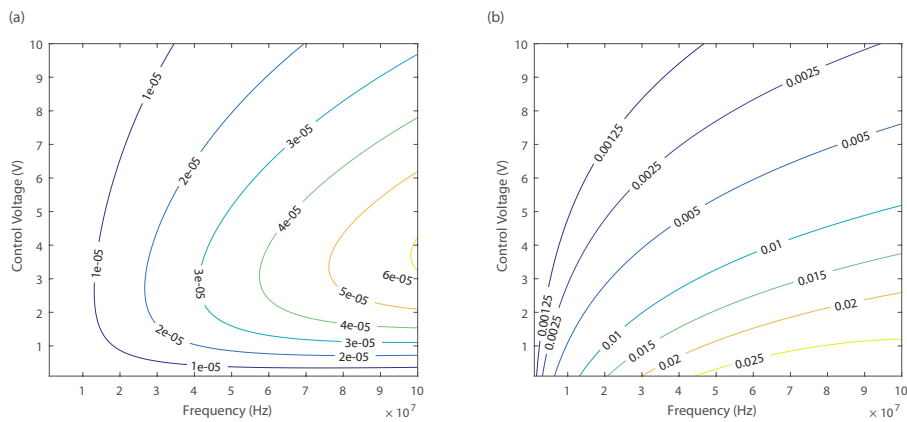
Figure 5.16: Temperature-dependent drift curves in $°/°C$ (a), and phase adjustment resolution curves in $°/°_{\mathrm{potentiometer}}$ (b), calculated using our model.

voltage across resistor R8. The current through R8 flows through R3, generating the control voltage for the second operational amplifier. That voltage appears on one leg of R4, setting the output current, which is buffered by the P-channel MOSFET Q3. The full relationship between the output current I_{out} and the position P of 10-turn potentiometer is as follows:

$$I_{\text{out}}(P) = V_{\text{CC}} \times \frac{P}{3600°} \times \frac{\text{RV1}}{\text{R2} + \text{RV1}} \times \frac{\text{R3}}{\text{R8}} \times \text{R4} \qquad (5.9)$$

Substituting component values, we find that our full-scale range of adjustment is from 0 to 31.58mA.

Temperature Drift

From consideration of (5.9) we can also determine the worst-case drift of the output current with temperature. The largest contributor is V_{CC}, which varies by $-1\text{mV}/°\text{C}$, generating a drift of $-83.3\text{ppm}/°\text{C}$. The resistive divider formed by RV1 (having a temperature drift of $\pm50\text{ppm}/°\text{C}$ and R2 ($\pm25\text{ppm}/°\text{C}$) produces a worst case drift of $\pm10.85\text{ppm}/°\text{C}$. Resistors R3 and R8 each contribute $\pm25\text{ppm}/°\text{C}$, while the sense resistor R4 contributes $\pm25\text{ppm}/°\text{C}$ as well. Assuming that all these drifts occur in the same direction, we obtain a worst-case drift of $-169.5\text{ppm}/°\text{C}$.

Important to note is that the transistor Q1 will experience a small increase in forward current gain B_{f} with increasing temperature, which tends to increase the output current. This effect is likely to be small, and would act to counteract the output current diminishing trend due to the temperature variation of V_{CC}. In the future, we could substitute Q1 with a small-signal MOSFET to eliminate this uncertainty.

In Figure. 5.18, we plot the effect of our calculated temperature drift on the attenuation of the current-controlled attenuator. On the same axes, we plot the achievable attenuation resolution, assuming a conservative $1°$ of potentiometer resolution. Drift due to the temperature dependence of the bias current is better than $0.001\text{dB}/°\text{C}$ beyond a bias current of $200\mu\text{A}$, and better than $0.0001\text{dB}/°\text{C}$ beyond about 4mA.
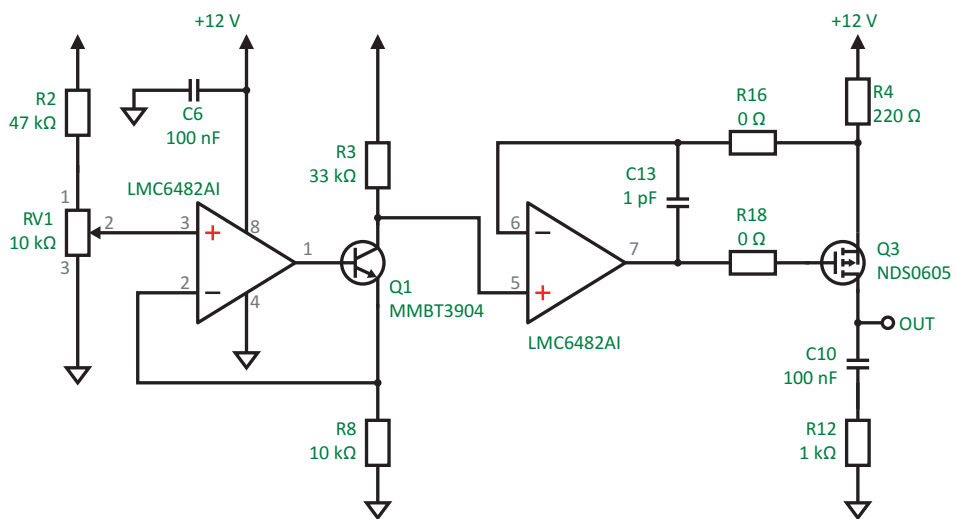
Figure 5.17: Variable current bias generator, based on a high-side current source circuit from the Art of Electronics. [3] The output current is controlled by sensing the voltage across the precision resistor R4, and is ratiometric. C13, C10 and R12 stabilize the current source for all reasonable output loadings.
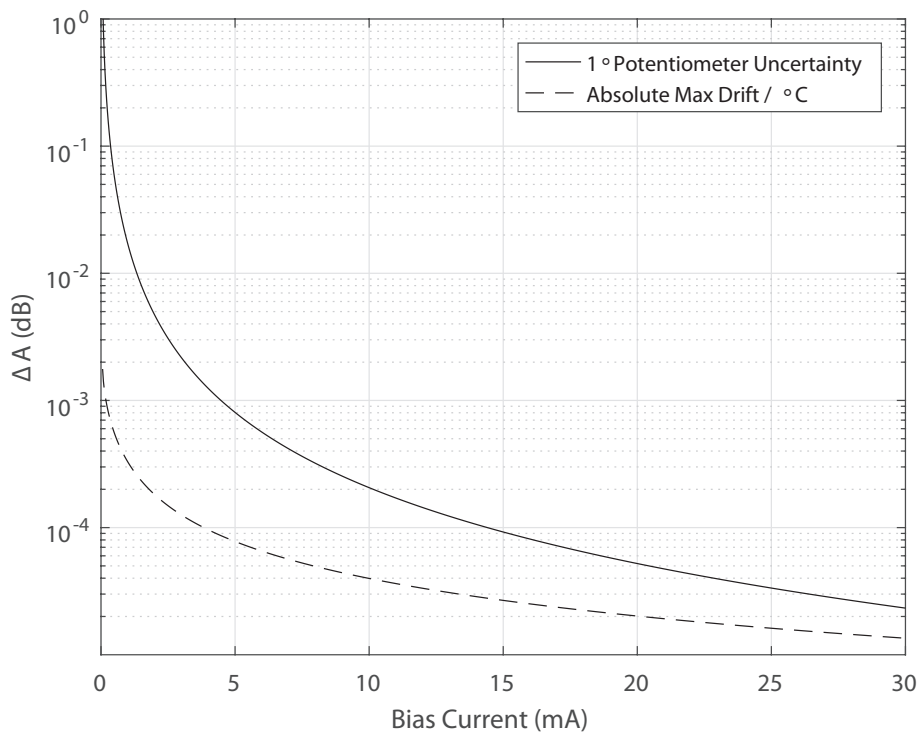
Figure 5.18: Temperature-dependent drift curve in dB/°C, plotted alongside the attenuation adjustment resolution curve in $\mathrm{dB}/^{\circ}_{\mathrm{potentiometer}}$.

Stability Considerations

The current source circuit must not oscillate under any realistic operating conditions or loadings. With this in mind, let us analyze the circuit in Figure. 5.17. The first operational amplifier, which interfaces with the potentiometer RV1, is not expected to pose any issue in terms of stability, as the base-emitter junction of Q1 appears, to a good approximation, as a resistive element in the equivalent AC circuit. Therefore, we do not expect the feedback network to contribute any additional phase shift in our control loop. Considering that the op-amp itself is unity-gain stable, and that this circuit is, in essence, a unity-gain follower with no additional phase shifts in the feedback network, the circuit is certainly stable.

The circuit comprised of the second op-amp, the MOSFET Q3, and the current-setting resistor R4 is slightly more challenging to analyze. The lagging phase shift due to the MOSFET gate capacitance, taken together with the phase-lag of the internally-compensated op-amp, threatens to throw the circuit into oscillation. However, our op-amp is rated to drive a 100 pF load at unity gain without oscillation. The NDS0605, with its typical gate capacitance of 79 pF, is thus unlikely to cause a problem here. Nevertheless, we design in a compensation network comprised of resistors R16 and R18, and feedback capacitor C13, to be used to stabilize the op-amp in the event that the MOSFET gate capacitance poses an issue. Were the gate capacitance to pose an issue, the first step would be to substitute a resistor of a few hundred ohms for R18. Following that, R16 and C13 can be chosen to introduce a pole in the loop gain function, throwing away gain at high frequencies for the sake of stability.

Finally, we evaluate the stability of our circuit for various output loads. It's important to note that the cables connecting our current source to the balancing circuit contribute some inductance to our load. This inductance can cause the output current to lag somewhat. This lagging current passes through R4, contributing to the phase lag of the loop gain function, potentially causing issue. To correct any potential issues with stability, we perform a loop gain analysis in LTSpice (Figure. 5.19).
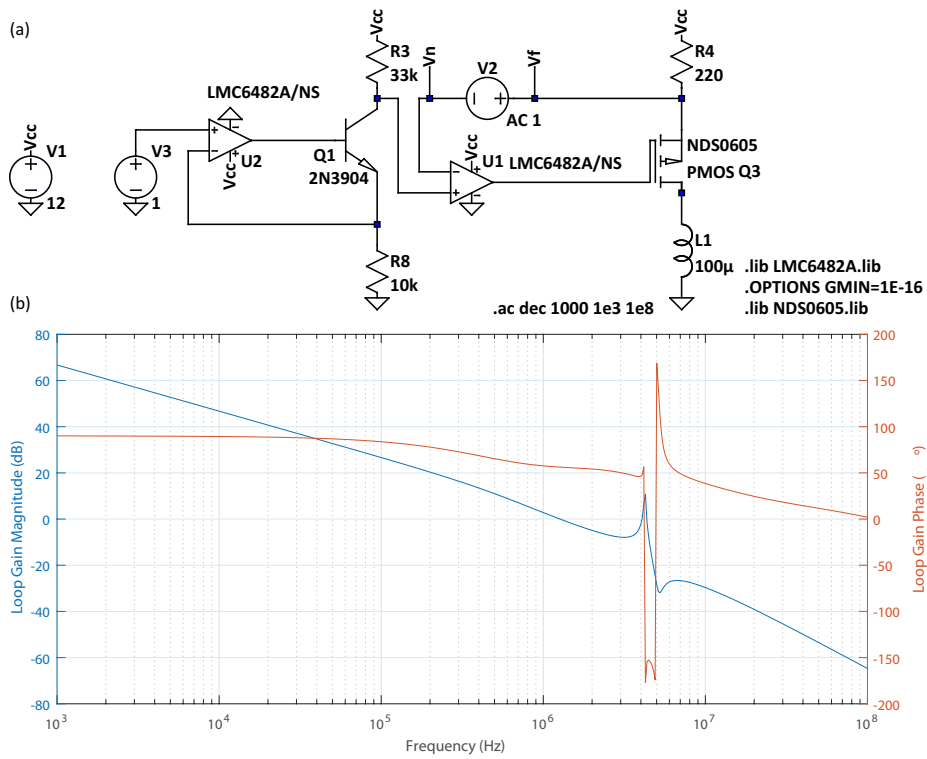
Figure 5.19: LTSpice Circuit (a) and calculated loop gain (b) for the current source subject to the 100μH load L1. The peaking of the magnitude of the loop gain beyond 0dB and the associated $180°$ phase shift indicate the circuit as described is unstable for this load.

We expect our connecting cables to contribute on the order of a micro-henry of inductance to the load. For the sake of ensuring circuit stability, we will exaggerate this greatly, and consider the performance of our current source given a purely inductive load of 100μH, represented as L1 in Figure. 5.19a. Note that we have, for the moment, ignored the resistor R12 and the capacitor C10 that were pictured in Figure. 5.17. We break the feedback loop with the small-signal AC source V2, labelling the feedback foltage Vf and the voltage at the inverting terminal of the op-amp Vn. Plotting V_f/V_n gives the loop gain of our circuit (Figure. 5.19b). The peak in loop gain magnitude just above 4 MHz and the associated 180° phase shift indicate the circuit is unstable with this load.

We introduce capacitor C10 and resistor R12 to the output of the circuit to restore stability in the presence of inductive loads. The loop gain of the corrected, inductively-loaded circuit is shown in Figure. 5.20b. With a phase margin of about 55° and a gain margin > 60dB, the circuit is certainly stable.

5.5   Construction

We constructed the circuit of Figure. 5.4 using surface-mount technology on a two-layer printed-circuit board, using the bottom copper layer as a ground plane. The constructed circuit is pictured in Figure. 5.21. The two RF signal branches were laid out as mirror-images of one another, so as to achieve the best intrinsic balance possible — any parasitic elements should appear identically in both branches, and should cancel out. Both bias and bridge signals are fed into the board using edge-mount SMA connectors for easy interfacing with RF test equipment.

The control circuit / bias generator layout was done on a 2-layer printed circuit board using a combination of surface-mount and thru-hole technology. We designed the circuit board to a standard 100mm width in order to fit common enclosures. For our enclosure, we selected the Hammond 1455N1201, a 103mm x 120mm x 56mm aluminum enclosure which was just large enough to fit the four required 10-turn potentiometers side-by-side

Figure 5.20: LTSpice Circuit (a) and calculated loop gain (b) for the corrected current source subject to the 100μH load L1. The phase margin is about $55°$, while the gain margin is > 60dB.
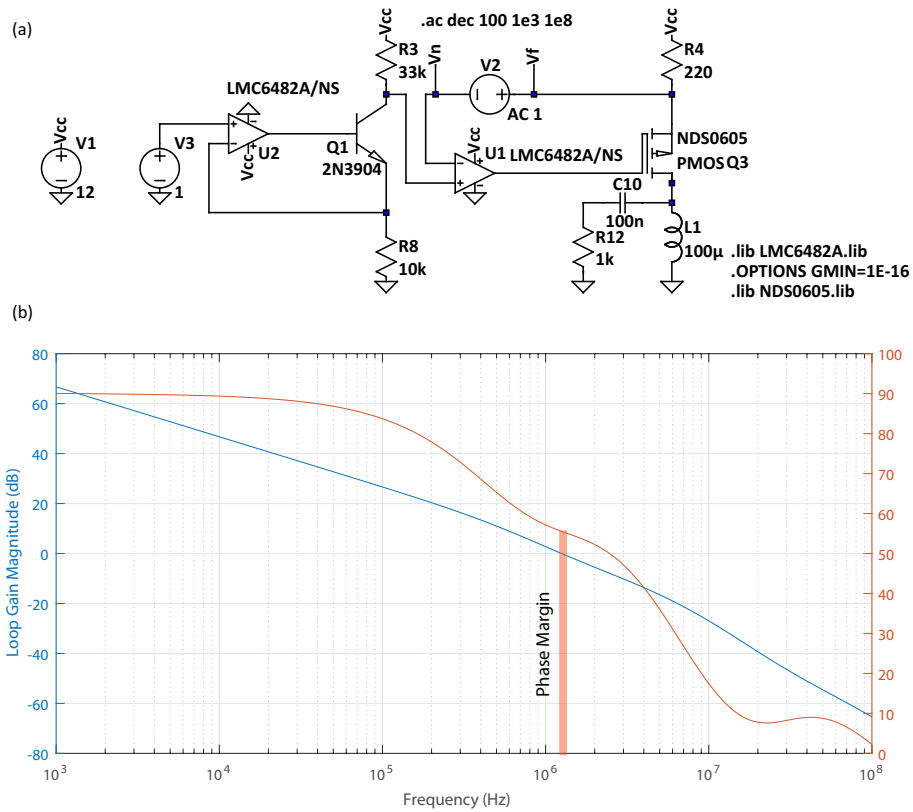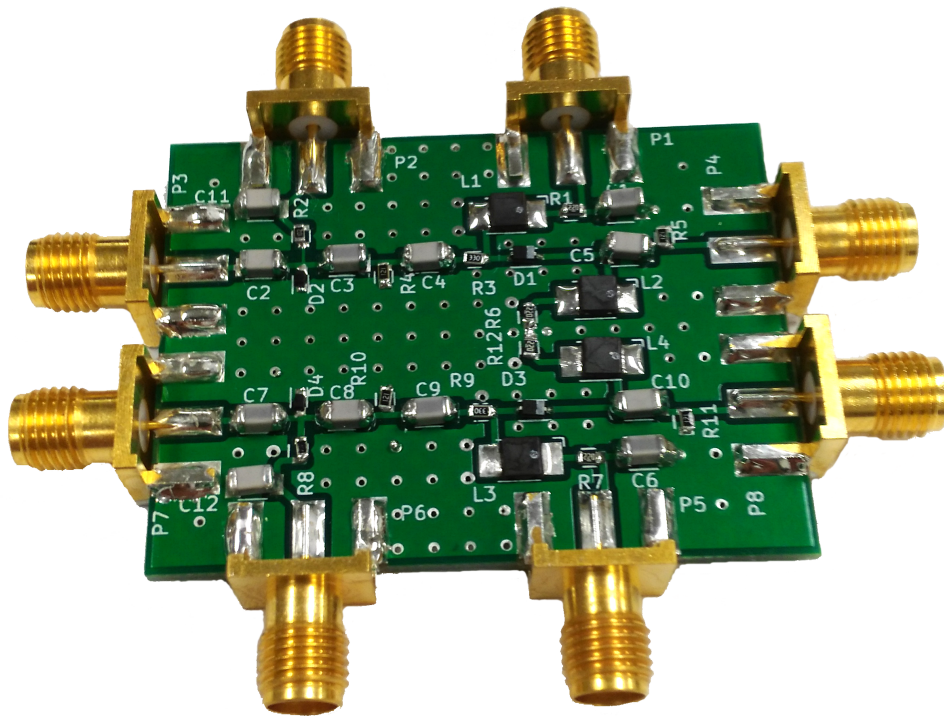
Figure 5.21: The bridge-balancing circuit, as constructed on a 2-layer PCB. Mirroring of layout between the two signal branches reduces imbalance due to parasitics.

on the front panel. A cable gland installed in the back of the enclosure prevents the connection points for the control signals on the board from suffering mechanical stress due to cable pulling. The control circuit is pictured in Figure. 5.22, while the front and rear panels of the fully-assembled control box are shown in Figure. 5.23.

5.6   Performance Tests

To verify correct performance of our circuit, we measured the attenuation and the phase shift of both signal branches as a function of applied bias. The measured performance data are plotted in Figure. 5.10, Figure. 5.13, and Figure. 5.14 alongside theoretical predictions which we calculated using the typical device performance curves provided by the manufacturers of the PIN [57] and variable capacitance [53] diodes. Agreement of the measured results with theory is good. Both signal branches exhibit nearly identical attenuation and phase shift *vs.* bias, indicating that the circuit is intrinsically well-balanced. Most importantly, the measured results verify that the circuit can provide the range of adjustment required in this application. Return loss of the attenuator was measured as better than 10 dB over the operating frequency range from 1–100 MHz, indicating a good match to 50 Ω. In practice, the degree of match is not very critical, as attenuators follow the balancing circuit to increase isolation.

One of the most basic functional tests of the balancing circuit is to generate two anti-phase signals and measure the amount of cancellation achievable by directly summing the two signal branches. The experimental setup for this test is elaborated in Figure. 5.24. Here, the balancing circuit simultaneously compensates for amplitude and phase unbalance in both splitter/combiners. Our typical achievable cancellation over a narrow bandwidth of about 1 MHz is about 100 dB, as indicated in the sample measurement plot of Figure. 5.25. In practice, the achievable bandwidth of maximum signal cancellation is a function of the frequency dependence of the unbalance in the test setup, and may be difficult to predict.

The circuit as shown in Figure. 5.4 is designed to operate from 1 MHz

117

Figure 5.22: The bias generator board mounted in the enclosure. The brown wires carry signals between the potentiometers and the board.

(a)

(b)

Figure 5.23: The bias generator, fully assembled. (a) Front panel and (b) rear panel. The different points of adjustment and major features are labelled.
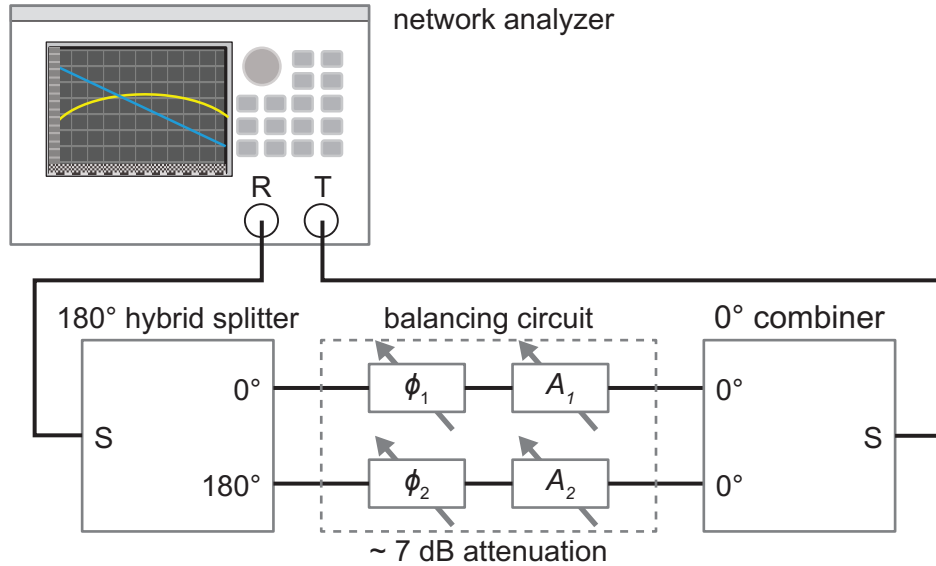
Figure 5.24: Experimental configuration for measuring the operational performance of the balancing circuit. Balanced anti-phase signals are summed using a 0° splitter/combiner.

up to about 100 MHz. Beyond 100 MHz, the performance of the phase shifter suffers, as the criterion $f \ll 1/(2\pi RC(V))$ is violated. Substitution of a lower-capacitance varactor diode in the phase shifter allows operation into the lower UHF band, at the expense of low-frequency performance. To test this, we constructed a second prototype circuit, substituting the lower-capacitance SMV1413-079LF varactor diode [58] in place of the SMV1801-079LF. We verified the performance of this prototype using the same direct summing method (Figure. 5.24), again achieving a signal cancellation on the order of 100 dB over a 1 MHz bandwidth. Performance was excellent up to 500 MHz — the upper frequency limit for the splitter/combiner modules used in our setup.

We emphasize that the major advantage of the broadband performance of our circuit is that it allows the researcher to measure high-order resonances of micro and nano-mechanical resonators without modifying the experimental apparatus. Simply by adjusting bias voltages, the frequency of optimal

balance and maximum background signal cancellation is easily translated, and may be scanned across any band of interest in order to fully characterize all resonances of a given device.

5.7 Application Examples

The balancing circuit, as described, is an extraordinarily versatile piece of instrumentation. It may be directly integrated into a wide variety of bridge measurement schemes, including the three-port transmission bridge [27,48], the two-port reflection bridge, the one-port reflection bridge [4], and the piezoresistive bridge (with and without downmixing) [5], among others. In all cases, the circuit replaces many (often difficult) physical balance adjustments with comparatively straightforward electronic tuning. The result is that the intrinsic balance of the experimental apparatus becomes less critical, allowing the use of low-cost, off-the-shelf modules, cables that are not precisely electrically matched, and less mechanically precise test fixtures without seriously impacting the quality of measurements. In this section, we discuss a handful of applications where this circuit works particularly well.

5.7.1 Three-Port Magnetomotive Bridge

Figure. 5.26 illustrates how our balancing circuit can be integrated into a 3-port magnetomotive balanced bridge measurement of the sort introduced in Figure. 5.1 and demonstrated in [27] and [48]. Attenuators are used as a broadband substitute for the isolators described in [48]. These attenuators serve to increase isolation as well as to ensure that the balancing circuit sees a well-behaved 50 Ω load at all times. Using this configuration, we measured the response of a 9.5 MHz doubly-clamped-beam resonator in a 1 T magnetic field (see Figure. 5.27). By tuning the balancing circuit for maximum off-resonance cancellation, we obtained an excellent signal-to-background ratio of about 25 dB. This large signal-to-background ratio allows the resonant frequency and quality factor to be read directly off the frequency-domain

121
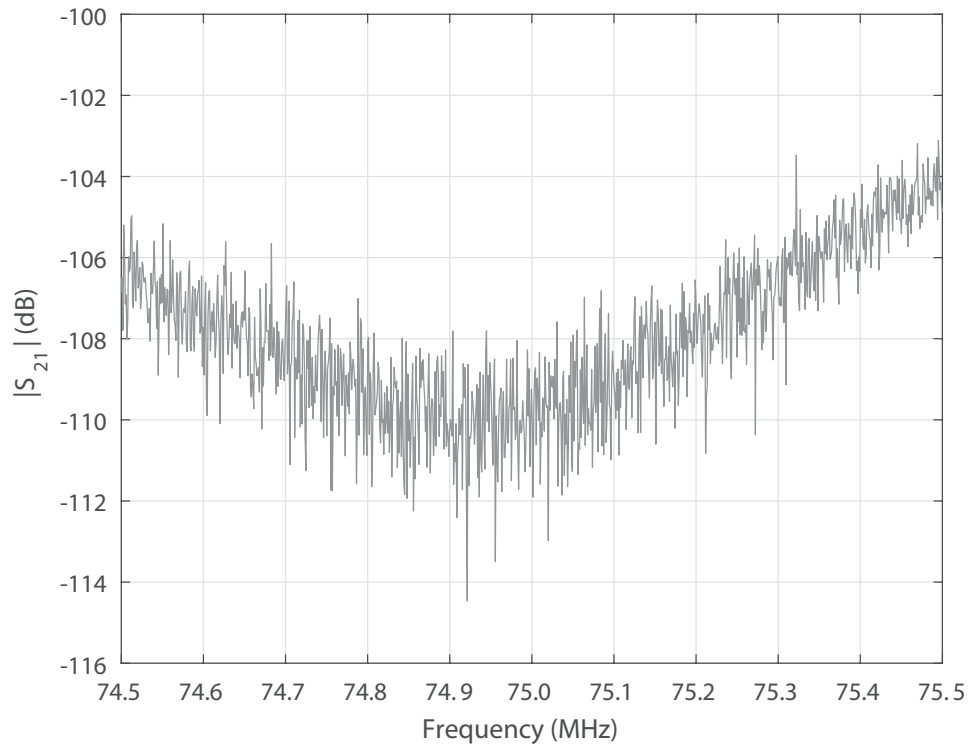
Figure 5.25: Typical signal cancellation after tuning, over a 1 MHz band-width — Each attenuator in the balancing circuit contributes about 7 dB of loss; as a result, actual signal cancellation is about 100 dB.

transmission plot, greatly simplifying resonator characterization.

5.7.2 One- and Two-Port Reflective Bridge

Our balancing circuit is particularly well-suited to improving reflection-mode measurements of resonators in a variety of configurations. One such configuration, based on the measurement scheme in [59] and [4], is illustrated in Figure. 5.28. A balanced, 2-port reflective bridge is fabricated on-chip, and is driven by two directional couplers. Off-resonance, the reflections from the bridge elements are equal and opposite (due to anti-phase excitation), and cancel out. The resonance of a single bridge element changes the amplitude and phase of the reflected signal in one branch, leading to imperfect cancellation which is then amplified and detected.

Here, the balancing circuit substitutes the adjustable reference resistor and cable from the setup described in [4]. Such adjustable components are difficult to realize with sufficient precision, even at frequencies as low as 1 MHz. At higher frequencies, fabricating perfectly matched cables and test fixtures becomes significantly more challenging, as small mismatches in electrical length translate to ever increasing phase unbalance. It is in this higher frequency regime that the balancing circuit really shines. Where a one-port characterization is required, the reference leg of the bridge may be substituted with a reference resistor. The resulting unbalance may be compensated with the balancing circuit so long as it is kept small.

5.7.3 Piezoresistive Bridge

The application of our balancing circuit is by no means limited to magnetomotive resonators. Figure. 5.29 demonstrates the potential application of our circuit to balancing the piezoresistive bridge described in [5]. In this measurement configuration, two RF generators, offset slightly in frequency, drive an electronic bridge, one leg of which is composed of a piezoresistor mechanically coupled to a resonator. The signal due to mechanical resonance at the drive frequency and the AC bias signal are downmixed by the piezoresistor, generating a low-frequency signal that is easy to measure in a
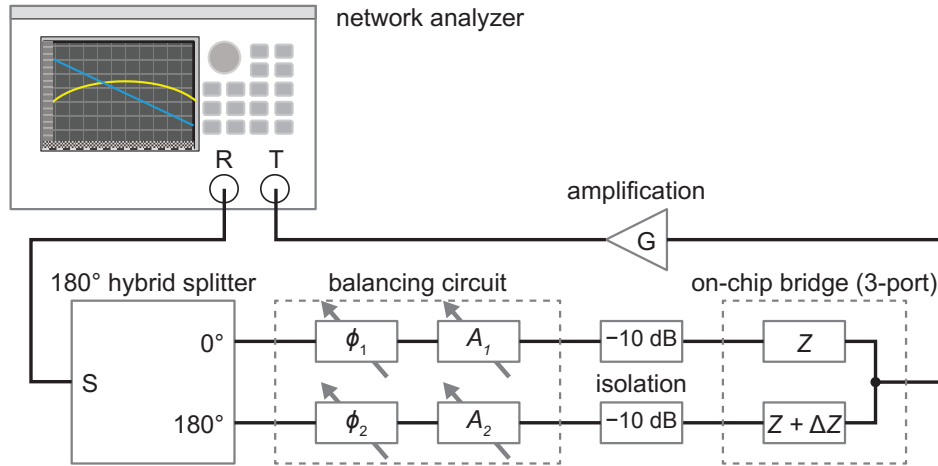
Figure 5.26: Experimental configuration for measuring magnetomotively actuated and detected MEMS resonators using the balanced configuration — Attenuators are placed in-line with the balancing circuit to increase isolation and improve matching.

high-impedance environment [5]. Our circuit, inserted in-line after the 180° splitter, serves to null the AC bias signal at the bridge point. The improved bias signal cancellation allows this technique to be extended to measurement of lower-frequency resonators where the presence of the drive signal could overload the detection circuitry. The delicately-nulled background also eases design constraints on the low-pass filter, which, at lower frequencies, would have to be of very high order to be able to reject the residual bias signal due to intrinsic unbalance in the bridge.

5.8   Conclusion

Variations on balanced measurement techniques represent the state-of-the-art for electrical readout of high-frequency MEMS and NEMS resonators. Though traditionally challenging to implement in practice, our balancing circuit makes the process of background signal nulling easy. By providing four points of adjustment, the balancing circuit loosens design requirements for the rest of the test and measurement setup; *i.e.* cables need not be per-
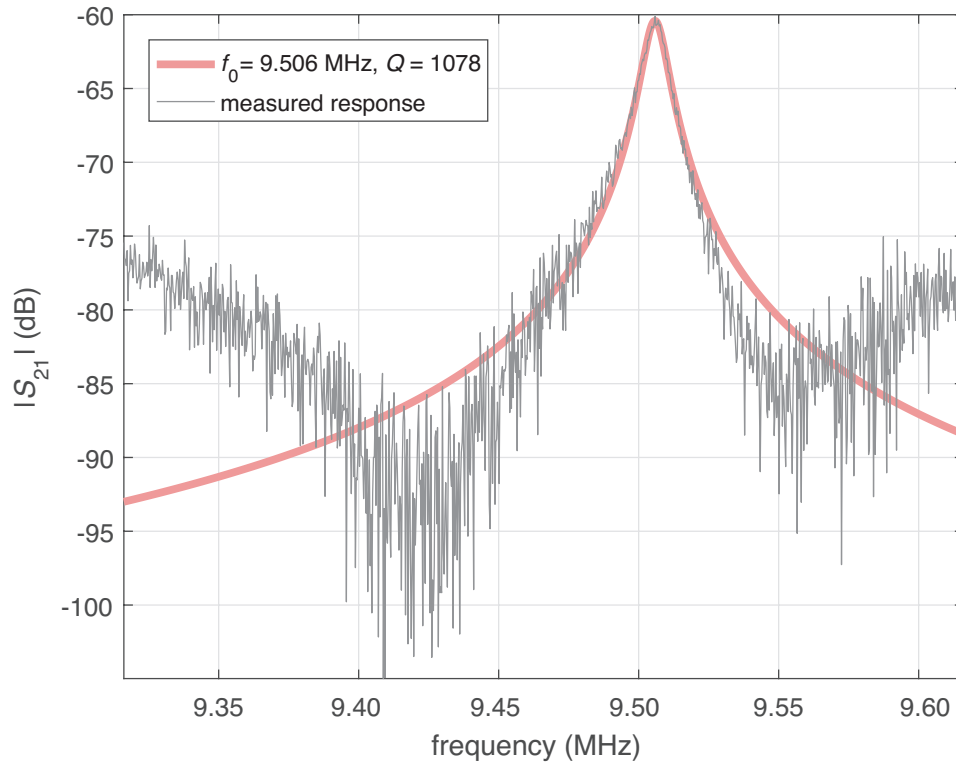
Figure 5.27: Response of a magnetomotive doubly-clamped-beam resonator, measured using the balanced technique — The signal balancing circuit allows us to achieve a signal-to-background ratio > 20 dB. (Compare with a typical signal to background ratio of < 1 dB without tuning). Overlay: Fitted Lorentzian response. The high signal-to-background ratio allows curve fitting to be done with confidence.
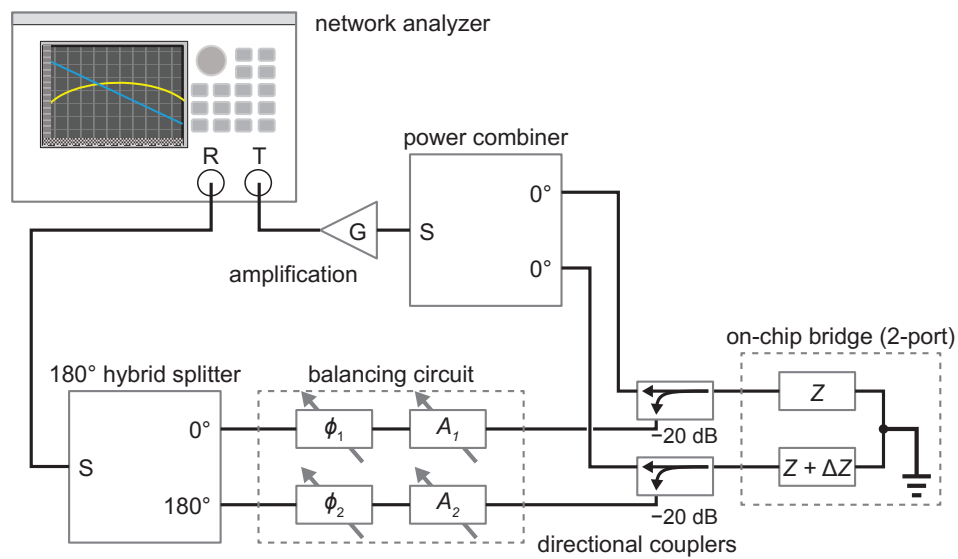
Figure 5.28: Balanced two-port reflective bridge measurement scheme, based on the scheme described in [4]. For the one-port technique, replace one leg of the bridge with a reference resistor to ground. The balancing circuit compensates for the unpredictable and uncontrollable unbalance due to any and all components in the signal path.
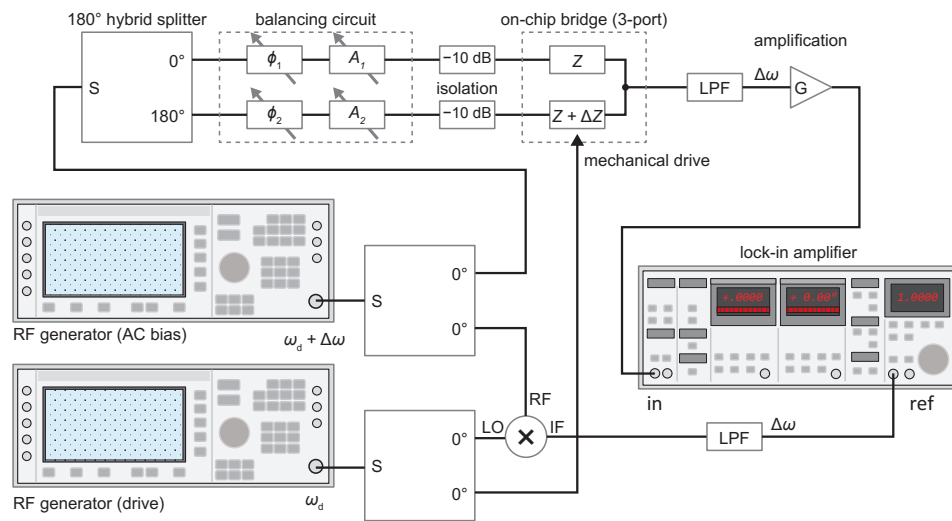
Figure 5.29: Balanced piezoresistive actuation and detection, using the scheme described in [5]. The balancing circuit serves to null the background due to unbalance in the AC bias signal path. Adjustable balance compensation eases design of the rest of the experimental apparatus by rendering the individual performance of each component less critical.

fectly matched, and readily available, off-the-shelf components may be used to construct the test apparatus without worry of introducing uncorrectable unbalance in the system. Furthermore, the broadband performance of our device allows both fundamental and higher-order resonances to be characterized with the same experimental setup, greatly simplifying measurement.

With demonstrated performance to 100 MHz (or to beyond 500 MHz with the aforementioned varactor substitution), the balancing circuit is an extremely versatile component. Herein, we have described a handful of illustrative test and measurement applications. The fact that our circuit may be seamlessly integrated with just about any balanced measurement technique indicates that there exist a great many more. Our intent is that these examples serve both as inspiration, as well as evidence that, with this balancing circuit in hand, balanced measurement techniques are as accessible as they are powerful.

Chapter 6

Initial Measurements

With all of the tools and techniques from the previous chapters in hand, we take some preliminary measurements of some devices, with an eye towards verifying correct operation of the system. We begin with a brief overview of our instrumentation setup, then present initial measurements of both U-cantilever and DCB resonators. We evaluate the effect of the ambient gas pressure on the quality factor of resonance, demonstrating that our system can operate at pressures low enough to render air damping negligible. A discussion of dissipation mechanisms follows. We briefly discuss some initial evidence of non-linear behavior in our devices when driven at high power. Finally, we demonstrate the exquisite tunability of our balanced bridge with some measurements of our RF MEMS resonators operating at ambient atmospheric pressure. The chapter ends with some ideas for future experiments.

6.1 Instrumentation and Experimental Method

Fabricated devices were first imaged using the Zeiss Sigma FESEM in the NanoFab. SEM imaging immediately reveals many potential fabrication issues, such as stictioning, beam buckling, or other catastrophic device failure (potentially due to mishandling). Furthermore, SEM imaging provides a means of measuring the actual (as-fabricated) device dimensions, including

beam widths, device lengths, and the actual size of the BOE undercut.

The devices were then subject to pass-fail testing using a multimeter. Using the test fixture, all contact pads were tested for isolation with respect to ground. Any devices with a short to ground were excluded from later testing. This first test was followed by measuring the resistance between the driving terminals and the common terminal of each device. Failed devices presented as an open circuit, while potentially working devices indicated a resistance on the order of 100 Ω.

With data in hand from both SEM imaging and preliminary electrical testing, potential working devices were then measured using our apparatus, with the anti-phase drive ports connected to the balancing circuit and the bridge port signal amplified and detected by the network analyzer.

For the purposes of measuring our devices, we apply the three-port magnetomotive bridge technique, as outlined in section 5.7.1 and Figure. 5.26. Figure. 4.1 gives an overview of the system configuration.

An RF network analyzer (Keysight E5061B) generates a drive signal, which is passed through an RF coaxial feedthrough into our vacuum system. The drive signal passes through a 2-way 180° hybrid splitter (Mini-Circuits ZFSCJ-2-1-S+), generating two roughly anti-phase signals. These signals are passed through our balancing circuit, which allows fine-tuning of the measurement bridge. Each branch of the balancing circuit is followed by a 10 dB attenuator (Mini-Circuits VAT-10+), which serves to increase isolation between the balancing circuit and the test fixture.

Two coaxial cables carry the drive signal from the balancing circuit to the test fixture, and a third cable carries the bridge-point response signal to the RF feedthrough, where it passes out of the vacuum system. This response signal passes through a low-noise RF amplifier (Mini-Circuits ZFL-500LN+) which is connected in-line with the network analyzer's receiver. The network analyzer is configured to measure the forward transmission coefficient (labeled S21), which represents the ratio of power incident at the analyzer's receiver to that generated by the analyzer's signal source.

The network analyzer was interfaced with a PC running MATLAB using the instrumentation control toolbox, greatly simplifying data capture. The

system pressure monitor (MKS PR 4000) was interfaced via RS-232 to allow simultaneous capture of pressure data. In the future, additional equipment may be interfaced with the PC in order to conduct more complex experiments.

6.2   Measurements on DCB Resonators

Doubly-clamped beam resonators were fabricated using the process outlined in chapter 3. These devices were designed for a nominal beam width of 500 nm, and were metallized with 6 nm of Ti followed by 30 nm of Al. The BOE process resulted in an undercut of about 500 nm. Some representative SEM images of the fabricated devices are included as Figure. 6.1.

Response curves were captured for the working devices. Resonant frequencies and quality factors were extracted by curve-fitting a Lorentzian in the neighbourhood of the response peak. The measured resonant frequencies are plotted vs. length in Figure. 6.2 and Figure. 6.3. The data are also included below, in Table. 6.1.

Notably, one device (a 5 μm DCB) was measured two months before the other devices. This happened as the test fixture was, at that time, still being constructed. After measuring this device, the chip containing the DCB resonators was imaged under SEM, and then stored until further measurements could be made. The same device, measured later, yielded both lower

Nominal Length (μm)	$f_{\textbf{res,1}}$ (MHz)	Q_1	$f_{\textbf{res,2}}$ (MHz)	Q_2
3	80.455	363	–	–
3.5	63.149	567	62.550	446
5	34.247	446	36.264	356
5 (*)	35.547	642	37.157	829
5.5	22.245	473	22.504	411

Table 6.1: Resonant frequency $f_{\text{res},(1,2)}$ and quality factor $Q_{(1,2)}$ for working DCB resonators. (*): This data was collected two months prior to the rest of the dataset. The device measured is identical to that measured in the row above.
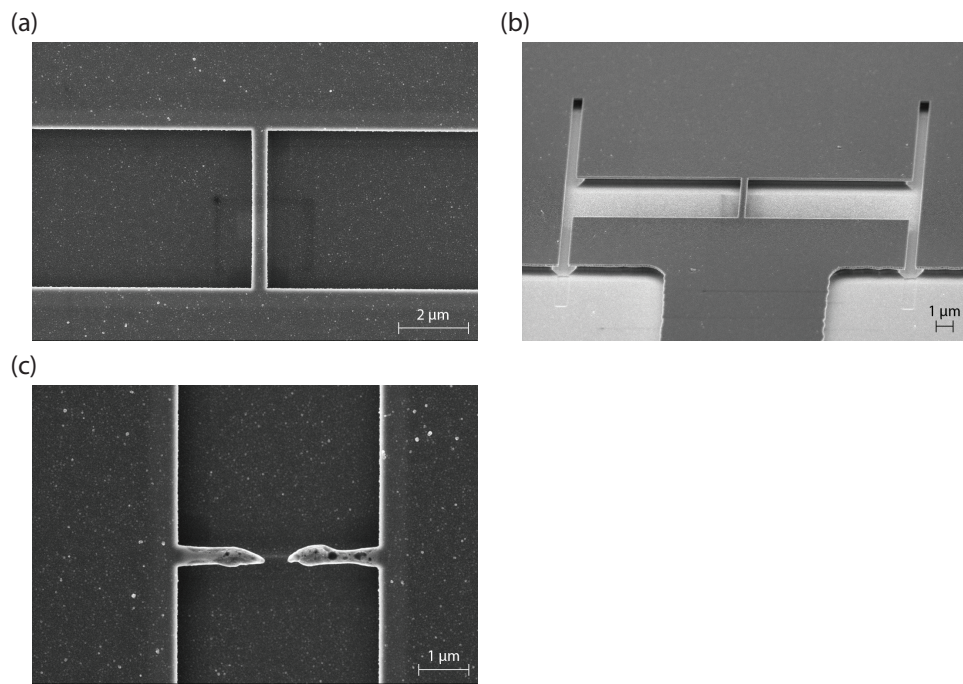
Figure 6.1: Representative SEM images from the DCB chip. (a) Top view and (b) tilted view of a nominally 6 μm long and 500 nm wide DCB resonator. (c) Image of a failed device, which may have snapped during deposition.

resonant frequencies and lower quality factors. The lower measured resonant frequencies suggest adsorbed material is at least partially responsible for this phenomenon. The lowering of quality factor might be attributable to thin-film aging effects, contamination of the devices during storage, or contamination from SEM imaging. It is likely that the quality factors and resonant frequencies of the other devices were affected in a similar way. In the future, devices should be electrically characterized immediately after fabrication to eliminate these potential issues.

As a first check that our devices are behaving as expected, we compare a plot of resonant frequency vs. device length to what we would expect for a stress-free DCB resonator. For these purposes, we employ the model of section 2.5. Additionally, we apply the correction of section 2.6 to take into account the mass-loading and stiffness of the metallization layer. For the purposes of modelling, we assume a Si device layer thickness of 145 nm, metallized with 6 nm thick Ti and 30nm thick Al layers, for which bulk properties have been assumed. Devices are assumed to have their nominal length L. This model is plotted as the blue curve in Figure. 6.2, alongside measured data.

As seen in Figure. 6.2, the basic multilayer model does a terrible job at predicting the resonant frequency of our devices as-is. In an attempt to correct the model, we add to the length L of our resonators a quantity ΔL, which represents an effective additional length due to the BOE undercut at the clamping points. With a BOE undercut of 500 nm, the worst-case (largest possible magnitude) ΔL is 2×500 nm $= 1$ μm. (In reality, the effective ΔL will be somewhere in-between 0 and $2 \times L_{\text{undercut}}$, where L_{undercut} is the length of the undercut due to the BOE process.) The same multi-layer model, plotted using $L+\Delta L$ as the resonator length shows remarkable agreement with the measurements for the smaller resonators, but over-estimates the resonant frequency of the longest resonator by a large margin. This over-estimation may be due to the presence of compressive stress in the DCBs, which, as per eqn. (2.70) would tend to depress the resonant frequency of the longest beams. Of course, more data would be required to establish this claim with certainty.

133
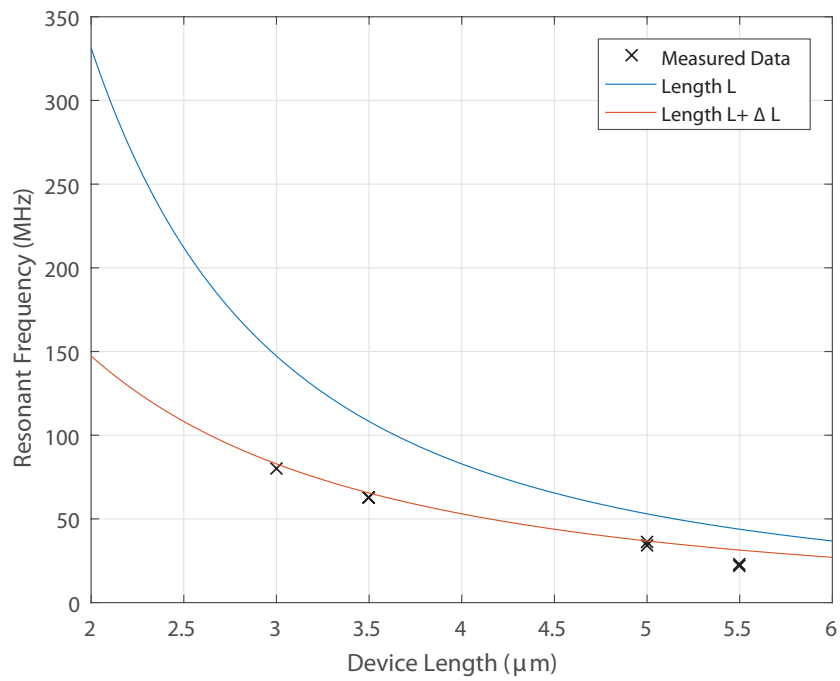
Figure 6.2: Measured DCB resonant frequencies vs. length, compared with theoretical estimates for a stress-free beam of length L (the designed length) and ΔL (the designed length, plus undercut).

One key issue with the above model is that we have neglected the fact that thin-film materials often exhibit very different mechanical properties from bulk materials. Without extensive thin-film characterization, we cannot be sure how much of the error of our model is due to uncertainty in thin-film material properties. An alternative method towards evaluating our model for the DCB resonator is to attempt to fit a mathematical curve with the theoretically expected L dependence to our data. If we assume the Euler buckling stress is a function of L, while the resonant frequency ω_0 is a function of $L + \Delta L$, we obtain:

$$f_{\text{res}}(L) = \left(\frac{4.73}{L + \Delta L} \right)^2 \sqrt{\frac{EI}{\lambda'}} \sqrt{1 + \frac{3L^2 \sigma}{\pi^2 E H^2}} \tag{6.1}$$

Replacing device parameters with fitting parameters, we obtain:

$$f_{\text{res}}(L) = \frac{1}{x_1} \frac{\sqrt{1 + x_2 L^2}}{(L + x_3)^2} \tag{6.2}$$

where $x = [x_1, x_2, x_3]$ is chosen to minimize the least-squares residual between the measured data and the function $f_{\text{res}}(L)$. The fit of this numerical model is plotted alongside measured data in Figure. 6.3. The close fit between the model and the measured data is reassuring; however, more data would be required to confirm the form of $f_{\text{res}}(L)$.

6.3   Measurements on U-Cantilever Resonators

U-cantilever resonators were fabricated using the process of chapter 3. As with the DCB resonators, devices were designed for a nominal beam width of 500 nm, and were metallized with 6 nm of Ti, followed by 30 nm of Al. The width of the cross-beam was nominally 2 μm for all of the patterned devices. Some representative SEM images of the fabricated devices are included as Figure. 6.4.

Unfortunately, only two devices from this chip ultimately functioned, in part due to a scratch imparted to the chip surface during fabrication. One of these devices only created a measurable response when excited in the
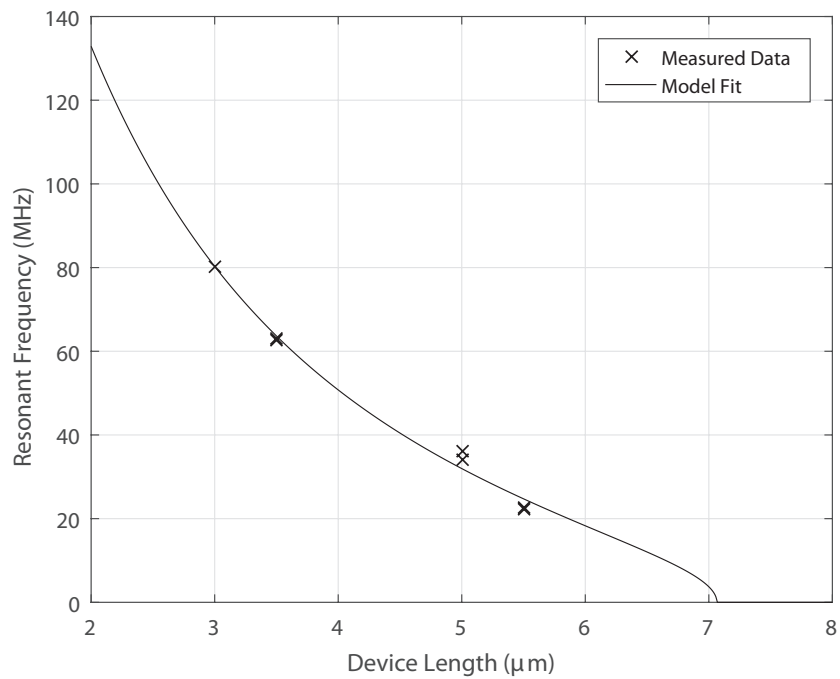
Figure 6.3: Fit of numerical model including residual stress effects and "effective" undercut to experimental data. The model exhibits good agreement with the measured data, but more measurements are required to confirm the validity of this approach.
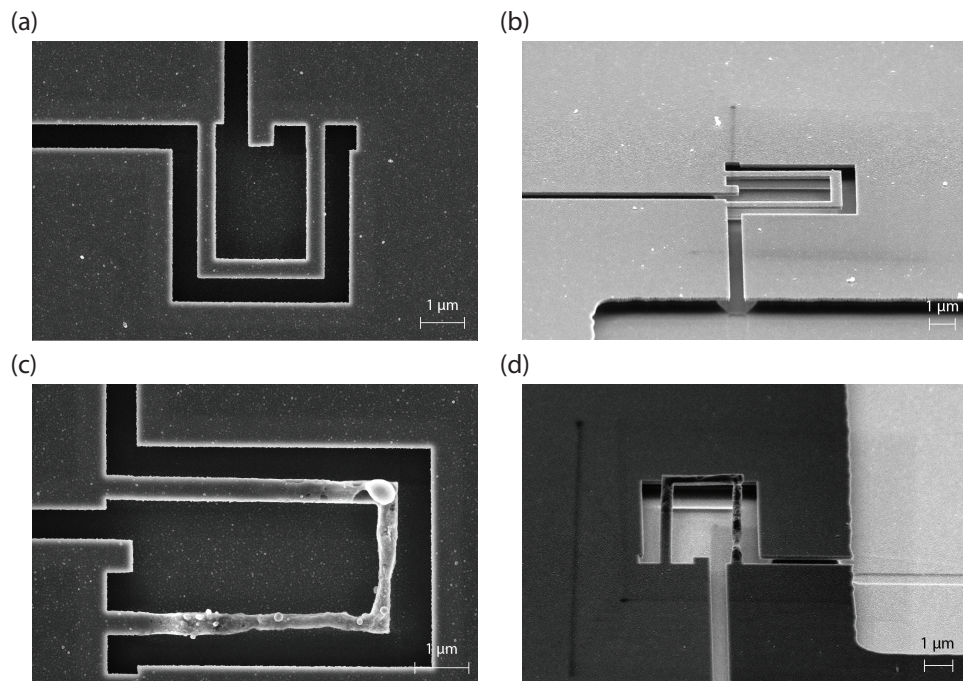
Figure 6.4: Representative SEM images from the U-cantilever chip. (a) Top view of a nominally 3 μm long resonator. (b) Tilted view of a nominally 4 μm long resonator. (c) Top view and (d) tilted view of a failed device, which likely snapped during deposition.

torsional mode. The measured data are recorded below, in Table. 6.2.

As there were few working devices, it is not possible to verify the applicability of our model for calculating U-cantilever resonant frequency as we did for the DCB resonators in the previous section. We can, however, compute the resonant frequency of the 3 μm long cantilever using the multi-span method of section 2.4.2, and compare the result to our measured value.

For the sake of calculation, we assume a device layer thickness of 145 nm, a 6 nm Ti film, and a 30 nm Al film. The length of the resonator is approximated as $L' \approx L + \Delta L$ where $\Delta L = 500$ nm, the size of the BOE undercut. We use the density-only correction of section 2.6, and assume all materials have their bulk properties. Performing the calculation (see appendix A for details), we obtain $f_{\text{res,calc}} = 10.058$ MHz, an error of only 4% from the measured value. Though this result is reassuring, more measurements would be required to verify the applicability of our model to these devices.

6.4   Evaluation of Loss in Measured Resonators

6.4.1   Air Damping

At pressures above a few Torr, air damping is known to create significant losses in resonating micromechanical structures. To investigate the effect of air damping on the quality factor of resonance of our devices, we measured response curves for a 4 μm long U-cantilever resonator operating in the torsional mode while varying the ambient pressure. The pressure was varied by leaking in small quantities of nitrogen through the system vent valve,

Nominal Length (μm)	$f_{\text{res,1}}$ (MHz)	Q_1	$f_{\text{res,2}}$ (MHz)	Q_2
3	9.661	643	9.689	778
3 (*)	24.668	498	–	–
4 (*)	18.397	901	–	–

Table 6.2: Resonant frequency $f_{\text{res,(1,2)}}$ and quality factor $Q_{(1,2)}$ for working U-cantilever resonators. (*): Torsional mode.

closing the valve, and then allowing the pressure to stabilize before capturing data. Response curves were captured for 29 different ambient pressures, and the quality factor for each response was estimated by curve-fitting a Lorentzian function to the resonance peak (Figure. 6.5) The resulting quality factor vs. pressure data are presented in Figure. 6.6.

From Figure. 6.6, we see that for pressures above 1 Torr, the quality factor begins to decrease, reaching a minimum of about 57 at about 430 mTorr. The consistent downward trend of Q vs. pressure above 1 Torr suggests that air damping is the dominant loss mechanism in this pressure regime. Conversely, below 1 Torr, the quality factor remains more-or-less constant at around 1100, indicating that air damping is likely not dominant in this pressure regime, and suggesting that other loss mechanisms, independent of ambient pressure, are dissipating energy in our devices. Potential culprits are discussed in section 6.4.2.

The precise mechanism behind air damping depends on the pressure regime, device dimensions, frequency of operation, and more. As such, the phenomena at play may be difficult to identify. At high gas pressures, viscous air damping may dominate, while molecular flow dynamics can explain damping phenomena at lower gas pressures. [60] Further complicating analysis is the presence of squeeze-film damping – damping due to a thin layer of gas between the resonator and the substrate – which can lead to additional losses [60–62]. An excellent review of squeeze-film damping dynamics can be found in [61].

6.4.2 Other Loss Mechanisms

There are a great number of phenomena which may contribute to mechanical loss in micromechanical resonators. These phenomena include thermoelastic damping, clamping losses, as well as damping due to defects in the device materials. [63–66]. In this section, we review these dissipative processes, and consider their potential impact on the final measured quality factors of our devices.
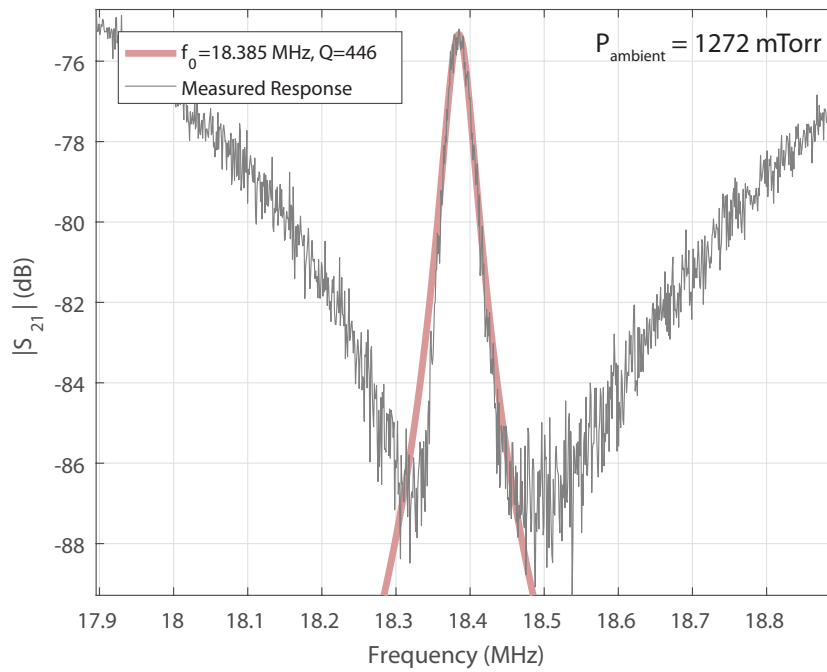
Figure 6.5: Sample result from curve-fitting procedure, at an ambient pressure of 1272 mTorr. The curve fit is restricted to the neighbourhood of the peak, as the response is expected to deviate from an ideal lorentzian as it falls towards the background signal.
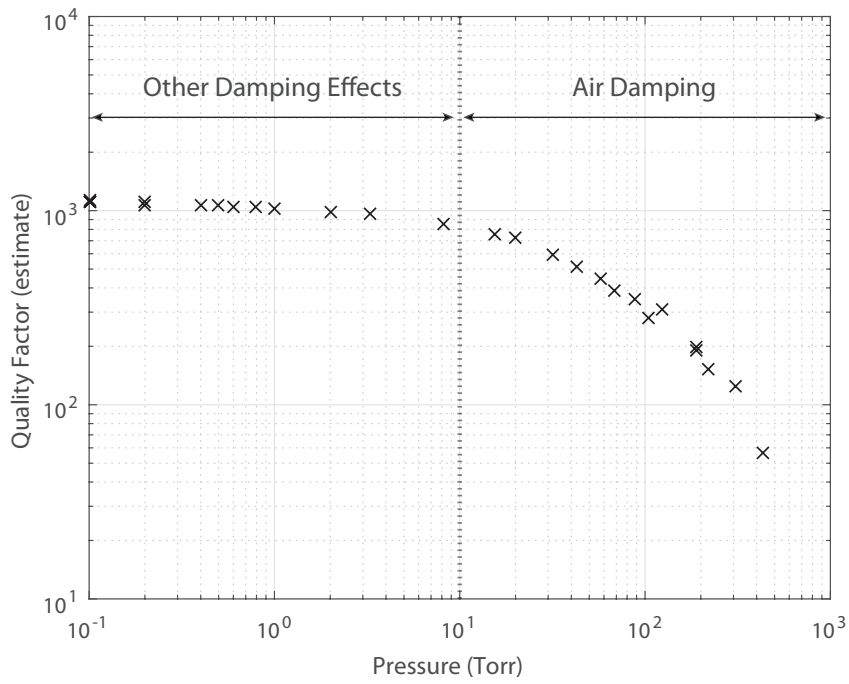
Figure 6.6: Estimated quality factor vs. pressure for a 4 μm long U-cantielver resonator operating in the torsional mode. The quality factor levels off for pressures lower than about 1 Torr, suggesting that other damping mechanisms are dominant in this pressure regime.

Thermoelastic Damping

Thermoelastic damping (TED) plays a role in estabishing an upper bound on device performance, as this phenomenon is present in all resonators. This form of damping occurs due to coupling between material strain and local temperature. In a micromechanical resonator, periodic expansion and contraction of the beam creates time-varying temperature fluctuations throughout the beam. The irreversible flow of heat between these regions leads to mechanical loss. [67] This process is illustrated in Figure. 6.7.

In particular, we expect TED to be more significant in metallized resonators than in simple bulk Si devices. The thin metallization layer almost certainly has a different coefficient of thermal expansion than the Si device layer. Under periodic strain, as occurs during resonance, this discontinuity in the thermal expansion coefficient leads to a step discontinuity in temperature, leading to a significant irreversible flow of heat and, depending on device geometry and the material stack-up, significant mechanical losses.

To estimate the contribution of TED in limiting the performance of our devices, we calculated the quality factor due to TED alone vs. frequency for both a uniform Si beam with a thickness of 145 nm, and for an identical beam coated with a 35 nm thin film of Al. The results are presented in Figure. 6.8. For the purposes of modelling, bulk material properties were assumed. The method used to compute the quality factor for the uniform Si beam is from [68]. For the case of the bilayer Si/Al beam, we used the
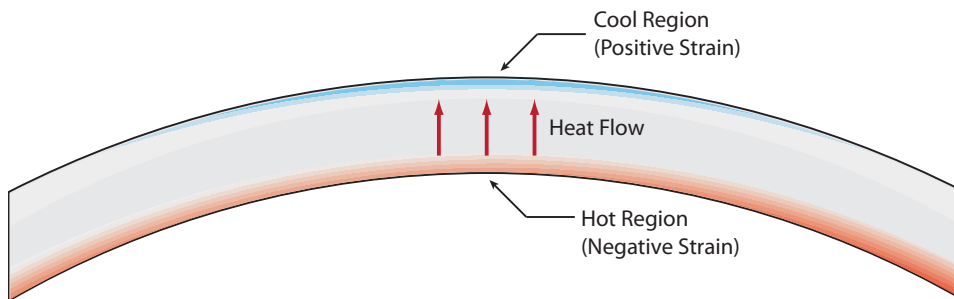
Figure 6.7: Mechanism of thermoelastic damping. Irreversible heat flow between periodically hot and cold regions in a vibrating beam leads to loss.

technique from [64]. Implementation of these techniques (non-trivial in the case of the bilayer beam) are presented in appendix B.

From Figure. 6.8, we see that the presence of the thin-film coating serves to reduce the quality factor of our devices by a full order of magnitude, as compared with the quality factor of the uncoated beam. That said, the calculated quality factor is a full two orders of magnitude higher than the measured Q for our resonators, indicating that TED is unlikely to be the most important dissipative process in our devices. TED may become limiting for smaller devices operating at higher frequencies.

Clamping Loss

Clamping losses establish yet another fundamental limit on resonator performance. This dissipative process occurs due to elastic waves which radiate into the supports of the device, and is much less significant for torsional resonators than for those which undergo transverse vibration. [69]

In an attempt to evaluate the magnitude of this effect in our devices, we will assume the worst-case scenario of transverse vibration in a 4 μm long, 500 nm wide, and 145 nm thick resonator. From [69], Q is given approximately by:

$$Q \approx \frac{3.9}{\pi^4 C_0} \frac{L^5}{W t^4} \left(\frac{3\pi}{2k_0 L} \right)^4 \tag{6.3}$$

where:

$$k_0 = 0.60\pi/L$$
$$C_0 = \tanh^2 \frac{k_0 L}{2}$$

Substituting our device parameters gives $Q \approx 1 \times 10^7$, which is two orders of magnitude higher than that computed due to TED alone, suggesting that clamping losses for our devices should not be significant.

Of note, however, is that the above formula assumes that the transition between the resonator and the support structure is abrupt. This is not necessarily true for our devices, due to the significant BOE undercut. A future
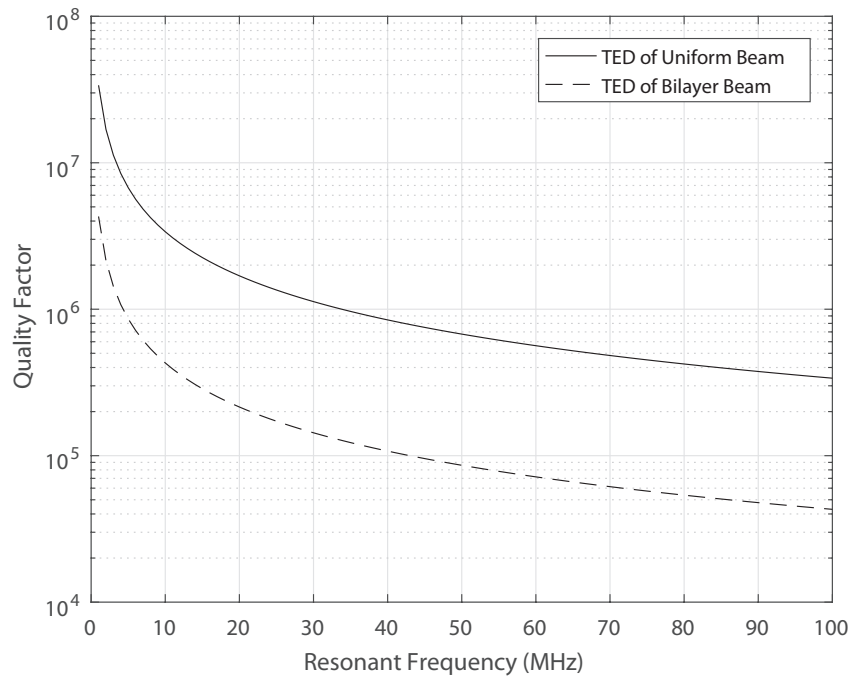
Figure 6.8: Quality factor for a 145 nm thick Si resonator due only to thermoelastic damping (solid line), plotted alongside the quality factor due to thermoelastic damping in the same device when coated with a 35 nm thin film of Al (dashed line). The order of magnitude difference in quality factor is largely due to increased irreversible heat flow across the interface between the film and the device. The dashed line represents a theoretical upper-bound on the quality factor of our devices.

experiment might be to reduce the amount of BOE undercut and evaluate the effect on Q. Furthermore, modifying the geometry of the clamping point(s), as done in [12], may provide additional insight into the significance of this loss mechanism.

Defect-Related Loss

A number of defect-related loss mechanisms exist. Thin film dislocations [65,66], grain boundaries, and diffusion of point defects [63] can all contribute to dissipation. Predictive modelling of these phenomena is difficult, as they may depend strongly on film microstructure and composition, all of which may vary when materials are deposited in different conditions.

One experiment to study the effect of defect-related losses in our devices would be to anneal our chips in an attempt to form a more crystalline metallization layer. The effect on Q, if any, may provide insight into the degree of loss attributable to defects in the thin-film coatings.

6.5   Drive Power and Onset of Non-Linearity

Our assumption of linear elastic behavior for the materials used to fabricate our resonators begins to break down for large deflections. At large drive powers, our devices begin to exhibit non-linear behavior. To investigate the onset of non-linearity, a 5.5 μm long DCB resonator was driven with excitation signals in the range from -20 dBm to -10 dBm at 1 dBm increments. Response curves were captured for each drive power. Some illustrative response signals are presented in Figure. 6.9.

As seen in Figure. 6.9, as the drive power is increased, the resonator response curves become skewed to the right and, for the highest drive power, sharply drop off. Examples of such behavior in MEMS resonators abound in the literature. [70–72] A review of nonlinear dynamics in NEMS can be found in [73].

A high level explanation of the frequency jump phenomenon follows from studying the dynamics of a damped oscillator in which the restoring force
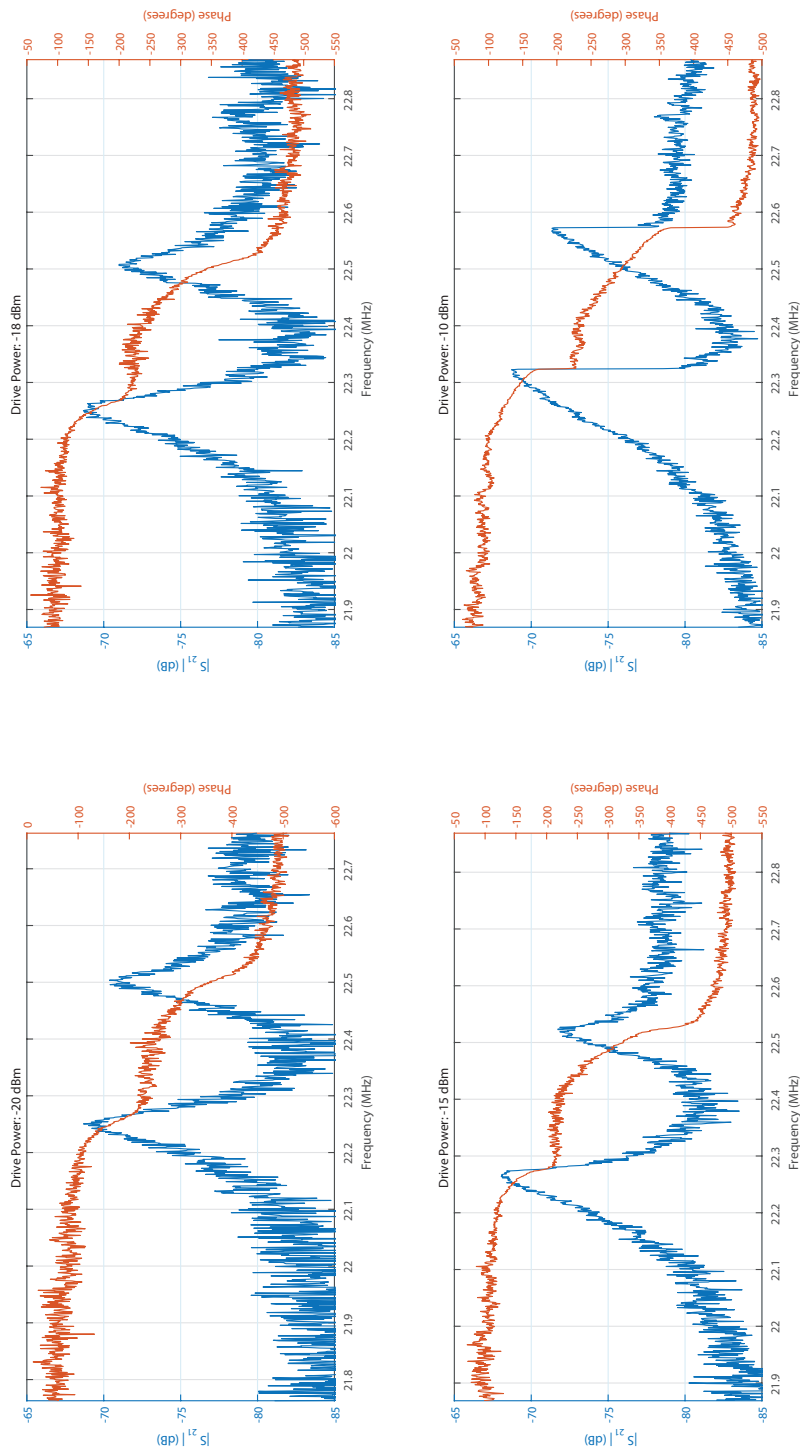
Figure 6.9: Response of a 5.5 μm long DCB resonator as drive power is increased from -20 dBm to -10 dBm. Note that drive power is measured at the R port of the network analyzer. The drive power at the resonators is expected to be about 17 dB lower than that measured at the R port, due to attenuation in the balancing circuit and the 10 dB attenuators. Skewing of the resonance peak to the right suggests a "hardening"-type nonlinearity is present in the system.

exhibits a cubic departure from Hooke's law. The dynamics of a forced oscillator are described by the equation: [70]

$$m\frac{d^2x}{dt^2} + c\frac{dx}{dt} - F_{\mathrm{r}}(x) = F_{\mathrm{drive}}(x, t) \tag{6.4}$$

In the case of a non-linear restoring force (due to the breakdown of the Euler-Bernoulli beam equation for large deflections), we have $F_{\mathrm{r}} = -k_1 x - k_3 x^3$. Furthermore, assuming a harmonic driving force, we have $F_{\mathrm{drive}} = F_0 \cos(\omega t)$. Substituting and simplifying, we obtain: [70]

$$m\frac{d^2x}{dt^2} + c\frac{dx}{dt} + k_1 x + k_3 x^3 = F\cos(\omega t) \tag{6.5}$$

This is an instance of a Duffing equation, which has been exhaustively characterized in the literature. Solutions to the Duffing equation reproduce the jumps in frequency response seen in our measurements. [74]. In particular, the direction of skew of the frequency response, as well as the location of the jumps, can be related to the device parameters. [74]. Systems that experience a skewing to the right (as in Figure. 6.9) are known as "hardening" systems, and have $k_3 > 0$, meaning that for large deflections, the effective stiffness of the resonator increases. [74] Conversely, systems that skew to the left have $k_3 < 0$ and are known as "softening" systems, as the effective spring constant decreases as the deflection becomes large. [74] Interestingly, the torsional U-cantilever resonator seems to exhibit this "softening" behavior, skewing to the left with increasing drive power, as illustrated in Figure. 6.10. Furthermore, the onset of nonlinearity in the torsional resonator occurs at a much higher drive power than for the DCB resonator (around 2 dBm for the torsional U-cantilever, vs. about -18 dBm for the DCB resonator).

Because these frequency jumps are very sharp, they might be used, in conjunction with extensive characterization and modelling, to increase the mass-sensitivity of our devices. [70]
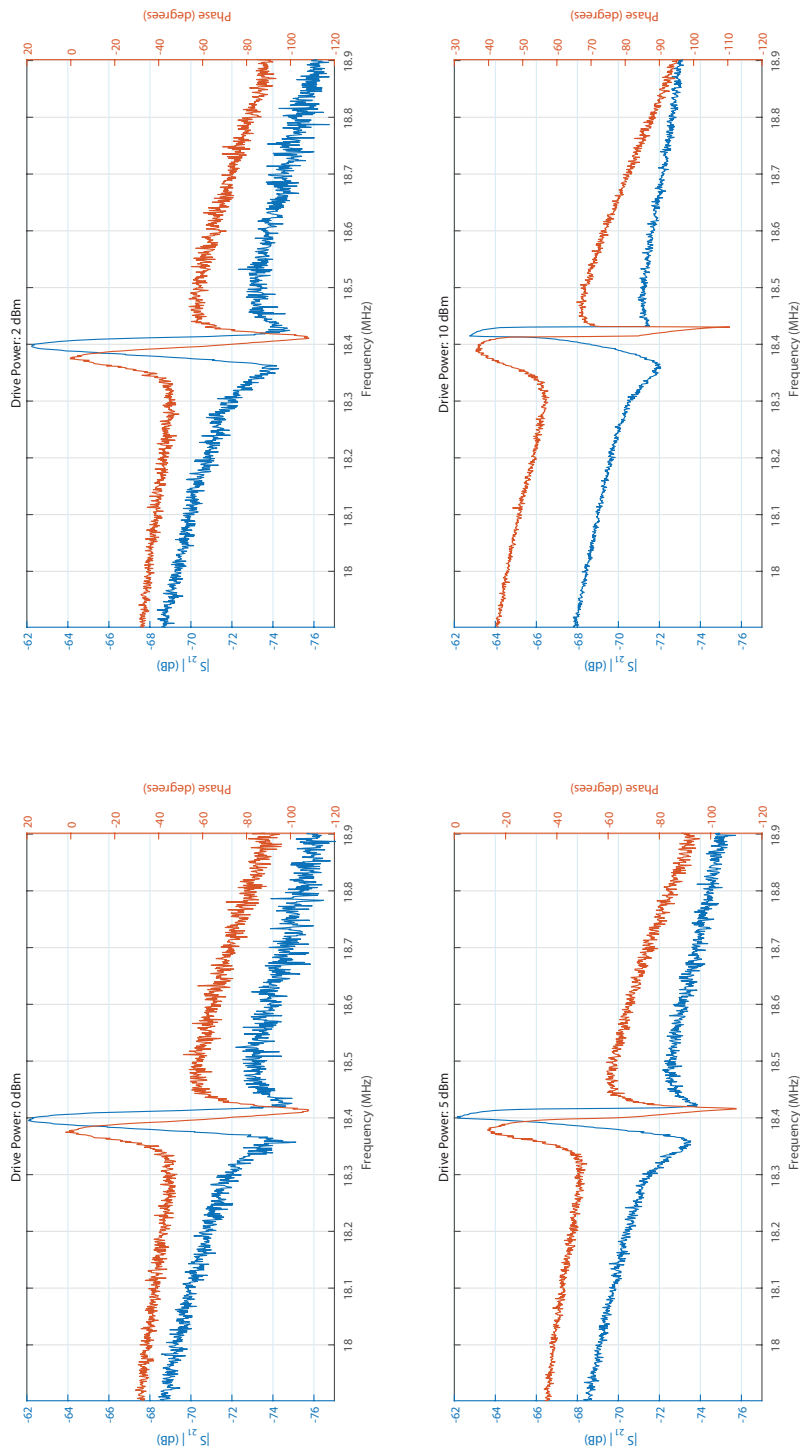
Figure 6.10: Response of a 4 μm long U-cantilever resonator operating in the torsional mode as drive power is increased from 0 dBm to 10 dBm. Note that drive power is measured at the R port of the network analyzer. The drive power at the resonators is expected to be about 17 dB lower than that measured at the R port, due to attenuation in the balancing circuit and the 10 dB attenuators. Skewing of the resonance peak to the left suggests a "softening"-type nonlinearity is present for this device.

6.6 Measurements at Atmospheric Pressure

The exceptional electronic balance achievable with our experimental apparatus allows us to measure the resonance of some of our devices at ambient atmospheric pressure (about 700 Torr). An example of a resonance curve measured under these conditions is given in Figure. 6.11. The response is quite weak, as air damping greatly reduces the quality factor of resonance. Nevertheless, this result shows that sensing in this regime is possible, and the measurement is both repeatable and stable.

6.7 Conclusions and Future Experiments

The most immediate conclusion of this section is that both the resonators and the test system function as intended. Our measurements of resonant frequency, the pressure dependence of quality factor, and the effect of over-driving the resonators are all in-line with theoretical expectations, and are hard evidence that we are, in fact, successfully actuating and detecting resonator motion. That said, there are still a number of challenges to be addressed and questions to be answered as we work towards nanomaterial enhanced gas sensing using this platform.

The most immediate open question is to identify the dissipative process that is limiting the quality factor of our devices. To this end, there are a number of experiments that could be done. First of all, it might be that defects in the thin-film metallization layer lead to significant dissipation. A potential experiment would be to anneal the chips post-metallization in an attempt to create a more crystalline film, and hence increase the quality factor. Furthermore, we could fabricate devices with a thinner metallization layer and evaluate the effect, if any, on Q. Thinner metal layers would provide less volume for defect-related losses to occur, at the expense of the DC resistance of the resonators. Finally, it might be that carbon contamination, integrated into our thin-films during evaporation, is causing significant mechanical loss. In the future, deposition could be carried out using tungsten or boron nitride crucible liners in order to reduce the carbon content of our
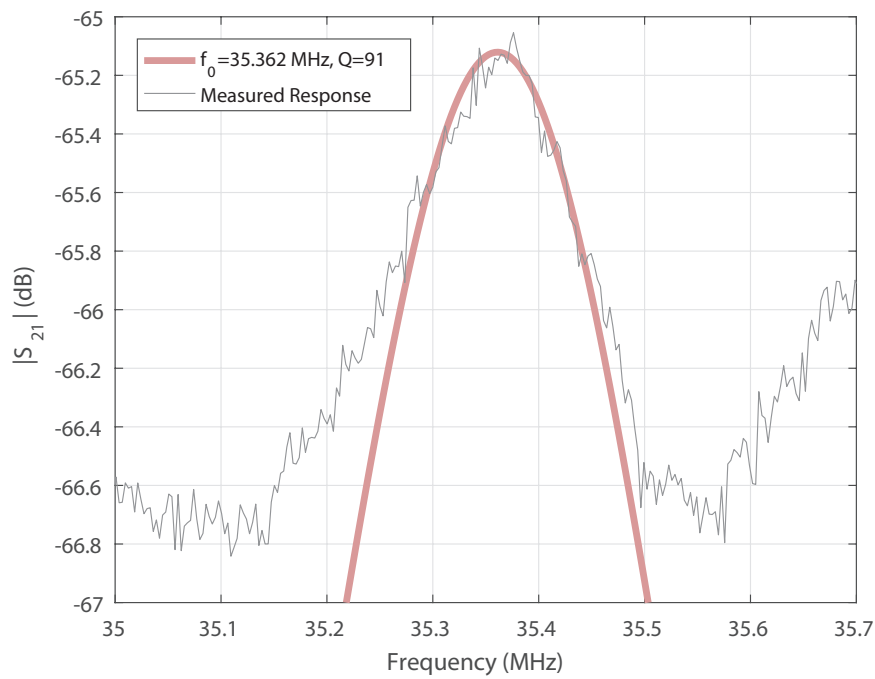
Figure 6.11: Response of a 5 μm long DCB resonator at atmospheric pressure (measured as 683.7 Torr). The low quality factor is a consequence of air damping (see section 6.4.1).

thin films.

There is also the possibility that clamping losses, exaggerated due to the BOE undercut, are limiting Q. Towards resolving this uncertainty, we could fabricate devices with both as small an undercut as possible, and with an exaggerated undercut, and evaluate the effect on Q. There is also the possibility of fabricating devices with purposefully narrowed clamping points, as in [12], to see if changing the clamping conditions has any effect on dissipation.

In order to establish the mass-sensitivity of our devices, a future experiment should measure the Allan deviation (frequency stability) of our devices. This measurement might require some additional instrumentation to be carried out in a meaningful way.

Of note is that the torsional-mode U-cantilever resonators exhibited a combination of (relatively) high quality factor, large signal to background, large dynamic range, and high resonant frequency. Furthermore, theory suggests that the resonant frequency of these structures should be less dependent on residual stresses in the films and devices than the DCB resonators. For these reasons, these devices are likely the best choice for future work into gas sensing with this platform.

After the questions about the quality factor of our devices are resolved, we would like to coat our resonators with GLAD nanostructured films. The enormous surface area enhancement afforded by GLAD films has the potential to make these devices extremely sensitive to gasses of interest. Integration of GLAD films could be followed with chemical modification to make *specific* gas sensors that combine the high surface area of GLAD films with the exquisite mass sensitivity of resonant MEMS structures.

Chapter 7

Conclusions and Future Work

7.1 Concluding Remarks

The objective of this work was to design a platform to be used for experimentation with nanomaterial-funcionalizable resonant MEMS sensors at a low cost. To this end, we designed both a fabrication process flow (chapter 3) and instrumentation (chapters 4 and 5) that, together, make this sort of research possible. Supporting this work are the models developed in chapter 2, which can be used to inform future design, and the initial results of chapter 6, which demonstrate that the devices function as expected. As such, we can claim with confidence that this objective was met.

Perhaps the most immediately useful result of this work is the low-cost balancing circuit of chapter 5, which implements an extremely fine-tunable balanced RF bridge at a very low cost. This simple circuit has the potential to make finely-tunable balanced measurement techniques more accessible to the research community at large. Furthermore, the exquisite tunability of our circuit renders the design of the rest of the instrumentation less critical, enabling researchers to make high-quality, repeatable measurements without the significant financial investment of a precision test fixture, superconducting magnets, and expensive specialty RF modules.

The multi-span beam analysis of the U-cantilever (section 2.4.2, implementation in appendix A) is, to our knowledge, novel, and is a tremendous asset to future design with these devices. Compared with FEM, the amount of computation required is very small, and there is little opportunity for numerical or modelling error. Because computation is fast, results from this model may be integrated into more sophisticated calculations for device optimization purposes in the future.

Our fully-numerical implementation of the approach in [64] for evaluating the effect of thermoelastic damping in a bilayer resonator will be an asset in future work with micro- and nanomechanical resonant sensors. As TED is always present in a real-world resonator, this program will serve as a useful check to ensure that unavoidable TED effects are not limiting the performance of our devices. The details of this implementation are found in appendix B.

7.2   Future Work

There remain a few questions that should be resolved before integration of GLAD nanostructured films with our resonators should be carried out. Chief among these is the question of damping. As of this time, we have not yet identified the process(es) responsible for the bulk of dissipation in our resonators when operating at vacuum. Clamping losses due to significant BOE undercut may play a role, as may defect-related damping in the thin-film metallization layers. Potential experiments to investigate the importance of these loss mechanisms are outlined in section 6.4.2.

From a fabrication standpoint, the fact that our Al metallization films were so vigorously attacked by the BOE process is worrying, and hints at possible film contamination. Contamination of films might also exacerbate defect-related loss in our resonators, lowering Q. Future evaporative deposition of metallization films should be carried out using carbon-free crucible liners to avoid this potential issue. A simple experiment towards establishing the effect of carbon contamination in Al films would be to evaporate films from both graphite and carbon-free (tungsten or boron nitride) cru-

153

cible liners, and compare how the films hold up in BOE processing.

Once issues with damping and film purity have been addressed, one experiment might be to measure the Allan deviation (frequency stability) of our devices. This parameter, in part, determines the ultimate sensitivity of resonant gravimetric sensors, and, as such, will be of particular interest in future work. Moreover, the experimental apparatus for such a measurement (essentially, an apparatus for measuring frequency fluctuations over time) would be useful for future work in sensing.

Finally, after these points are addressed, deposition of a GLAD functionalization layer can be carried out, opening the doors to high-surface-area nanomaterial-enhanced sensing with the exquisite mass sensitivity of MEMS resonant sensors. With integration of GLAD films, the possibilities for sensing are rich and varied. Post-deposition chemical functionalization of SiO_2 GLAD films could be carried out to create specific sensors. GLAD films of different materials may yield specificity as well; for instance, a GLAD film of Au might preferentially adsorb thiol-containing molecules. All of these specific sensors would carry with them the characteristic surface-area enhancement of GLAD films.

Bibliography

[1] T. Williams, *Circuit Designer's Companion (Second Edition)*. Newnes, 2005.

[2] A. D. Inc., "Ultracompact, precision 10.0 v/5.0 v/2.5 v/3.0 v voltage references," http://www.analog.com/media/en/ technical-documentation/data-sheets/ADR01_02_03_06.pdf, 2012.

[3] P. Horowitz and W. Hill, *The Art of Electronics*, 3rd ed. Cambridge University Press, 2015.

[4] K. Brueckner, V. Cimalla, F. Niebelschütz, R. Stephan, K. Tonisch, O. Ambacher, and M. Hein, "Strain-and pressure-dependent rf response of microelectromechanical resonators for sensing applications," *Journal of Micromechanics and Microengineering*, vol. 17, no. 10, p. 2016, 2007.

[5] I. Bargatin, E. Myers, J. Arlett, B. Gudlewski, and M. Roukes, "Sensitive detection of nanomechanical motion using piezoresistive signal downmixing," *Applied Physics Letters*, vol. 86, no. 13, p. 133109, 2005.

[6] S. Fanget, S. Hentz, P. Puget, J. Arcamone, M. Matheron, E. Colinet, P. Andreucci, L. Duraffourg, E. Myers, and M. Roukes, "Gas sensors based on gravimetric detectiona review," *Sensors and Actuators B: Chemical*, vol. 160, no. 1, pp. 804–821, 2011.

[7] A. Naik, M. Hanay, W. Hiebert, X. Feng, and M. Roukes, "Towards single-molecule nanomechanical mass spectrometry," *Nature nanotechnology*, vol. 4, no. 7, pp. 445–450, 2009.

[8] M. Li, E. Myers, H. Tang, S. Aldridge, H. McCaig, J. Whiting, R. Simonson, N. Lewis, and M. Roukes, "Nanoelectromechanical resonator arrays for ultrafast, gas-phase chromatographic chemical analysis," *Nano letters*, vol. 10, no. 10, pp. 3899–3903, 2010.

[9] I. Bargatin, E. Myers, J. Aldridge, C. Marcoux, P. Brianceau, L. Duraffourg, E. Colinet, S. Hentz, P. Andreucci, and M. Roukes, "Large-scale integration of nanoelectromechanical systems for gas sensing applications," *Nano letters*, vol. 12, no. 3, pp. 1269–1274, 2012.

[10] J. Chaste, A. Eichler, J. Moser, G. Ceballos, R. Rurali, and A. Bachtold, "A nanomechanical mass sensor with yoctogram resolution," *Nature nanotechnology*, vol. 7, no. 5, pp. 301–304, 2012.

[11] J. Westwood, V. Sauer, J. Kwan, W. Hiebert, and J. Sit, "Fabrication of nanoelectromechanical systems via the integration of high surface area glancing angle deposition thin films," *Journal of Micromechanics and Microengineering*, vol. 24, no. 6, p. 065021, 2014.

[12] J. N. Westwood, "High surface area nanoelectromechanical systems via the integration of glancing angle deposition thin films," Ph.D. dissertation, University of Alberta, 2013.

[13] K. D. Harris, M. J. Brett, T. J. Smy, and C. Backhouse, "Microchannel surface area enhancement using porous thin films," *Journal of The Electrochemical Society*, vol. 147, no. 5, pp. 2002–2006, 2000.

[14] K. M. Krause, M. Thommes, and M. J. Brett, "Pore analysis of obliquely deposited nanostructures by krypton gas adsorption at 87k," *Microporous and Mesoporous Materials*, vol. 143, no. 1, pp. 166–173, 2011.

[15] S. Tsoi, E. Fok, J. C. Sit, and J. G. Veinot, "Surface functionalization of porous nanostructured metal oxide thin films fabricated by glancing angle deposition," *Chemistry of materials*, vol. 18, no. 22, pp. 5260–5266, 2006.

156

[16] S. Tsoi, "Chemical tunability of glancing angle deposition thin films," Ph.D. dissertation, University of Alberta, 2006.

[17] K. Ekinci, "Electromechanical transducers at the nanoscale: actuation and sensing of motion in nanoelectromechanical systems (nems)," *small*, vol. 1, no. 8-9, pp. 786–797, 2005.

[18] D. Karabacak, T. Kouh, and K. Ekinci, "Analysis of optical interferometric displacement detection in nanoelectromechanical systems," *Journal of Applied Physics*, vol. 98, no. 12, p. 124309, 2005.

[19] D. W. Carr, L. Sekaric, and H. G. Craighead, "Measurement of nanomechanical resonant structures in single-crystal silicon," *Journal of Vacuum Science & Technology B: Microelectronics and Nanometer Structures Processing, Measurement, and Phenomena*, vol. 16, no. 6, pp. 3821–3824, 1998.

[20] D. W. Carr, S. Evoy, L. Sekaric, H. Craighead, and J. Parpia, "Parametric amplification in a torsional microresonator," *Applied Physics Letters*, vol. 77, no. 10, pp. 1545–1547, 2000.

[21] T. Kouh, D. Karabacak, D. Kim, and K. Ekinci, "Diffraction effects in optical interferometric displacement detection in nanoelectromechanical systems," *Applied Physics Letters*, vol. 86, no. 1, p. 013106, 2005.

[22] W. Venstra, H. Westra, K. B. Gavan, and H. Van der Zant, "Magnetomotive drive and detection of clamped-clamped mechanical resonators in water," *Applied Physics Letters*, vol. 95, no. 26, p. 263103, 2009.

[23] M. Li, H. X. Tang, and M. L. Roukes, "Ultra-sensitive nems-based cantilevers for sensing, scanned probe and very high-frequency applications," *Nature nanotechnology*, vol. 2, no. 2, pp. 114–120, 2007.

[24] A. Rahafrooz and S. Pourkamali, "High-frequency thermally actuated electromechanical resonators with piezoresistive readout," *IEEE Transactions on Electron Devices*, vol. 58, no. 4, pp. 1205–1214, 2011.

[25] S. C. Jun, X. H. Huang, J. Hone, C. Zorman, and M. Mehregany, "Evaluation of 3c-sic nanomechanical resonators using room temperature magnetomotive transduction," in *Sensors, 2005 IEEE*. IEEE, 2005, pp. 4–pp.

[26] X. M. H. Huang, C. A. Zorman, M. Mehregany, and M. L. Roukes, "Nanoelectromechanical systems: Nanodevice motion at microwave frequencies," *Nature*, vol. 421, no. 6922, pp. 496–496, 2003.

[27] K. Ekinci, Y. Yang, X. Huang, and M. Roukes, "Balanced electronic detection of displacement in nanoelectromechanical systems," *Applied physics letters*, vol. 81, no. 12, pp. 2253–2255, 2002.

[28] S. C. Jun, J. H. Cho, W. K. Kim, Y. M. Jung, S. Hwang, S. Shin, J. Y. Kang, J. Shin, I. Song, J.-Y. Choi *et al.*, "Resonance properties of 3c-sic nanoelectromechanical resonator in room-temperature magnetomotive transduction," *IEEE Electron Device Letters*, vol. 30, no. 10, pp. 1042–1044, 2009.

[29] Y. Yang, C. Callegari, X. Feng, K. Ekinci, and M. Roukes, "Zeptogram-scale nanomechanical mass sensing," *Nano letters*, vol. 6, no. 4, pp. 583–586, 2006.

[30] M. T. Taschuk, M. M. Hawkeye, and M. J. Brett, "Glancing angle deposition," *Handbook of Deposition Technologies for Films and Coatings*, pp. 621–678, 2010.

[31] M. M. Hawkeye and M. J. Brett, "Glancing angle deposition: fabrication, properties, and applications of micro-and nanostructured thin films," *Journal of Vacuum Science & Technology A: Vacuum, Surfaces, and Films*, vol. 25, no. 5, pp. 1317–1335, 2007.

[32] K. Robbie and M. Brett, "Sculptured thin films and glancing angle deposition: Growth mechanics and applications," *Journal of Vacuum Science & Technology A: Vacuum, Surfaces, and Films*, vol. 15, no. 3, pp. 1460–1465, 1997.

[33] J. Sit, D. Vick, K. Robbie, and M. Brett, "Thin film microstructure control using glancing angle deposition by sputtering," *Journal of Materials Research*, vol. 14, no. 04, pp. 1197–1199, 1999.

[34] B. Dick, M. Brett, T. Smy, M. Belov, and M. Freeman, "Periodic submicrometer structures by sputtering," *Journal of Vacuum Science & Technology B: Microelectronics and Nanometer Structures Processing, Measurement, and Phenomena*, vol. 19, no. 5, pp. 1813–1819, 2001.

[35] R. Hibbeler, "Mechanics of materials," 2011.

[36] E. Volterra and E. Zachmanoglou, *Dynamics of Vibrations.* Charles E. Merrill Books, Inc., 1965.

[37] S. D. Senturia, *Microsystem design.* Springer Science & Business Media, 2007.

[38] D. Gorman, "Free lateral vibration analysis of double-span uniform beams," *International Journal of Mechanical Sciences*, vol. 16, no. 6, pp. 345–351, 1974.

[39] M. A. Koplow, A. Bhattacharyya, and B. P. Mann, "Closed form solutions for the dynamic response of euler–bernoulli beams with step changes in cross section," *Journal of Sound and Vibration*, vol. 295, no. 1, pp. 214–225, 2006.

[40] "Csc - elmer." [Online]. Available: https://www.csc.fi/web/elmer

[41] A. Bokaian, "Natural frequencies of beams under compressive axial loads," *Journal of sound and vibration*, vol. 126, no. 1, pp. 49–65, 1988.

[42] ——, "Natural frequencies of beams under tensile axial loads," *Journal of sound and vibration*, vol. 142, no. 3, pp. 481–498, 1990.

[43] J. E. Sader, I. Larson, P. Mulvaney, and L. R. White, "Method for the calibration of atomic force microscope cantilevers," *Review of Scientific Instruments*, vol. 66, no. 7, pp. 3789–3798, 1995.

[44] G. Celler, C. Scientist, and M. Wolf, "Smart cut," *A Guide to the Technology, the Process, the Products*, 2003.

[45] Z. Chemicals, "Zep520a-7 technical report," 2016.

[46] A. Hryciw, "Raith_gdsii matlab toolbox," Jul 2016. [Online]. Available: https://github.com/nrc-cnrc/Raith_GDSII

[47] L. Foster, G. Long, and M. Hunter, "Reactions between aluminum oxide and carbon the al2o3al4c3 phase diagram," *Journal of the American Ceramic Society*, vol. 39, no. 1, pp. 1–11, 1956.

[48] X. Feng, C. White, A. Hajimiri, and M. L. Roukes, "A self-sustaining ultrahigh-frequency nanoelectromechanical oscillator," *Nature nanotechnology*, vol. 3, no. 6, pp. 342–346, 2008.

[49] Mini-Circuits, "Coaxial power splitter/combiner," http://www.minicircuits.com/pdfs/ZFSCJ-2-1.pdf, 2016.

[50] J. Schurr and J. Melcher, "Unequalized currents in coaxial ac bridges," *IEEE Transactions on Instrumentation and Measurement*, vol. 53, no. 3, pp. 807–811, 2004.

[51] *LQH3NP_G0 Series (1212 Size)*, Murata Manufacturing Co., Ltd., 5 2011.

[52] *Design With PIN Diodes*, Skyworks Solutions, Inc, 11 2012.

[53] S. S. Inc., "Smv1801-079lf: Hyperabrupt junction tuning varactor," http://www.skyworksinc.com/uploads/documents/SMV1801_079LF_200915F.pdf, 2012.

[54] *Varactor SPICE Models for RF VCO Applications*, Skyworks Solutions, Inc, 02 2010.

[55] *E3620A and E3630A Non-programmable DC Power Supplies Data Sheet*, Keysight Technologies, 08 2014.

[56] *LMC6482 CMOS Dual Rail-to-Rail Input and Output Operational Amplifier*, Texas Instruments, 04 2015.

[57] I. T. AG, "Ba696/ba885/ba895 silicon pin diode," http://www.infineon.com/dgdl/Infineon-BA595_BA885_BA895SERIES-DS-v01_01-en.pdf?fileId=db3a304314dca3890114fdf44fbb09fe, 2009.

[58] S. S. Inc., "Smv1405 to smv1430 series: Plastic packaged abrupt junction tuning varactors," http://www.skyworksinc.com/uploads/documents/SMV1405_1430_Series_200068V.pdf, 2016.

[59] K. Bruckner, V. Cimalla, F. Niebelschutz, R. Stephan, K. Tonisch, O. Ambacher, and M. Hein, "Gas pressure sensing based on mems resonators," in *Sensors, 2007 IEEE*. IEEE, 2007, pp. 1251–1254.

[60] S. S. Verbridge, R. Ilic, H. Craighead, and J. M. Parpia, "Size and frequency dependent gas damping of nanomechanical resonators," *Applied Physics Letters*, vol. 93, no. 1, p. 013101, 2008.

[61] M. Bao and H. Yang, "Squeeze film air damping in mems," *Sensors and Actuators A: Physical*, vol. 136, no. 1, pp. 3–27, 2007.

[62] C. Zhang, G. Xu, and Q. Jiang, "Characterization of the squeeze film damping effect on the quality factor of a microbeam resonator," *Journal of Micromechanics and Microengineering*, vol. 14, no. 10, p. 1302, 2004.

[63] S. Vengallatore, "Gorsky damping in nanomechanical structures," *Scripta materialia*, vol. 52, no. 12, pp. 1265–1268, 2005.

[64] S. Prabhakar and S. Vengallatore, "Thermoelastic damping in bilayered micromechanical beam resonators," *Journal of Micromechanics and Microengineering*, vol. 17, no. 3, p. 532, 2007.

[65] D.-h. Choi and W. D. Nix, "Anelastic behavior of copper thin films on silicon substrates: Damping associated with dislocations," *Acta materialia*, vol. 54, no. 3, pp. 679–687, 2006.

[66] X. Liu, E. Thompson, B. White Jr, and R. Pohl, "Low-temperature internal friction in metal films and in plastically deformed bulk aluminum," *Physical Review B*, vol. 59, no. 18, p. 11767, 1999.

[67] C. Zener, "Internal friction in solids. i. theory of internal friction in reeds," *Physical review*, vol. 52, no. 3, p. 230, 1937.

[68] R. Lifshitz and M. L. Roukes, "Thermoelastic damping in micro-and nanomechanical systems," *Physical review B*, vol. 61, no. 8, p. 5600, 2000.

[69] I. Wilson-Rae, "Intrinsic dissipation in nanomechanical resonators due to phonon tunneling," *Physical Review B*, vol. 77, no. 24, p. 245418, 2008.

[70] W. Zhang, R. Baskaran, and K. L. Turner, "Effect of cubic nonlinearity on auto-parametrically amplified resonant mems mass sensor," *Sensors and Actuators A: Physical*, vol. 102, no. 1, pp. 139–150, 2002.

[71] Y. C. Wang, S. G. Adams, J. S. Thorp, N. C. MacDonald, P. Hartwell, and F. Bertsch, "Chaos in mems, parameter estimation and its potential application," *IEEE Transactions on Circuits and Systems I: Fundamental Theory and Applications*, vol. 45, no. 10, pp. 1013–1020, 1998.

[72] N. Kacem, S. Hentz, D. Pinto, B. Reig, and V. Nguyen, "Nonlinear dynamics of nanomechanical beam resonators: improving the performance of nems-based sensors," *Nanotechnology*, vol. 20, no. 27, p. 275501, 2009.

[73] J. F. Rhoads, S. W. Shaw, and K. L. Turner, "Nonlinear dynamics and its applications in micro-and nanoresonators," *Journal of Dynamic Systems, Measurement, and Control*, vol. 132, no. 3, p. 034001, 2010.

[74] M. Brennan, I. Kovacic, A. Carrella, and T. Waters, "On the jump-up and jump-down frequencies of the duffing oscillator," *Journal of Sound and Vibration*, vol. 318, no. 4, pp. 1250–1261, 2008.

Appendix A

Calculation of U-Cantilever Resonant Frequency using MATLAB

A.1   Description

The code below computes the resonant frequency of a U-cantilever resonator using the multi-span beam approximation of section 2.4.2. This model works very well for U-cantilevers with an aspect ratio (length / cross-bar width) greater than 1. See section 2.4.2 for more details.

A.2   Implementation

```matlab
1   function [freal] = UCantileverResFreq(lw, t, L, W)
2   % UCantileverResFreq    Compute resonant frequency of U-cantilever
3   % structure using the stepped-beam technique of Chapter 2.
4   %    freal = UCantileverResFreq(lw, t, L, W) computes the resonant
5   %    frequency freal of a U-cantilever resonator from the beam width lw,
6   %    beam thickness t, beam length L, and the width of the cross-bar W.
7   %    See chapter 2 for more details.
8
9
10  % Material Constants for Silicon
11  E = 165e9;         % Young's modulus (Pa)
12  rho = 2330;        % Mass density (kg/m^3)
13
14  % Device Dimensions
```

```matlab
15   L1 = L - lw;      % Length before crossbar
16   L2 = lw;          % Length of crossbar section
17
18   % Area Moment of Inertia for Beam and Cross-Bar
19   I1 = lw * (t)^3 / 12;
20   I2 = (W/2+lw) * (t)^3 / 12;
21
22   % We require that both segments of the resonator vibrate at
23   % the same frequency. This fixes the ratio kr=k2/k1
24   kr = sqrt(sqrt((I1/I2)* ((W/2+lw)/(lw))));
25
26   % Matrix due to imposition of constraints at the interface
27   % between beam and the cross-bar. For non-trivial
28   % solutions, this matrix must be singular (det(A)=0).
29   A = @(k1,L1,k2,L2) [
30       cos(k1*L1)-cosh(k1*L1) sin(k1*L1)-sinh(k1*L1) -(cos(k2*L2)+cosh(k2*L2)) -(sin
             ↪ (k2*L2)+sinh(k2*L2))
31       (-sin(k1*L1)-sinh(k1*L1)) (cos(k1*L1)-cosh(k1*L1)) (k2./k1).*(-sin(k2*L2)+
             ↪ sinh(k2*L2)) (k2./k1)*(cos(k2*L2)+cosh(k2*L2))
32       (-cos(k1*L1)-cosh(k1*L1)) (-sin(k1*L1)-sinh(k1*L1)) -(I2/I1)*(k2/k1).^2.*(-
             ↪ cos(k2*L2)+cosh(k2*L2)) -(I2/I1)*(k2/k1).^2.*(-sin(k2*L2)+sinh(k2*L2))
33       (sin(k1*L1)-sinh(k1*L1)) (-cos(k1*L1)-cosh(k1*L1)) (I2/I1)*(k2/k1).^3.*(sin(
             ↪ k2*L2)+sinh(k2*L2)) (I2/I1)*(k2/k1).^3.*(-cos(k2*L2)+cosh(k2*L2))
34       ];
35
36   % Condition number of matrix A for some k1,k2
37   % Useful to verify conditioning of our root-finding problem.
38   % Acond = @(k1,k2) cond(A(k1,L1,k2,L2));
39
40   % Evaluate det(A) for some k1
41   % (k2 is determined through kr).
42   A1Dkr = @(k1) det(A(k1,L1,k1*kr,L2));
43
44   % Initial guess for k from modelling the beam as a
45   % cantilever clamped at one end and free at the other.
46   estimatedk = 1.875/(L1+L2);
47
48   % Find root of A1Dkr(k1), with estimatedk as a guess.
49   kreal = fzero(A1Dkr,estimatedk);
50
51   % Compute the resonant frequency using kreal
52   freal = kreal^2*sqrt((E)*I1/(rho*t*lw))/2/pi;
53   end
```

Appendix B

Evaluation of Thermoelastic Damping using MATLAB

B.1 TED in the Uniform Beam

B.1.1 Description

The code below computes the quality factor Q due to thermoelastic damping alone for a resonator with a rectangular cross-section, and thickness t_b. The code below assumes that the beam material is Si, but may be easily modified for use with other materials by substituting the material properties. The method used is from [68], which gives the quality factor due to TED in a uniform beam as:

$$Q^{-1} = \frac{E\alpha^2 T_0}{C_v} \left(\frac{6}{\xi^2} - \frac{6}{\xi^3} \frac{\sinh \xi + \sin \xi}{\cosh \xi + \cos \xi} \right) \tag{B.1}$$

where:

$$\xi = b\sqrt{\frac{\omega_0}{2\chi}}$$

B.1.2 Implementation

```
1  function [Q] = TEDUniform(t_b, w0)
2  % TEDUniform    Compute quality factor of resonance due only to
```

```
3   % thermoelastic damping effects in a uniform Si beam.
4   %   Q = TEDUniform(t_b, w0) computes Q for an Si beam of thickness
5   %   t_b, vibrating at an angular frequency w0.
6   %
7   % This code uses the method described in:
8   % Lifshitz, R., & Roukes, M. L. (2000). Thermoelastic damping in micro-
9   % and nanomechanical systems. Physical review B, 61(8), 5600.
10
11  % Material Constants for Silicon
12  E = 165e9;                    % Young's modulus (Pa)
13  alpha = 2.6e-6;               % Thermal expansion coeff (K^-1)
14  chi = 8.8e-5;                 % Thermal diffusivity of Si m^2/s
15  sp_heat_cap1 = 0.712e3;       % Specific heat capacity (J/kg/K)
16  rho = 2330;                   % Mass density (kg/m^3)
17  C = rho*sp_heat_cap1;         % Constant volume heat capcity (J/m^3/K)
18
19  T0 = 293;                     % Ambient temperature (K)
20
21  b = t_b;                      % Beam thickness (m)
22
23  xi = @(w) b*sqrt(w/(2*chi));
24
25  qinv = @(w) E*alpha^2*T0/C.*(6./(xi(w).^2)-6./(xi(w).^3).* ...
26      (sinh(xi(w))+sin(xi(w)))./(cosh(xi(w))+cos(xi(w))));
27
28  Q=1/qinv(w0);
29  end
```

B.2   TED in the Bilayer (Metallized) Beam

B.2.1   Description

The code below computes the quality factor Q due to thermoelastic damping alone for a bi-layer resonator with a rectangular cross-section. The thickness of the device layer (material 1) is given as t_b, while the thickness of the thin-film coating (material 2) is given as t_{film}. The code below assumes that material 1 is Si and that material 2 is Al, but may be easily adapted to other material stack-ups by substituting the relevant material properties.

The method used is from [64]. Note that, while the implementation in [64] was realized using a combination of symbolic and numerical analysis, the implementation here is completely numerical. Correctness of implementation was verified by demonstrating that the computed quality factor converges to that computed in section B.1 as the thin-film coating is made arbitrarily thin, as shown in Figure. B.1.

B.2.2   Implementation

```matlab
 1  function [Q] = TEDBilayer(t_b, t_film, w0)
 2  % TEDBilayer    Compute quality factor of resonance due only to
 3  % thermoelastic damping effects in an Si beam coated with a thin film of Al.
 4  %   Q = TEDBilayer(t_b, t_film, w0) computes Q for an Si beam of thickness
 5  %   t_b coated with an Al film of thickness t_film, vibrating at an angular
 6  %   frequency w0.
 7  %
 8  % This code uses the technique described in:
 9  % Prabhakar, Sairam, and Srikar Vengallatore. "Thermoelastic damping in
10  % bilayered micromechanical beam resonators." Journal of Micromechanics and
11  % Microengineering 17.3 (2007): 532.
12  %
13
14
15  % Material Constants for Silicon
16  E1 = 165e9;                    % Young's modulus (Pa)
17  alpha1 = 2.6e-6;               % Thermal expansion coeff (K^-1)
18  sp_heat_cap1 = 0.712e3;        % Specific Heat Capacity (J/kg/K)
19  rho1 = 2330;                   % Mass density (kg/m^3)
20  C1 = rho1*sp_heat_cap1;        % Constant volume heat capcity (J/m^3/K)
21  k1 = 148;                      % Thermal conductivity (W/m/K)
22
23  % Material Constants for Aluminum
24  E2 = 69e9;                     % Young's modulus (Pa)
25  alpha2 = 22.2e-6;              % Thermal expansion coeff (K^-1)
26  sp_heat_cap2 = 0.902e3;        % Specific Heat Capacity (J/kg/K)
27  rho2 = 2700;                   % Mass density (kg/m^3)
28  C2 = sp_heat_cap2*rho2;        % Constant volume heat capcity (J/m^3/K)
29  k2 = 237;                      % Thermal conductivity (W/m/K)
30
31  % Beam Geometry
32  t1 = t_b;                      % Si device layer thickness (m)
33  t2 = t_film;                   % Al film thickness (m)
34
35  % Number of terms to include in eigenfunction expansion
36  Nterms = 15;
37
38  T0 = 298;                      % Room temperature (K)
39
40  % Z-coordinates of top of device layer and top of film, respectively
41  z1 = t1;
42  z2 = t1+t2;
43
44  % Transformation factor for transformed section method
45  n_trans = E2/E1;
46
47  % Z-coordinate of neutral axis
48  z0 = (t1/2*t1 + (t1+t2/2)*t2*n_trans)/(t1+t2*n_trans);
49
50  % Eigenvalue-determining matrix (must be singular)
51  R = sqrt(k1*C1/k2/C2);
52  M = @(bn) [-cos(bn*sqrt(C1/k1)*z1) cos(bn*sqrt(C2/k2)*z1) sin(bn*sqrt(C2/k2)*z1)
53      -R*sin(bn*sqrt(C1/k1)*z1) sin(bn*sqrt(C2/k2)*z1) -cos(bn*sqrt(C2/k2)*z1)
54      0 -sin(bn*sqrt(C2/k2)*z2) cos(bn*sqrt(C2/k2)*z2)];
55
56  % Roots of f are the eigenvalues Bn, where Bn>0
57  f = @(x) det(M(x));
58
59  % Guess roots based on single-layer beam case
60  % Note: If thin film coating is made thicker, this may have to be adjusted.
61  % Plot the roots on a plot of f(x) to check.
62  bguess = @(n) n*pi/t1*sqrt(k1/C1);
63
```

```matlab
64    % Use root−finding method to determine eigenvalues
65    Bn = @(n) fzero(f,bguess(n));
66    Bns = arrayfun(Bn, 1:Nterms);
67
68    % Eigenfunctions
69    phi1 = @(n) @(z) cos(Bns(n)*sqrt(C1/k1)*z);
70    phi2 = @(n) @(z) R*sin(Bns(n)*sqrt(C1/k1)*z1)*cos(Bns(n)*sqrt(C2/k2)*z2)/ ...
71        sin(Bns(n)*sqrt(C2/k2)*z2*(z1/z2−1))*cos(Bns(n)*sqrt(C2/k2)*z) + ...
72        R*sin(Bns(n)*sqrt(C1/k1)*z1)*sin(Bns(n)*sqrt(C2/k2)*z2)/sin(Bns(n) ...
73        *sqrt(C2/k2)*z2*(z1/z2−1))*sin(Bns(n)*sqrt(C2/k2)*z);
74
75    % Pre−evaluate for efficiency
76    phi1s = arrayfun(phi1, 1:Nterms, 'UniformOutput', false);
77    phi2s = arrayfun(phi2, 1:Nterms, 'UniformOutput', false);
78
79    % Note: x dependence in Ln cancels out during calculation of Q.
80    % This x dependence has been ommited here for simplicity.
81    % See accompanying text for details.
82    Ln = @(n) (alpha1*E1*integral(@(z) (z−z0).*feval(phi1(n),z), 0, z1) + ...
83        alpha2*E2*integral(@(z) (z−z0).*feval(phi2(n),z), z1, z2));
84
85    % Pre−compute Ln values for efficiency
86    Lns = arrayfun(Ln, 1:Nterms);
87
88    % Compute Nn values
89    Nn = @(n) C1*integral(@(z) feval(phi1(n),z).^2, 0, z1)+C2*integral(@(z) feval(
          ↪ phi2(n),z).^2, z1, z2);
90    Nns = arrayfun(Nn,1:Nterms);
91
92    % Approximate (truncated sum) expressions for excess temperature theta_i in
93    % each region (0<z<z1, z1<z<z2).
94    theta_trunc1 = @(n) @(z) −T0*sum(arrayfun(@(ni) (1i*w0)/(Bns(ni)^2+1i*w0)*Lns(ni)
          ↪ ./Nns(ni).*feval(phi1s{ni},z), 1:n));
95    theta_trunc2 = @(n) @(z) −T0*sum(arrayfun(@(ni) (1i*w0)/(Bns(ni)^2+1i*w0)*Lns(ni)
          ↪ ./Nns(ni).*feval(phi2s{ni},z), 1:n));
96
97    % h1,h2 are the truncated sum expressions, ready for evaluation.
98    h1 = theta_trunc1(Nterms);
99    h2 = theta_trunc2(Nterms);
100
101   % Imaginary part of h1,h2
102   ih1 = @(z) arrayfun(@(x) imag(h1(x)), z);
103   ih2 = @(z) arrayfun(@(x) imag(h2(x)), z);
104
105   % Loss per cycle of vibration = dW1 + dW2
106   % (In reality, the energy lost is:
107   % (dW1+dW2)*W*integral(@(x) (K0(x))^2, 0, L), but these two factors are
108   % present in the denominator (W1+W2), and therefore cancel out.
109   dW1 = −pi*alpha1*E1*integral(@(z) (z−z0).*ih1(z), 0, z1);
110   dW2 = −pi*alpha2*E2*integral(@(z) (z−z0).*ih2(z), z1, z2);
111
112   % Stored energy during vibration = W1 + W2
113   % (In reality, the energy stored is:
114   % (W1+W2)*W*integral(@(x) (K0(x))^2, 0, L), but these two factors are
115   % present in the numerator (dW1+dW2), and therefore cancel out.
116   W1 = (E1/2)*integral(@(z) (z−z0).^2, 0, z1);
117   W2 = (E2/2)*integral(@(z) (z−z0).^2, z1, z2);
118
119   Qinv = (dW1+dW2)/(2*pi*(W1+W2));
120
121   Q=1/Qinv;
122   end
```
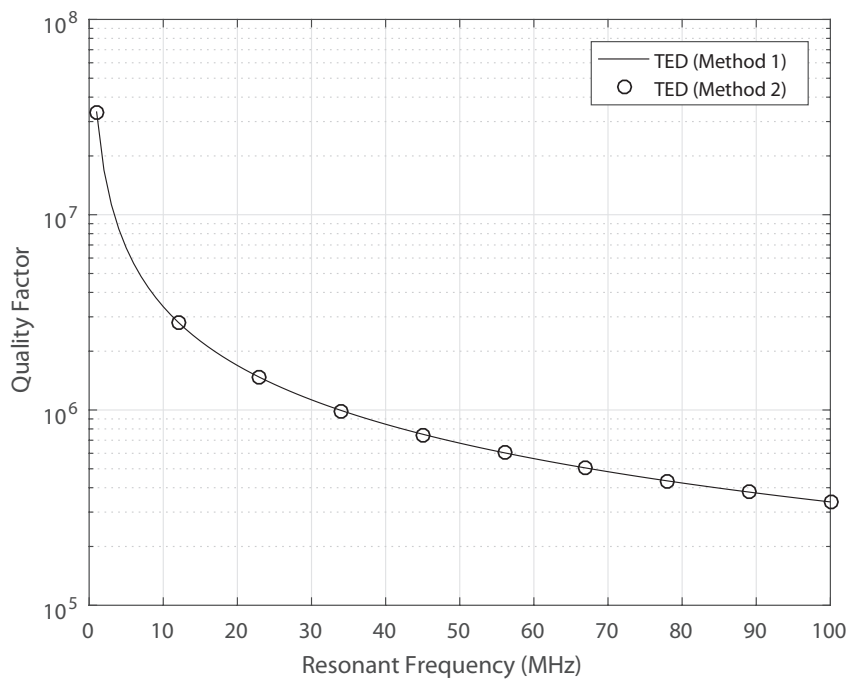
Figure B.1: TED for a uniform Si beam with a thickness of 145 nm computed using method 1 (section B.1) and method 2 (section B.2). The thin film thickness was set to 0.001 nm for the purposes of calculation using the bilayer method. The bilayer method reduces to the result for the uniform beam as the film thickness approaches zero, as required.